Dynamics in Polymer Thin Films by Inelastic Neutron Scattering

Rintaro Inoue

2008

Contents

Chapter 1

General Introduction

1.1 Introduction

Organic and inorganic thin films are utilized very much in various applications such as optical and electronic devices. In the case of the inorganic materials, thin films are prepared by sputtering, deposition by electron beam (EB), and highly aligned metal mono-layer film is made by manipulating each molecule in nm scale. In the case of organic materials polymers are often used to prepare thin films because of the high viscosity, and we can prepare stable thin films by simple methods like vapor evaporation methods including spin-coatng and dip coat [1-3]. Sometimes Langmuir-Blodgett method [4,5] is employed to prepare thin mono-molecular layer of surfactants. Owing to the convenience for preparation, polymer thin films are used very much in industrial fields, however there remain many problems concerning the physical properties such as size and thermal stabilities. The properties are very different from those of bulk, and sometimes are related to the dynamic properties of polymer thin films. In this thesis, therefore, we studied the dynamic properties of polymer thin films from molecular level to understand the unusual physical properties.

Generally speaking, polymers are classified into crystalline and non-crystalline polymers. Crystalline polymer thin films are not stable because of the slow progress in crystallization and the surface is usually very rough because of co-existence of crystalline and amorphous regions in the thin films. Therefore, most polymer thin films utilized in industry are prepared with non-crystalline polymers. In this thesis we mainly studied

single component amorphous polymer thin films due to the above reason.

With the recent progress of evaluation methods for polymer thin films [6-14], it was revealed that the thermal and mechanical properties of polymer thin films were very different from those of bulk. One of the most interesting topics in the findings is the thickness dependence of glass transition temperature T_g. Non-crystalline polymers have no melting temperature T_m, therefore T_g is considered as the most important physical constant for non-crystalline polymers. Therefore the thickness dependence of T_g is highlighted from not only scientific but also industrial point of view. For polystyrene (PS), which has weak interactions with Si substrate, it was revealed by reflectivity method and ellipsometry [15-18] that T_g decreased with film thickness. In some reports [15,17,19,20] this result was interpreted in terms of a mobile surface layer, however the definite mechanism of glass transition of PS thin film is still missing.

In order to understand the glass transition in polymer thin films, we have to know the mechanism of glass transition in bulk. In the last two decades experimental and theoretical studies on glass transition phenomena have been extensively performed for various glass-forming materials. These studies have presented a key concept to understand the glass transition. In the concept "cooperativity" plays the most important role. In a high temperature above the glass transition temperature T_g molecules move independently, but as temperature decreases close to T_g they must move cooperatively due to the increase of density. The domain where molecules move cooperatively is often called as a cooperative rearranging regions (CRR) [21]. One of the way to estimate the size of the CRR is a study of glass transition of confined molecular systems. It was considered that the fundamentally different dynamics would be observed in glass forming molecules confined in porous media or polymer thin films when the size of the confinement is less than that of CRR. Hence many experiments were done along this direction using polymer thin films, but some of works found that surface and/or interface effects were not negligible in the glass transition. In the following sections, we will review the studies on glass transition in bulk and in thin films to show current situation of the researches in this filed and to give a basis to the studies in this thesis.

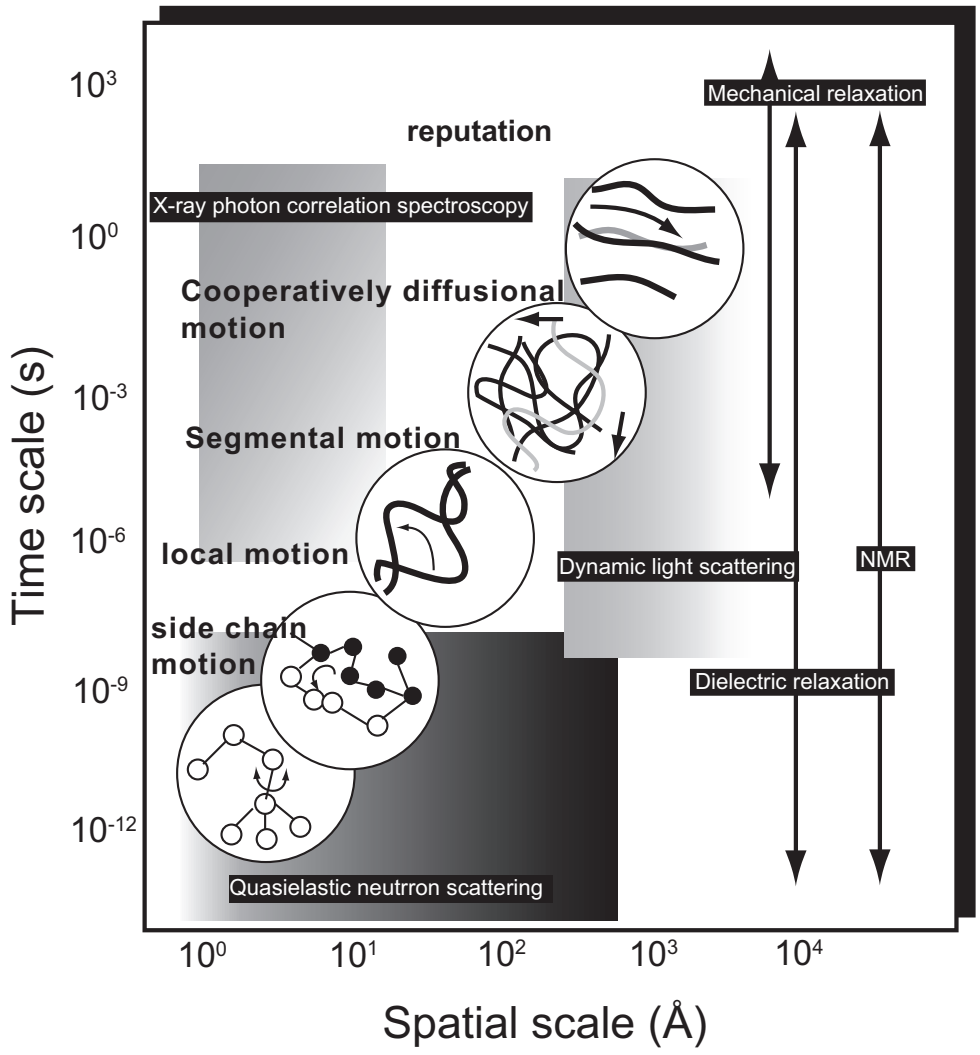

Figure 1.1: Time and spatial scale dependence of dynamics of amorphous polymer and related instrument.

Another important subject in this thesis is a dynamics of polymers. As revealed in the previous studies, many people believe that glass transition is a relaxation phenomena. In other words, glass transition is not a thermodynamic transition, but dynamic transition. Hence we studied dynamics of polymer thin films to understand the glass transition. However, as well known there are many modes of motions in polymers, and we have to know which mode is dominant in glass transition in polymer thin films. As an example we show some modes of motion observed in amorphous polymer in Figure 1-1 in time and space. We supposed that the lack of the dynamical studies on polymer thin films was one of the main reasons for the insufficient understanding of glass transition of polymer thin films, and believe that dynamical studies on polymer thin films give us a clue to understand the glass transition of polymer thin films. In this thesis, therefore, dynamic studies of polymer thin films were performed using inelastic neutron scattering, aiming the clarification of the glass transition of polymer thin films. In the following sections we review the previous works on glass transition in bulk and in polymer thin films in sections 1.2 and 1.3, respectively, to show the background of this thesis. We will describe the motivation of this work in section 1.4 and outline of this thesis in section 1.5.

1.2 Brief Summary of Studies on Glass Transition

It is well known that solids can be classified into crystal and amorphous solids. Atoms or molecules in crystalline solids align periodically with a long range order, and the macroscopic structure can be described by the microscopic unit cell due to the long range order. On the other hand, there exist no long range order in amorphous solids. Amorphous solids including organic and inorganic substances can be obtained by various ways such as rapid cooling the corresponding liquids [22,23], vapor deposition [24,25], mechanical milling [26] and so on. Among them, amorphous solids obtained through the rapid cooling of liquids is often called glasses because they are vitrified through the glass transition from liquids. In a sense glass is one of amorphous solids. On heating the glasses they usually crystallize at a certain temperature above the glass

transition temperature T_g. In this section we especially focus on glasses state among amorphous solids.

Glasses have no long-range order in the structure and have isotropic elastic property. The transition from liquid to glass is normally known as glass transition and formerly glass transition phenomenon was studied mainly by thermodynamic and mechanical measurements. From the mechanical point of view, glass is realized when the viscosity is equal to about 10^{13} poise or the average relaxation time is equal to 100 s. From thermodynamic point of view, glassy state can be characterized as residual entropy even at T=0, implying the violation of the third law of thermodynamics. These are some representative definitions of glassy state, and next we would like to consider the thermodynamic singularity at the glass transition. Figure 1-2 indicates the schematic view of temperature dependence of entropy (S) of a glass-forming material. When the glass-forming materials is cooled down rapidly from above the melting temperature (T_m), it easily get into metastable state called supercooled state due to the insufficient time for crystallization. The thermal expansivity changes at a given temperature with further cooling. This corresponds to the glass transition temperature T_g and the changes of thermodynamic quantities at around T_g are shown in Figure 1-3. The volume and the enthalpy are continuous at around T_g but the 1st deferential of these values are discontinuous below and above T_g. According to the Etherenfest's definition, the glass transition was formerly known as thermodynamic 2nd order phase transition. However this assumption is not true because T_g strongly depends on the cooling rate, hence we cannot determine unique T_g value experimentally. Therefore it is commonly recognized that glass transition is considered as a dynamical process or a relaxational process [27]. First, we would like to focus on some theoretical models that describe the glass transition.

The simplest theory for the glass transition is the free volume theory [28]. This theory is based on the following model. A molecule is treated as a sphere, which is confined in a cage defined by its nearest neighboring molecules. The total volume (V_{total}) of the system is defined by the addition of volume occupied by molecule (V_{occ})

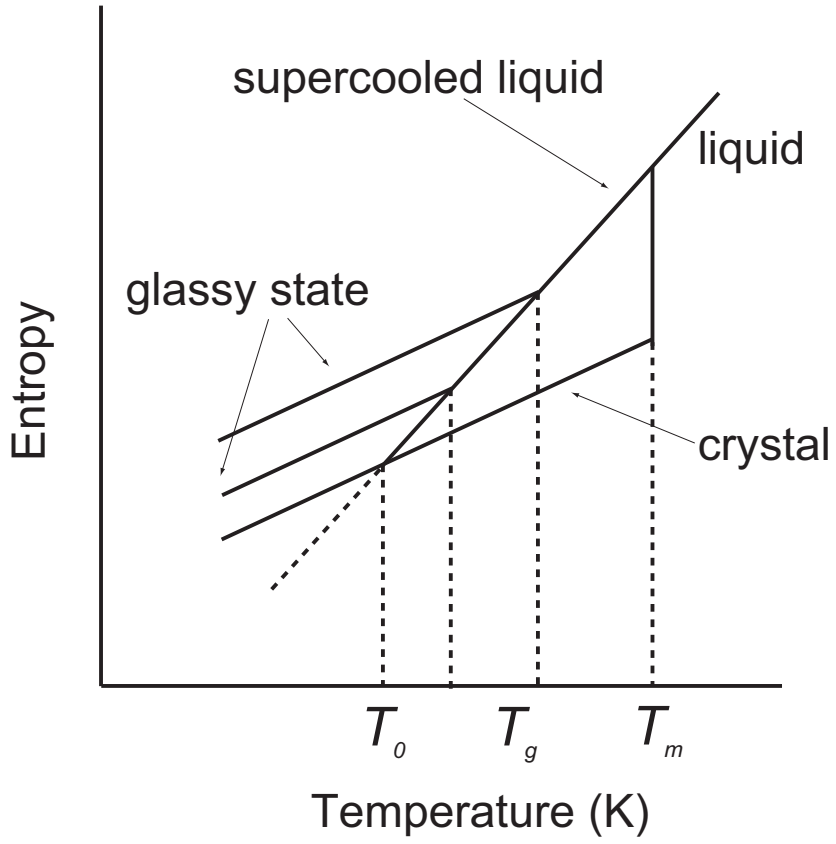

Figure 1.2: Temperature dependence of entropy for glass-forming material.

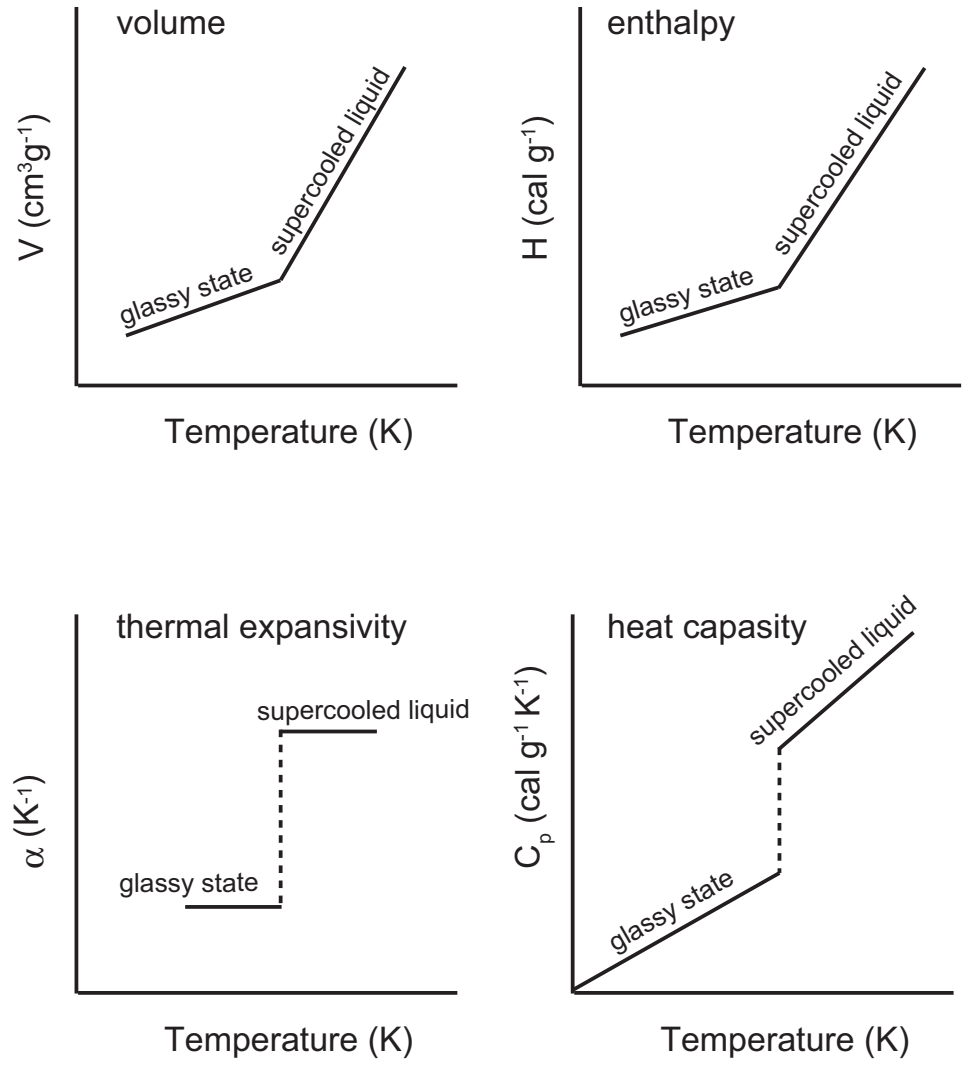

Figure 1.3: Schematic view of thermal behaviors of glass-forming material at around T_g.

and the remaining free volume (V_{free}). The total free volume is randomly distributed by the available thermal energy. Molecules are able to move when there are voids larger than a certain minimum value. As the liquid is cooled, the free volume (V_{free}) decreases until the free volume is so small that the molecular motion is no longer possible at the glass transition temperature (T_g). Using the empirical Doolittle equation which describes the free volume dependence of viscosity η is given by

$$\ln \eta = \ln A + B\frac{V_{occ}}{V_{free}} = \ln A + B\frac{V_{total} - V_{free}}{V_{free}} = \ln A + B\Big(\frac{1}{f} - 1\Big), \tag{1.1}$$

where A, B are constants and $f = V_{free}/V_{total}$, respectively. Under the notion of time-temperature reducibility, the viscosity $\eta(T)$ at a given temperature T can be described by that at a reference temperature ($=T_{ref}$) [29]. The ratio for $\eta(T)$ to $\eta(T_{ref})$ is defined as shift factor a_T. In this expression, we used T_g as T_{ref} and then we can obtain a following equation.

$$\ln a_T = \ln \frac{\eta(T)}{\eta(T_g)} = B\Big(\frac{1}{f(T)} - \frac{1}{f(T_g)}\Big). \tag{1.2}$$

With an assumption that temperature dependence of $f(T)$ is described by the following equation,

$$f(T) = f(T_g) + \Delta\alpha(T - T_g). \tag{1.3}$$

In the above expression, $\Delta\alpha$ is the difference of thermal expansivity between the glassy state and the molten state. Finally, we can obtain Williams-Landel-Ferry (WLF) equation [30].

$$\log a_T = \log \frac{\eta(T)}{\eta(T_g)} = \frac{-B}{2.303 f(T_g)}\Big(\frac{T - T_g}{f(T_g)/\Delta\alpha + T - T_g}\Big) = \frac{-C_1(T - T_g)}{C_2 + (T - T_g)}, \tag{1.4}$$

where C_1 and C_2 are constants. Mathematically, this WLF equation is identical to so-called Vogel-Fulcher (VF) equation [34] given by below

$$\eta(T) = \eta_0 \exp\Big(\frac{B}{T - T_0}\Big), \tag{1.5}$$

where T_0 is called the Vogel-Fulcher temperature, η_0 and B are constants. This equation indicates that the relaxation time diverges at the temperature (T_0) and the temperature dependence of η was well described by the WLF or VF equation, as shown in Figure

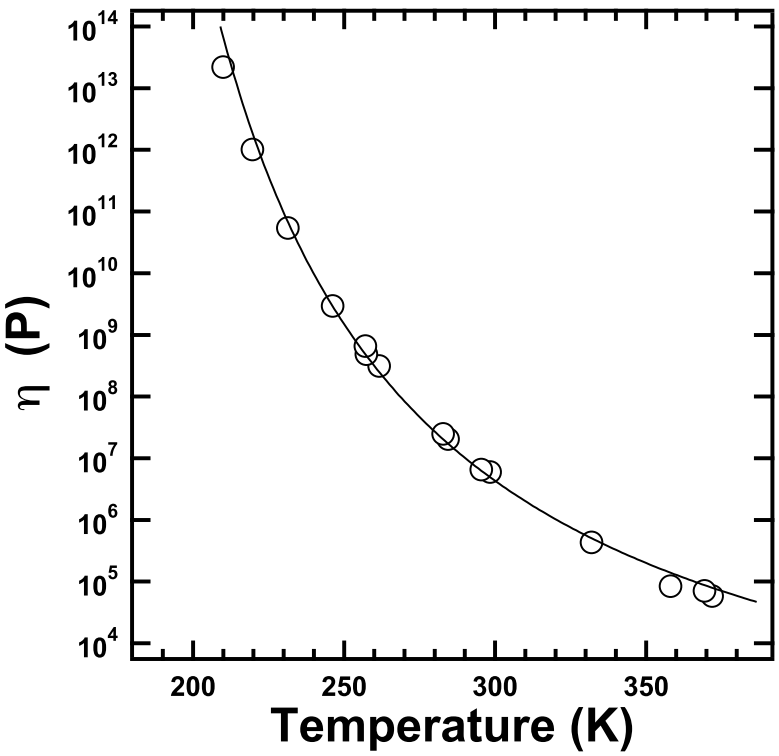

Figure 1.4: Temperature dependence of viscosity observed for polyisobutylene (PIB) [32].

1-4 [32]. In general, the observed T_g is higher than T_0 and T_0 is also known as the ideal glass transition temperature, which can be reached only by the infinitely slow cooling (Figure 1-2). The temperature dependence of viscosity, which increases drastically at around T_g was well described by the notion of free volume. However, the relation between the very low entropy near T_g and the radical slowing down of motions at the glass transition was not understood from the free volume theory. In order to answer the above problem, a notion of cooperatively rearranging motions was introduced by Adam and Gibbs [21]. They suggested that the existence of a cooperatively rearranging region (CRR) as a subregion of the sample in which molecules can be rearranged into another configuration. The size of CRR was shown to be related to the configurational entropy of the system. By introducing a relation between the structural relaxation time and cooperativity size, the WLF equation or VF equation was successfully obtained. This theory provided a background for the observed slowing down of the dynamics in terms of cooperative structural rearrangements in the glass-forming materials, but not individual motions. This schematically illustrated in Figure 1-5. However, the information for the size of CRR has not been indicated in their paper. We would like to describe the estimation of size of CRR in this section later. The free volume theory or the Adam Gibbs theory describe the phenomenologically glass transition, and predict some thermodynamic properties. Therefore most of the experimental works have been done to confirm the macroscopic predictions by the theories. Theoretical approaches, which connect the subtle structural change and the drastic change of relaxation time at the glass transition qualitatively was demanded for a long time. Especially, there exists no long range order like crystal, and hence microscopic molecular level measurements are required.

At the beginning of 1980's, the mode coupling theory (MCT), which successfully described the dynamics of critical phenomenon was applied to the phenomenon of glass transition. The theory predicts two dynamical modes (α-process and β-process) and an ergodic-nonergodic dynamical transition according to the freezing of the slow α process below the critical temperature (T_c). Many theoretical predictions which could be

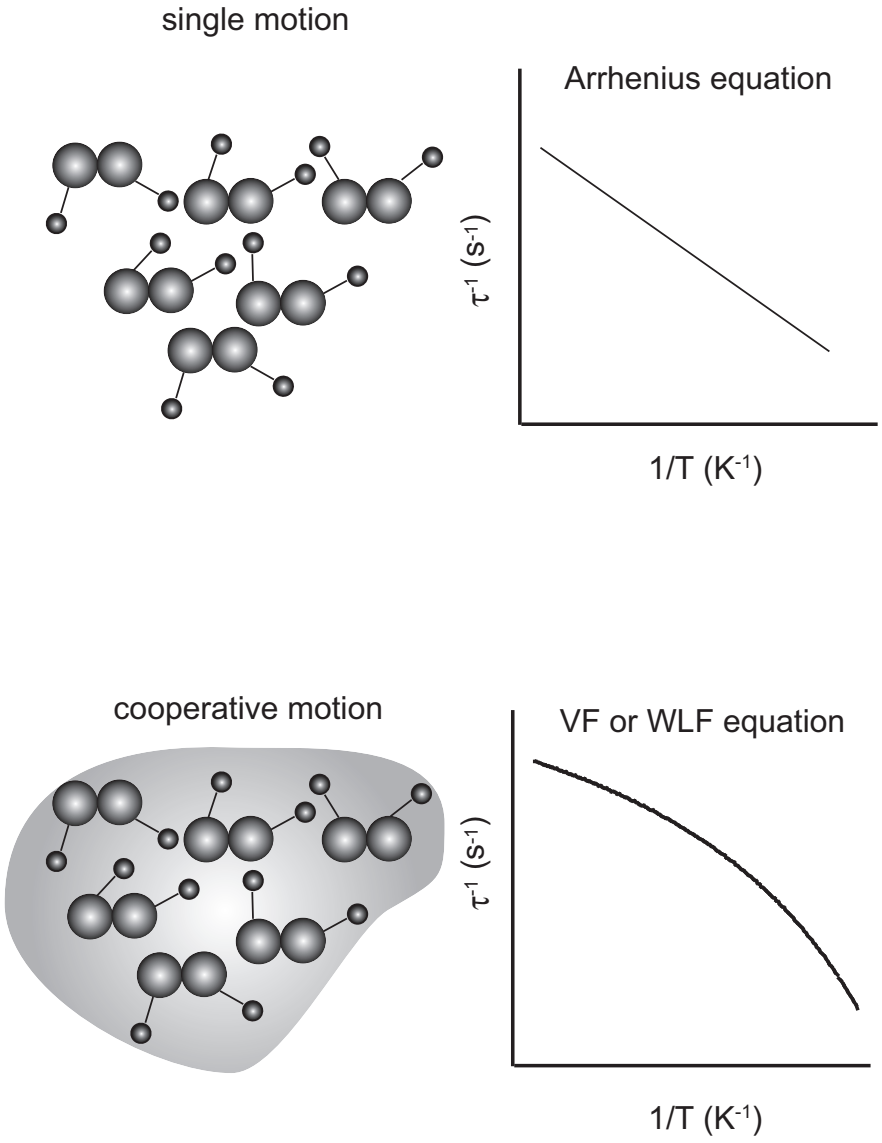

Figure 1.5: Simple schematic view of single motion and cooperative motion and its temperature dependence of relaxation rate, respectively.

verified experimentally were offered by Götze [33] and many researchers performed experiments in order to confirm these predictions by quasielastic neutron scattering, quasielastic light scattering, dielectric relaxation, nuclear magnetic resonance (NMR), mechanical relaxation (MR) and so on. From the vigorous researches, it was found that MCT was approximately valid above T_c that is about 1.2 times higher or about 50K higher than T_g, but not applicable below T_c. This is the current interpretation of MCT [34]. There is some criticism to MCT. Originally MCT was developed to describe the long wavelength phenomena near a critical point, however the glass transition is a short wavelength phenomena in a spatial scale at around the first peak of the structure factor $S(Q)$. Hence some criticisms were focused on this point. Concerning to the application of MCT to glass transition, there is a review by Kaswasaki and please refer it for more detail [35]. Other theoretical approaches, which were not based on liquid theory have been proposed to describe the glass transition. The trapping diffusion model [36] is a theory that describes glass transition from stochastic process. Tanaka [37] has proposed a phenomenological theory based on multi-order parameters. Another approach is based on on energy landscape [38] in order to describe the glass transition. Recently, there exists a theoretical approach that introduced free volume or interstice, which is dependent on time and space into solid with a lot of lattice defect in order to understand the dynamical properties of amorphous structure [39]. We have described the theoretical approach for glass transition in this section and we also would like to describe the experimental approaches for the understanding of glass transition behaviour.

The key to understand glass transition phenomenon is dynamical heterogeneity and the evaluation of characteristic length at the glass transition (or size of CRR). It is well known that density-density correlation function $\phi(t)$ of α process is not described by a simple Debye type equation but by the so-called Kohlrausch-Williams-Watts (KWW) equation or stretched exponential function [40].

$$\phi(t) = \phi_0\Big(-\frac{t}{\tau}\Big)^{\beta} (0 < \beta < 1) \tag{1.6}$$

This equation indicates a broad distribution of relaxation time near the glass transition

and it was assumed that such a broad distribution of relaxation time was attributed to the dynamical heterogeneity of glass. Various studies by light scattering, photo probe and NMR methods have identified dynamical heterogeneity on various scales [41-44] and Zorn et al. and Kanaya et al. evaluated dynamical heterogeneity of glass-forming materials by inelastic or quasielastic neutron scattering based on non-Gaussian parameter A_0 [45,46].

Concerning the size of CRR, various experiments or simulations have been done and it was found that CRR has not been estimated from structural analysis, hence CRR is considered as dynamical characteristic length. The characteristic length of the CRR was estimated to be 2∼6 nm in some molecular glass [47-49] and polymeric glasses [50-54] near T_g, however CRR size is strongly dependent on theories and evaluation methods. The most effective and simplest way to evaluate the size of CRR without any assumption is performing experiments concerning the finite size effect. As the size of the glass-forming materials approaches the cooperativity length scale, the anomaly or drastic change would be observed near the glass transition temperature or the α process. Based on this idea, experiments for the finite size effect have been done using controlled pore glasses (CPGs) [55], Vycor glass [56], the regular porous silicates (MCM-41 and SBA-15) as a confining media [57,58]. By incorporating glass-forming into confining media, confinement systems exhibit different behaviour compared to bulk system. Priss et al. first studied the confinement effect on the α process with glycerol using Vycor glass by dielectric relaxation and found the broadening of the relaxation time compared to bulk [59]. First they interpreted this broadening as the change of the size of CRR by spatial confinement. Richert et al. also reported some results from dielectric measurements on propylene glycol (PG) and two poly(propylene glycol)s with different molecular weights confined in CPGs and they observed the broadening of α-process by confinement and increase of T_0, where T_0 is Vogel-Fulcher temperature [60]. With further investigations, they observed another additional relaxation process below the α relaxation frequency and this additional process was attributed to the interaction of a few layers of the confined liquid with the pore. Richert et al. also further

extended their work, and they found that the additional process disappeared with surface modification of CPGs's wall by silanization [61]. By the surface modification, it seemed to be possible to evaluate pure finite size effect. However, situation is not so simple because some of the dielectric works reported an additional relaxation at low frequency for some molecules even after the surface treatment of confining media [62-65]. In addition to interaction between confining materials and sample, other factors like surface and interface effects affect the experimental results very much, owing to the high surface to volume ratio. Kramer et al. studied the dynamics of propylene glycol (PG), butylene glycol (BG) and pentylene glycol (PeG) confined to porous glasses with the pore size of 7.5, 5.0 nm and 2.2 nm [66]. They reported no or slight acceleration effect of the confinement on α process of PG, BG and PeG in 7.5 nm and 5 nm. On the other hand, all the samples exhibited slower dynamics than that of bulk confined in 2.5 nm pores. They used a three-layer model assuming an interfacial layer, surface layer and bulk-like layer in order to explain the relaxation mechanism.

Therefore it is still difficult to understand the exact reasons for observed results and extract the genuine finite size effect with decreasing the size of confinement. Similar situation holds for polymer thin film systems. Exact evaluation of surface or interface effect or surface interaction effect on the dynamics is indispensable in order to extract pure finite size effect or CRR size definitely. The advantage of polymer thin film experiments is that the confining dimension or the thickness can be varied easily and the second advantage is the inhibition of crystallization that trigger dewetting or collapse the flat surface with atactic polymer. In the next section, we would like to survey the prior works on glass transition and related topics of polymer thin films.

1.3 Prior Works on Glass Transition of Polymer Thin Films

Beaucage et al. first reported the possibility of the investigation of glass transition of polymer thin films by ellipsometry method [67]. Keddie et al. studied the thickness dependence of T_g systematically by ellipsometry and found that T_g decreased with film

thickness for Polystyrene (PS) that has relatively small interaction with the Si substrate [15,68]. After his pioneering works, the various researchers studied the thickness dependence of T_g by various methods like ellipsometry [17,68,69], X-ray/neutron reflectivity [16-18,70], positron annihilation spectroscopy (PALS) [71], local thermal analysis [72], fluorescence probe intensity [73,74], lateral force microscopy [9] and differential scanning nanocalorimetry [75,76]. From their vigorous researches, it was found that the decrease of T_g was caused by the existence of mobile surface layer and T_g of such mobile layer was lower than that of bulk. Kawana et al. collected the reported results on the thickness dependence of T_g of PS supported on Si wafer from various techniques in one figure and the obtained data seemed to be well described by one single curve regardless of molecular weight (M_w) [69], as shown in Figure 1-6.

$$T_g(h) = T_g(\infty)\Big(1 - \Big(\frac{A}{h}\Big)^{\delta}\Big), \tag{1.7}$$

where h is the thickness of film, $T_g(\infty)$ is T_g of bulk and A and the exponent δ are constants. According to the Kawana's investigation, the best-fit parameters were A = 83 Å, and the exponent δ = 1.1, respectively. Much larger reduction of T_g was observed for freely-standing thin films than that for supported films and even the M_w dependence of T_g was reported with relatively high M_w [77,78].

The glass transition temperature of polymer thin film was well characterized by various methods, however the definite mechanism of the glass transition of polymer thin films is still unknown. As noted in the former section, the glass transition is the relaxational process or the dynamical process, we have to study the dynamical behaviour of polymer thin films directly in order to understand the glass transition of polymer thin films. So far, the dynamical studies on polymer thin films were performed using dielectric relaxation [79-81], dynamic light scattering (DLS) [82], Near-edge X-ray absorption fine structure (NEXAFS) [83], X-ray photon correlation spectroscopy (XPCS) [84], scanning probe microscopy [7], dynamical mechanical analysis (DMA) [85], inelastic neutron scattering [86,87], low energy muon [88] and second-harmonic generation (SHG) [89]. Other approaches using different techniques such as hole growth [90], dewetting dynamics [91,92] and nanobubble inflation [93] have been conducted for

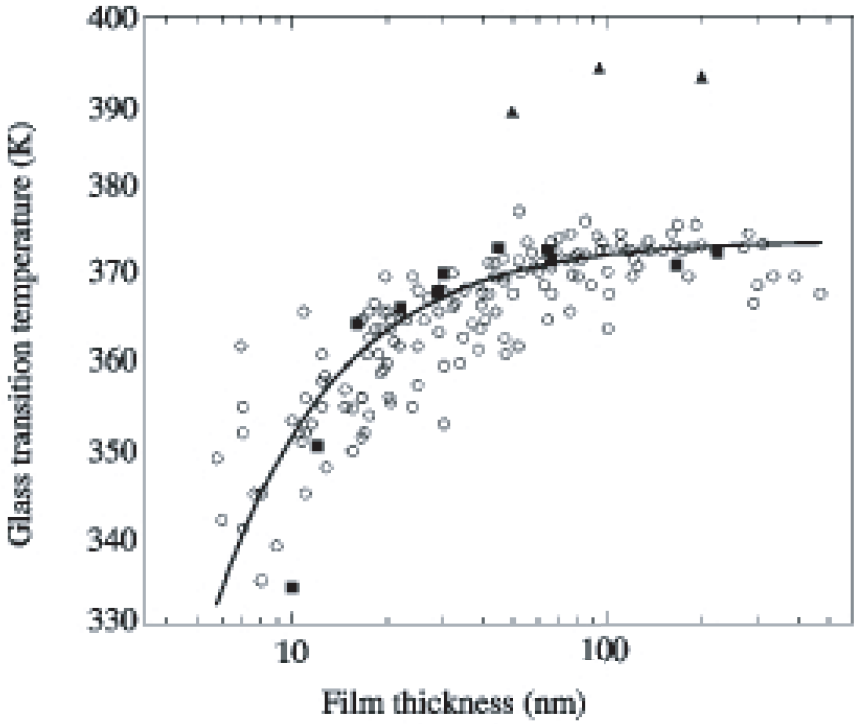

Figure 1.6: Previously measured values of the glass transition temperature T_g for PS supported on silicon and solid line is the result of fit with (1.7) [69].

the understanding of the rheological behaviour of polymer thin films with somewhat different point of view. The direct dynamical information, which cannot be obtained from the structural studies only has been identified from above dynamical studies, however the collected results were still not sufficient for the fully understanding of the mechanism or the singularity of glass transition behaviour of polymer thin films. We considered that continuing the dynamical studies on polymer thin films was still needed in this field.

1.4 Motivation of This Work

We felt the importance of studying the polymer thin films from the dynamical point of view. Neutron scattering covers relatively fast and microscopic dynamics compared to other techniques as shown in Figure 1-1. It was supposed that the microscopic dynamics of polymer chains in confined systems would be different from those of bulk state from the results on the dynamical measurements of molecule with porous media by inelastic neutron scattering [94] and the studies on microscopic dynamics of polymer thin films have not been conducted so much, as far as the author knows. There have been some experimental reports that polymer chain conformation in a thin film was different from bulk state from small angle neutron scattering (SANS) study [95-97]. We considered that change of chain conformation would affect the dynamics and investigating the microscopic dynamics would offer some useful dynamical information, which has not been reported so far. For this purpose, inelastic neutron scattering is suitable and it can offer both static and dynamical structure. In fact, Kanaya et al. reported that the decrease of thermal expansivity with film thickness in glassy state was partly related to the increase of harmonic constant that was evaluated from inelastic neutron scattering [98]. Inelastic neutron scattering would offer the possibility of understanding the unresolved problems in the field of polymer thin films. There have been some works on the dynamics of polymer thin films with inelastic neutron scattering method [92,93], however the reported data were mainly focused on elastic scattering due to the extremely low inelastic scattering intensity. The information from inelastic and

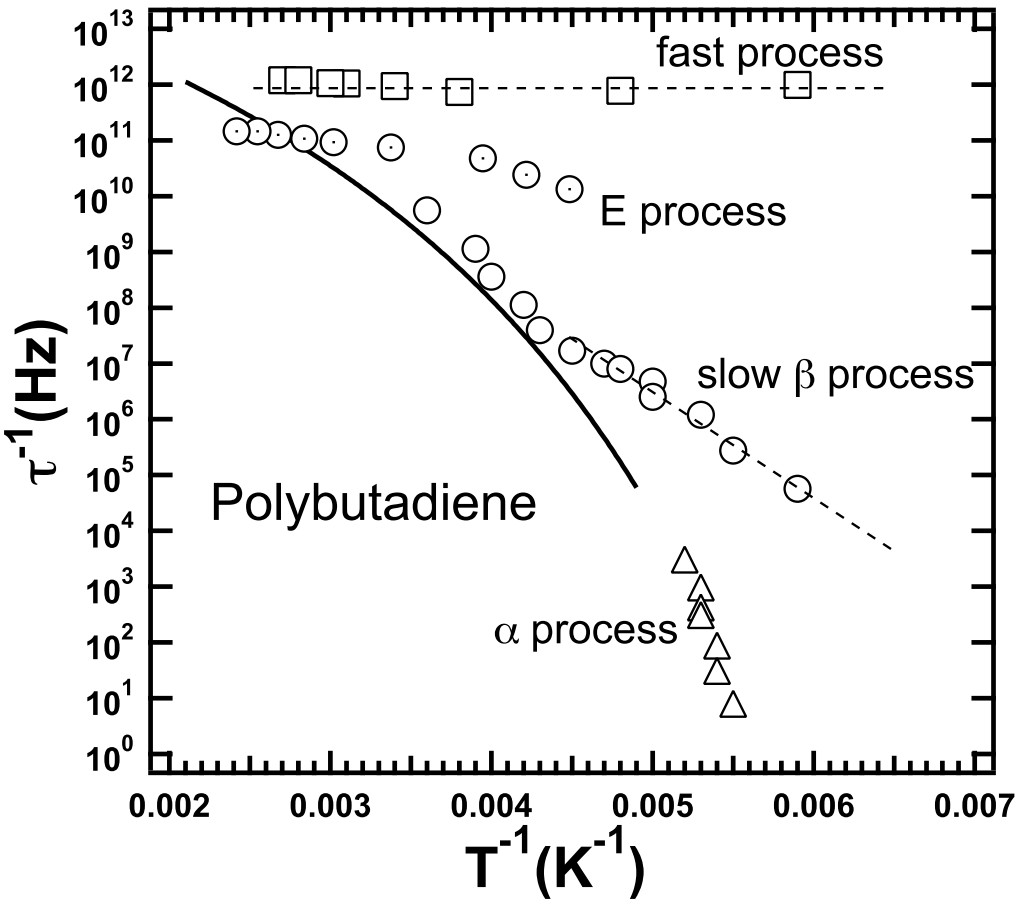

Figure 1.7: Relaxation time map of polybutadiene (PB) observed with various kinds of methods [99].

quasielastic scattering out of the elastic scattering includes various dynamical information like the relaxation time or the excitation energy, which cannot be obtained from temperature dependence of the elastic scattering only. We would like to focus on the inelastic or quasielastic scattering from polymer thin films.

In addition to the α process that is mainly related to the glass transition, there exist several relaxations, which are related to local motion, conformational change, as indicated in Figure 1-7 [99]. For the clarification of the mechanism of glass transition of polymer thin films, we also have to understand the glassy dynamics as well. We don't consider that there exists no correlation between the α process and the glassy dynamics, for example, the so-called pico-second "fast process" that onsets far below T_g. Formerly MCT predicted the correlation between the fast process and the α process, although it didn't work for the observed data well, as already shown in former section, however there exist some experimental results that connect two relaxational processes. Buchenau et al. reported that the inverse of the mean square displacement difference between the values in the disordered and ordered phase was linearly proportional to the logarithm of the macroscopic physical value viscosity η for selenium (Se) in the very broad temperature range [100]. This results support the free-volume theory and they suggested that free volume could be replaced by the mean square displacement of fast motion. Kanaya et al. reported that the onset temperature of fast process was at around Vogel-Fulcher temperature T_0 for polybutadiene (PB) and they also reported the validity of above notion with PB [99]. As for PS, Kanaya et al. suggested the possibility of the assistance of the onset of glass transition by the fast process at above T_g [99]. The correlation between fragility index and dynamical heterogeneity that was evaluated from inelastic neutron scattering (ps dynamics) has been studied for disordered system [45] and Sokolov et al. also reported the correlation between fragility index and the intensity ratio of the relaxation process to the Boson peak [101]. Considering these experimental results, the glassy dynamics is closely related to glass transition and cannot be ignored for the investigation of glass transition. In addition, the glassy state of polymer thin films have not been studied very much, therefore broad

temperature range measurements from far below T_g seemed to be needed in order to understand the glass transition and related phenomenon of polymer thin films from the viewpoint of dynamics. We would like to study the glassy dynamics and glass transition of polymer thin film by inelastic and quasielastic neutron scattering.

1.5 Outline of This Thesis

The aim of this thesis is to reveal the mechanism of glass transition and glassy dynamics of polymer thin films by inelastic and quasielastic neutron scattering. We will clarify the singularity of the dynamics of polymer thin films compared to bulk in the broad temperature range, mainly focusing on the understanding of glass transition of polymer thin films. The contents of this thesis are as follows;

In Chapter 2, the fundamental theories of inelastic and quasielastic neutron scattering are described and these theories give the physical meaning to the observable in the later chapters. We will introduce the instruments used in this study and the detailed sample preparation in the following two sections.

In Chapter 3, we surveyed the effect of Al on the glass transition temperature of polystyrene thin films with ellipsometry using Al deposited Si wafer as a substrate. The obtained data was compared with that from X-ray reflectivity (XR) and the effect of Al on T_g of polystyrene thin films is discussed.

In Chapter 4, the glassy dynamics of polymer thin films was studied with inelastic and quasielastic neutron scattering method in meV region. Thickness dependence of mean square displacement $< u^2 >$ was investigated and it was found that $< u^2 >$ decreased with thickness. In order to analyze the origin of decrease of mobility with thickness, we focused on the inelastic and quasielastic scattering from thin films. In order to understand the observed results, we assumed two candidates for the decrease of mobility with thickness, one is spatial confinement effect and the other is interface effect.

We observed the decrease of $< u^2 >$ with film thickness in the former chapter (Chapter 4) and we considered two possible causes in Chapter 5. In order to clarify

which factor is dominant, we studied M_w dependence of $< u^2 >$ by inelastic neutron scattering.

In Chapter 6, we studied the dynamics of thin films using macroscopically isotropic samples in the former chapters, and we didn't know whether interfacial layer affect the mobility of chain and the molecular motion is really isotropic. In order to confirm the above problem, we studied the motions in the parallel and perpendicular to surface. If the interfacial layer existed, the increase of heterogeneity is expected compared to bulk. We investigated the dynamical heterogeneity of polymer thin films in terms of non-Gaussian parameter A_0 and obtained the dynamical information from interface layer.

In Chapter 7, the glass transition of polymer thin film was studied with a relatively high energy resolution spectrometer and T_g was evaluated from the temperature dependence of elastic intensity. We compared the evaluated glass transition temperature T_g with that from the ellipsometry measurements and discussed the singularity of dynamics of polymer thin films.

In Chapter 8, the distribution of T_g in polymer thin films was studied with trilayer stacked thin film of d-PS/h-PS/d-PS by neutron reflectivity. The temperature dependence of thickness and roughness of each layer was studied carefully and discussed the difference of mobility of each layer.

In the end of the thesis, the whole results and discussions are summarized.

References

[1] J. J. O'Malley, H. R. Thomas, and G. M. Lee, Macromolecules, **12**, 496 (1979).

[2] M. Stamm, S. Huttenbach, G. Reiter, and T. Springer, Europhys. Lett. **14**, 451, (1991).

[3] K. Tanaka, S. Yoon, A. Takahara, and T. Kajiyama, Macromolecules, **28**, 934 (1995).

[4] G. L. Gaines, Jr. *Insoluble Monolayers at Liquid-Gas Interfaces*, (Interscience, 1966).

[5] A. Ulman, *An Introduction to Ultrathin Organic Films*, (Academic Press., 1991).

[6] *Practiacal Surface Analysis-Vol.2- Ion and Neutral Spectroscopy*, edited by D. Briggs and M. P. Seah, (Jhon Wiley, 1992).

[7] T. Kajiyama, K. Tanaka, and A. Takahara, Macromolecules, **30**, 280 (1997).

[8] J. H. van Zanten, W. E. Wallace, and W. Wu, Phys. Rev. E **53**, R2053 (1996).

[9] T. P. Russel, Mat. Sci. Rep. **5**, 171 (1990).

[10] L. J. Norton, E. J. Kramer, F. S. Bates, M. D. Gehlsen, R. A. L. Jones, A. Karim, G. P. Felcher, and R. Kleb, Macromolecules, **28**, 8621 (1995).

[11] S. J. Whitlow, and R. P. Wool, Macromolecules, **22**, 2648 (1989).

[12] X. Zhao, W. Zhao, J. Sokolov, M. H. Rafailivich, S. A. Schwarz, B. J. Wilkens, R. A. L. Jones, and E. J. Kramer, Macromolecules, **24**, 5991 (1991).

[13] E. J. Kramer, P. F. Green, and C. J. Palmstrom, Makromol. Chem. Rapid Commun. **5**, 159 (1984).

[14] R. J. Composto, E. J. Kramer, and D. M. White, Nature, **328**, 234 (1987).

[15] J. L. Keddie, R. A. L. Jones, and R. A. Cory, Europhys. Lett. **27**, 59 (1994).

[16] W. J. Orts, J. H. vanZanten, W. W.-l. Wu, and S. K. Satija, Phys. Rev. Lett. **71**, 867 (1993).

[17] T. Miyazaki, K. Nishida, and T. Kanaya, Phys. Rev. E **69**, 061803 (2004).

[18] W. E. Wallace, J. H. van Zanten, and W. L. Wu, Phys. Rev. E **52**, R3329 (1995).

[19] J. A. Forrest, and K. Dalnoki-Veress, Adv. Colloid Interface Sci. **94**, 167 (2001).

[20] M. Alcoutlabi, and G. B. McKenna, J. Phys. Condens. Matter, **17**, R461 (2005).

[21] G. Adam, and, J. H. Gibbs, J. Chem. Phys. **43**, 139 (1965).

[22] P. K. Dixon, Phys. Rev. B **42**, 8179 (1990).

[23] D. L. Sidebottom, and C. M. Sorensen, Phys. Rev. B **40**, 461 (1989).

[24] O. Yamamuro, I. Tsukushi, T. Matsuo, K. Takeda, T. Kanaya, and K. Kaji, J. Chem. Phys. **106**, 2997 (1997).

[25] O. Yamamuro, Y. Madokoro, H. Yamasaki, T. Matsuo, I. Tsukushi, and K. Takeda, J. Chem. Phys. **115**, 9808 (2001).

[26] Y. H. Zhao, J. Non-Cryst. Solids, **352**, 5578 (2006).

[27] O. G. Oblad, and R. E. Newton, J. Am. Chem. Soc. **59**, 2495 (1937).

[28] M. H. Cohen, and D. Turnbull, J. Chem. Phys. **31**, 1164 (1959).

[29] J. D. Ferry, and L. D. Grandine, Jr., J. Appl. Phys. **24**, 911 (1953).

[30] M. L. Williams, R. E. Landel, and J. D. Ferry, J. Am. Chem. Soc. **77**, 3701 (1955).

[31] H. Vogel, Phys. Z **22**, 645 (1921).

[32] D. J. Plazek. X. D. Zheng, and K. L. Ngai, Macromolecules, **25**, 4920 (1992).

[33] W. Götze, Liquids, Freezing, and the Glass Transition, edited by J. P. Hansen, (Elsevier, 1991).

[34] B. Frick, and D. Richter, Science, **267**, 1939 (1995).

[35] K. Kawasaki, Busseikenkyu, **80**, 503 (2003).

[36] T. Odagaki, and Y. Hiwatari, Phys. Rev. A **41**, 929 (1990).

[37] H. Tanaka, J. Chem. Phys. **111**, 3163 (1999).

[38] S. Sastry, Nature, **409**, 164 (2001).

[39] A. Onuki, A. Furukawa, and A. Minami, Pramana-Journal of Physics, **64**, 661 (2005).

[40] G. Williams, and D. C. Watts, Trans. Faraday Soc. **67**, 1323 (1971).

[41] M. T. Cicerone, F. R. Blackburn, and M. D. Ediger, J. Chem. Phys. **102**, 471 (1995).

[42] R. Bohmer, G. Hinze, G. Diezemann, B. Geil, and H. Sillescu, Europhys. Lett. **36**, 55 (1996).

[43] M. T. Cicerone, and M. D. Ediger, J. Chem. Phys. **103**, 5684 (1995).

[44] K. Schmit-Rohr, and H. W. Spiss, Phys. Rev. Lett. **66**, 3020 (1991).

[45] R. Zorn, Phys. Rev. B **61**, 6249 (1997).

[46] T. Kanaya, I. Tsukushi, and K. Kaji, Prog. Theor. Phys. Suppl. **126**, 133 (1997).

[47] E. Donth, J. Non-Cryst. Solids. **53**, 325 (1982).

[48] F. Fujara, B. Geil, H. Sillescu, and G. Flescher, Z. Phys. B **88**, 195 (1992).

[49] O. Yamamuro, I. Tsukushi, A. Lindqvist, S. Takahara, M. Ishikawa, and T. Matsuo, J. Phys. Chem. B **102**, 1605 (1998).

[50] C. G. Robertson, and X. R. Wang, Macromolecules, **37**, 4266 (2004).

[51] U. Tracht, M. Wilhelm, A. Heuer, H. Feng, K. Schmidt-Rohr, and H. W. Spiss, Phys. Rev. Lett. **81**, 2727 (1998).

[52] S. A. Reinsberg, X. H. Qiu, M. Wilhelm, H. W. Spiss, and M. D. Ediger, J. Chem. Phys. **114**, 7299 (2001).

[53] P. D. Hong, W. T. Chuang, W. J. Yeh, and J. L. Lin, Polymer, **43**, 6879 (2002).

[54] E. Donth, Acta Polym. **35**, 120 (1984).

[55] W. Haller, Nature, **206**, 693 (1965).

[56] M. C. Bellissent-Funel, J. Lal, and L. Bosio, J. Chem. Phys. **98**, 4246 (1993).

[57] C. Alba-Scimonecso, G. Dosseh, E. Dumont, B. Frick, B. Geil, D. Morineau, V. Teboul, and Y. Xia, Eur. Phys. J. E **12**, 19 (2003).

[58] A. Watanabe, K. Kaneko, T. Iiyama, R. Radhakrishman, and K. E. Gubbins, J. Phys. Chem. B **103**, 7071 (1999).

[59] P. Priss, D. Daoukaki, L. Apekis, and C. Christodoulides, J. Phys. Condes. Matter, **6**, L325 (1994).

[60] J. Schuller, Yu. B. Mel'nichenko, R. Richert, and E. W. Ficher, Phys. Rev. Lett. **73**, 2224 (1994).

[61] Y. B. Melnichenko, J. Schuller, R. Richert, B. Ewen, and C. K. Loong, J. Chem. Phys. **103**, 2016 (1995).

[62] G. Barut, P. Priss, R. Plester, and G. Nimtz, Phys. Rev. Lett. **80**, 3543 (1998).

[63] M. Arndt, R. Stannarius, H. Groothus, H. Hempel, and F. Kremer, Phys. Rev. Lett. **79**, 2077 (1997).

[64] J. Schuller, R. Richert, and E. W. Fisher, Phys. Rev. B **52**, 15232 (1995).

[65] A. Schönels, and R. Stauga, J. Non-Cryst. Solids, **235**, 450 (1998).

[66] W. Gorbatschow, M. Arndt, R. Stannarius, and F. Kremer, Europhys. Lett. **35**, 719 (1996).

[67] G. Beaucage, R. Composto, and R. S. Stein, J. Poly. Sci. Polym. Phys. Ed., **31**, 319 (1993).

[68] J. L. Keddie, R. A. L. Jones, and R. A. Cory, Faraday. Discuss. **98**, 219 (1994).

[69] S. Kawana, and R. A. L. Jones, Phys. Rev. E **63**, 21501 (2001).

[70] T. Kanaya, T. Miyazaki, H. Watanabe, K. Nishida, H. Yamano, S. Tasaki, and D. B. Bucknall, Polymer, **44**, 3769 (2003).

[71] D. B. DeMaggio, W. E. Frieze, D. W. Gidley, M. Zhu, H. A. Hristov, and A. F. Yee, Phys. Rev. Lett. **78**, 1524 (1997).

[72] D. S. Fryer, P. F. Nealey, and J. J. de Pablo, Macromolecules, **33**, 6439 (2000).

[73] C. J. Ellison, and J. M. Torkelson, Nature Mater. **2**, 695 (2003).

[74] R. D. Priestley, C. J. Ellison, L. J. Broadbelt, and J. M. Torkelson, Science, **309**, 456 (2005).

[75] M. Yu. Efremov, E. A. Olson, M. Zhang, Z. Zhang, and L. H. Allen, Macromolecules, **37**, 4607 (2004).

[76] M. Yu. Efremov, E. A. Olson, M. Zhang, Z. Zhang, and L. H. Allen, Phys. Rev. Lett. **91**, 085703 (2003).

[77] J. A. Forrest, K. Dalnoki-Veress, J. R. Stevens, and J. R. Dutcher, Phys. Rev. Lett. **77**, 2002 (1996).

[78] K. Dalnoki-Veress, J. A. Forrest, C. Murray, C. Gigault, and J. R. Dutcher, Phys. Rev. E **63**, 31801 (2001).

[79] K. Fukao, and Y. Miyamoto, Phys. Rev. E **61**, 1743 (2001).

[80] K. Fukao, and Y. Miyamoto, Phys. Rev. E **64**, 011803 (2001).

[81] K. Fukao, Eur. Phys. J. E **12**, 119 (2003).

[82] J. A. Forrest, C. Svanberg, K. Révész, M. Rodahl, L. M. Torell, and B. Kasemo, Phys. Rev. E **58**, R1226 (1998).

[83] Y. Liu, T. P. Russell, M. G. Samant, J. Stöhr, H. R. Brown, A. Cossy-Favre, and J. Diaz, Macromolecules, **30**, 7768 (1997).

[84] H. Kim, A. Rühm, L. B. Lurio, J. K. Basu, J. Lal, D. Lumma, S. G. J. Mochrie, and S. K. Sinha, Phys. Rev. Lett. **90**, 068302 (2003).

[85] K. Akabori, K. Tanaka, T. Nagamura, A. Takahara, and T. Kajiyama, Macromolecules, **38**, 9735 (2005).

[86] B. Frick, K. Dalnoki-Veress, J. A. Forrest, J. Dutcher, C. Murray and A. Higgins, Eur. Phys. J. E **12**, s01, 93 (2003).

[87] C. L. Soles, J. F. Douglas, W. Wu, and R. M. Dimeo, Phys. Rev. Lett. **88**, 037401 (2002).

[88] F. L. Pratt, T. Lancaster, M. L. Brooks, S. J. Blundell, T. Prokscha, E. Morenzoni, A. Suter, H. Luetkens, R. Khasanov, R. Scheuermann, U. Zimmermann, K. Shinotsuka, and H. E. Assender, Phys. Rev. B **72**, 121401(R) (2005).

[89] D. B. Hall, J. C. Hooker, and J. M. Torkelson, Macromolecules, **30**, 667 (1997).

[90] G. Reiter, Eur. Phys. Lett. **23**, 579 (1993).

[91] P. F. Green, and V. Ganesan, Eur. Phys. J. E **12**, 449 (2003).

[92] G. Reiter, Macromolecules, **27**, 3046 (1994).

[93] P. O'Connell, and G. B. McKenna, Science, **307**, 1760 (2005).

[94] R. Zorn, L. Hartmann, B. Frick, D. Richter, and F. Kremer, J. Non-Cryst. Solids. **307**, 547 (2002).

[95] J. Kraus, P. Müeller-Buschbaum, T. Kuhlmann, D. W. Schubert, and M. Stamm, Europhys. Lett. **49**, 210 (2000).

[96] R. L. Jones, S. K. Kumar, D. L. Ho, R. M. Briber, and T. P. Russell, Nature, **400**, 146 (2000).

[97] A. Brulet, F. Boue, A. Menelle, and J. P. Cotton, Macromolecules, **35**, 8878 (2002).

[98] T. Kanaya, T. Miyazaki, R. Inoue, and K. Nishida, Phys. Stat. Sol. (b) **242**, 595 (2005).

[99] T. Kanaya, and K. Kaji, Adv. Polym. Sci. **154**, 87 (2001).

[100] U. Buchenau, and R. Zorn, Europhys. Lett. **18**, 523 (1992).

[101] A. P. Sokolov, E. Rossler, A. Kisliuk, and D. Quitmann, Phys. Rev. Lett. **71**, 2062 (1993).

Chapter 2

Basic Theories of Scattering and Experimental Techniques

2.1 Fundamental Theories of Neutron Scattering

In this thesis, we mainly used inelastic neutron scattering method for the investigation of dynamics of polymer thin films. we describe the basic theories of inelastic neutron scattering. After brief description of theories of elastic scattering, we describe the theories of inelastic neutron scattering and some models for quasielastic neutron scattering in the following sections

2.1.1 Scattering Theory: Elastic Scattering

We consider the scattering of a neutron by a particle at $\boldsymbol{r'}$ and incident neutron is represented by plane wave $\exp(i\boldsymbol{k}\cdot\boldsymbol{r})$, where $\boldsymbol{r}$ is the position vector and $\boldsymbol{k}$ is the wave vector. The value of $\boldsymbol{k}$ is equal to $2\pi/\lambda$, where λ is the de Broglie wavelength. Detail of the scattering geometry is shown in Figure 2-1 [1]. Schrödinger wave function of this system is described by below

$$-\frac{\hbar^2}{2m_n}\nabla^2\Psi(\boldsymbol{r}) + V(\boldsymbol{r})\Psi(\boldsymbol{r}) = E\Psi(\boldsymbol{r}), \tag{2.1}$$

where m_n is the mass of neutron. Using the Born approximation, we have a solution of the Schrödinger equation.

$$\Psi(\boldsymbol{r}) = \exp(i\boldsymbol{k}\cdot\boldsymbol{r}) - \frac{1}{4\pi}\int \frac{\exp[i\boldsymbol{k'}\cdot(\boldsymbol{R'}+\boldsymbol{r'})]}{|\boldsymbol{R'}|}\exp[i(\boldsymbol{k}-\boldsymbol{k'})\cdot\boldsymbol{r'}]\times\frac{2m_n}{\hbar^2}V(\boldsymbol{r'})d\boldsymbol{r'}, \tag{2.2}$$

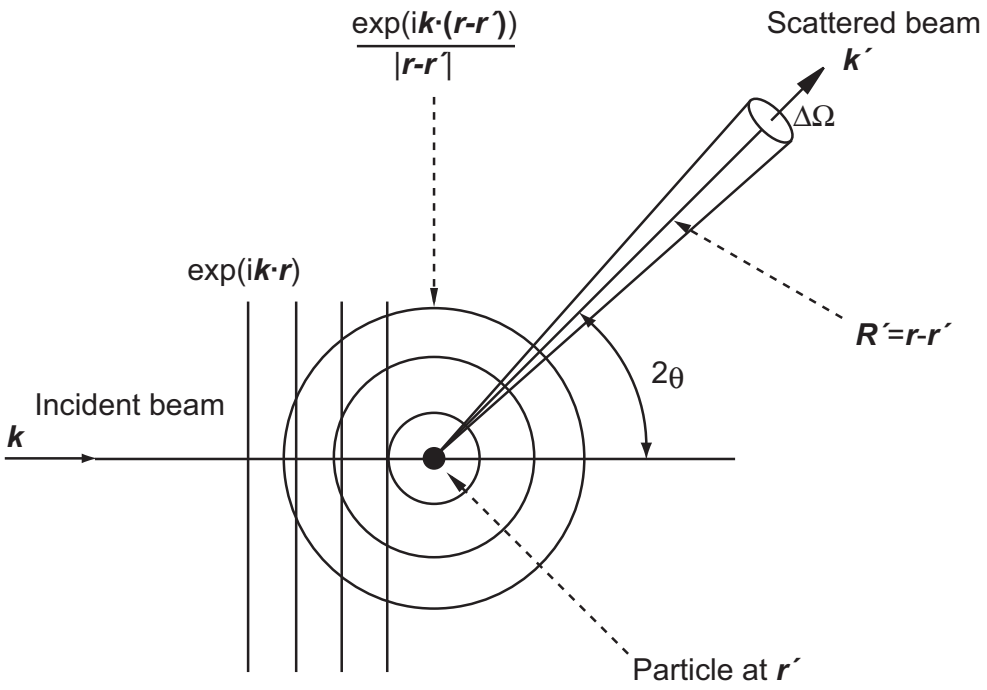

Figure 2.1: Scattering of plane wave by spherically symmetric potential field.

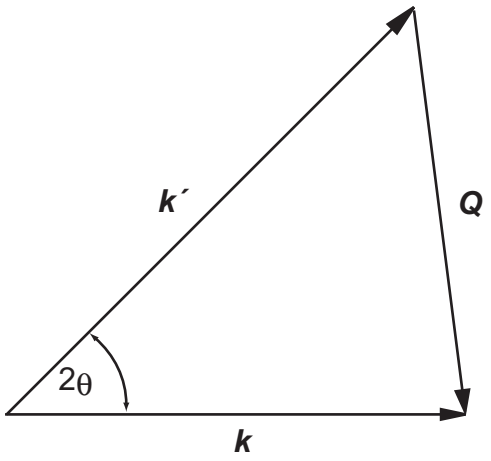

Figure 2.2: Relation between wave vector $\boldsymbol{k}$ for incident neutron and $\boldsymbol{k'}$ for the scattering neutron. 2θ is scattering angle.

where $\boldsymbol{R'} = \boldsymbol{r} - \boldsymbol{r'}$ and $\boldsymbol{k'}$ is the wave vector of scattered neutron. If there are n_0 neutrons incident on unit area in unit time, and if $d\Omega$ is an element of solid angle in which numbers of neutron scattered from $\boldsymbol{r'}$ is counted, then this number is proportional both to n_0 and to $d\Omega$. The factor of proportionality is called differential cross-section $d\sigma/d\Omega$. In this case, the plane wave term $\exp(i\boldsymbol{k}\cdot\boldsymbol{r})$ represents as wave of unit density and the spherically-scattered wave $f\exp(i\boldsymbol{k}\cdot\boldsymbol{r})/\boldsymbol{R'}$, represents a wave of density $|f|^2/R'^2$, where the amplitude f is described below

$$f = -\frac{1}{4\pi}\int \exp[i(\boldsymbol{k}-\boldsymbol{k'})\cdot\boldsymbol{r'}] \times \frac{2m_n}{\hbar^2}V(\boldsymbol{r'})d\boldsymbol{r'} \tag{2.3}$$

The number of scattered neutrons per second that cross $R'^2 d\Omega$ in the solid angle $d\Omega$ is

$$\frac{|f|^2}{R'^2}\cdot\frac{\hbar k'}{m_n}\cdot R'^2 d\Omega, \tag{2.4}$$

therefore differential cross-section is written in the below expression

$$\frac{d\sigma}{d\Omega} = \frac{1}{N}\cdot\frac{|f|^2}{R'^2}\cdot\frac{\hbar k'}{m_n}\cdot R'^2 = \frac{k'}{k}\left|\frac{1}{4\pi}\int \exp[i(\boldsymbol{k}-\boldsymbol{k'})\cdot\boldsymbol{r'}]\frac{2m_n}{\hbar^2}V(\boldsymbol{r'})d\boldsymbol{r'}\right|^2 \tag{2.5}$$

In the case of elastic scattering k=k', $\boldsymbol{Q}$ is given as $\boldsymbol{k}-\boldsymbol{k'}$, as shown in Figure 2-2.

$$\frac{d\sigma}{d\Omega} = \left|\frac{1}{4\pi}\int \exp[i\boldsymbol{Q}\cdot\boldsymbol{r'}]\frac{2m_n}{\hbar^2}V(\boldsymbol{r'})d\boldsymbol{r'}\right|^2 \tag{2.6}$$

$$|\boldsymbol{Q}| = \frac{4\pi\sin\theta}{\lambda} \tag{2.7}$$

From the sequence of derivation, it was found that the amplitude of scattering is proportional to Fourier transform of scattering potential $V(\boldsymbol{r})$ [see eq. (2.6)].

Scattering from A Single Nucleus

$V(\boldsymbol{r})$ is the interaction potential between neutron and atomic nucleus and it is restricted to nuclear dimensions. In the case of thermal neutron, $\exp(i\boldsymbol{Q}\cdot\boldsymbol{r'})$ is almost equal to 1, therefore f is described by below relation

$$f = -\frac{1}{4\pi}\int_{\text{nucleus}} \frac{2m_n}{\hbar^2}V(\boldsymbol{r})d\boldsymbol{r}. \tag{2.8}$$

The quantity $-f$ is called the neutron scattering length of the nucleus and denoted by b, which is inherent value of nucleus. Since b is independent of $\boldsymbol{Q}$, the differential cross-section $d\sigma/d\Omega$ for single nucleus is isotropic and the total cross-section σ_{tot} is given by

$$\sigma_{tot} = \int \frac{d\sigma}{d\Omega} d\Omega = 4\pi b^2. \tag{2.9}$$

Scattering from Many Nuclei. Coherent and Incoherent Scattering

Next we consider a case of scattering from many nuclei. The phase of the scattered radiation is $\exp(i\boldsymbol{Q}\cdot\boldsymbol{R})$, and hence the differential scattering cross-section for many fixed nuclei is

$$\begin{aligned}\frac{d\sigma}{d\Omega} = \left|\sum_{\boldsymbol{R}} b_{\boldsymbol{R}} \exp(i\boldsymbol{Q}\cdot\boldsymbol{R})\right|^2 = \sum_{\boldsymbol{R},\,\boldsymbol{R}'} b_{\boldsymbol{R}} b_{\boldsymbol{R}'} \exp[i\boldsymbol{Q}\cdot(\boldsymbol{R}-\boldsymbol{R}')] = \sum_{\boldsymbol{R}} b_{\boldsymbol{R}}^2 \\ + {\sum_{\boldsymbol{R},\,\boldsymbol{R}'}}' b_{\boldsymbol{R}} b_{\boldsymbol{R}'} \exp[i\boldsymbol{Q}\cdot(\boldsymbol{R}-\boldsymbol{R}')],\end{aligned} \tag{2.10}$$

the second term in (2.10) excludes the summation in the case $\boldsymbol{R}=\boldsymbol{R}'$, and first term is equal to $N < b_{\boldsymbol{R}}^2 >$, where N is the number of nuclei and there is no correlation between $b_{\boldsymbol{R}}$ and$b_{\boldsymbol{R}'}$, hence $< b_{\boldsymbol{R}} b_{\boldsymbol{R}'} >=< b_{\boldsymbol{R}} >< b_{\boldsymbol{R}'} >=< b_{\boldsymbol{R}} >^2$ and second term can be written

$$\begin{aligned}N < b_{\boldsymbol{R}} >^2 {\sum}' \exp[i\boldsymbol{Q}\cdot(\boldsymbol{R}-\boldsymbol{R}')] = -N < b_{\boldsymbol{R}} >^2 \\ + N < b_{\boldsymbol{R}} >^2 \sum \exp[i\boldsymbol{Q}\cdot(\boldsymbol{R}-\boldsymbol{R}')],\end{aligned} \tag{2.11}$$

using $N < b_{\boldsymbol{R}} >^2$ and (2.11), (2.10) can be written as

$$\frac{d\sigma}{d\Omega} = N(< b^2 > - < b >^2) + N < b >^2 \left|\sum \exp(i\boldsymbol{Q}\cdot\boldsymbol{R})\right|^2. \tag{2.12}$$

The first term is known as incoherent scattering cross-section and the second term is known as coherent scattering cross-section. The distinction between coherent and incoherent cross-section can be conducted easily. We consider $b_{\boldsymbol{R}}$ as an example.

$$b_{\boldsymbol{R}} =< b > + \Delta b_{\boldsymbol{R}}, \tag{2.13}$$

where $< b >$ is the average amplitude and $\Delta b_{\boldsymbol{R}}$ indicates the deviation from average. The intensity was divided into two parts coherent scattering and incoherent scattering.

We have the total scattering cross-section per atom

$$\sigma_{tot} = 4\pi < b^2 >= \sigma_{coh} + \sigma_{incoh} = 4\pi < b >^2 + 4\pi(< b^2 > - < b >^2). \tag{2.14}$$

2.1.2 Scattering Theory: Inelastic Scattering

Eigenstate Formulation

When the energy conservation law is satisfied, the scattering amplitude given by (2.15)

$$\sum_{\boldsymbol{R}} b_{\boldsymbol{R}} \exp(i\boldsymbol{Q}\cdot\boldsymbol{R}) \tag{2.15}$$

can excite transitions from initial energy state to final energy state and the inelastic scattering happens during the scattering event in which there is a energy transfer. In order to formulate the differential cross-section $d^2\sigma/d\Omega dE'$, we have to consider below four factors together.

(1) the squared modulus of the matrix elements of the scattering amplitude between initial and final states,

$$\sum_{\boldsymbol{R},\,\boldsymbol{R'}} < i|b_{\boldsymbol{R'}} \exp[-i\boldsymbol{Q}\cdot\boldsymbol{R'}]|f >< f|b_{\boldsymbol{R}} \exp[i\boldsymbol{Q}\cdot\boldsymbol{R}]|i > \tag{2.16}$$

(2) the possibility that the initial state is occupied at temperature T

$$P_i = \frac{e^{-E/k_BT}}{\sum_i e^{-E/k_BT}} \tag{2.17}$$

(3) the δ function which ensures the energy-conservation

(4) the ratio of the scattered and incident velocities

The fraction of neutrons scattered per nucleus per unit area into a solid angle $\Delta\Omega$ and with neutron energy in the range $\Delta E'$ can be represented by

$$\frac{d^2\sigma}{d\Omega dE'} = \frac{k'}{k}\sum_{i,f} P_i \sum_{\boldsymbol{R},\,\boldsymbol{R'}} < i|b_{\boldsymbol{R'}} \exp[-i\boldsymbol{Q}\cdot\boldsymbol{R'}]|f >< f|b_{\boldsymbol{R}} \exp[i\boldsymbol{Q}\cdot\boldsymbol{R}]|i > \delta(E - E' - \hbar\omega). \tag{2.18}$$

This expression can be directly evaluated if the eigenstates and energy levels of the scattering system are known. This situation is not always possible, we consider other two formulations.

Time-Dependent Formulation

The time variable is introduced through the integral presentation of the δ function

$$\delta(x) = \frac{1}{2\pi}\int_{-\infty}^{\infty} e^{ixt}dt. \tag{2.19}$$

Using (2.19), we have the below relation

$$\delta(E - E' - \hbar\omega) = \frac{1}{2\pi\hbar}\int_{-\infty}^{\infty} e^{i(t/\hbar)\cdot(E-E'-\hbar\omega)}dt. \tag{2.20}$$

Next, we apply the time-dependent Schrödinger equation

$$i\hbar\frac{\partial\Psi(t)}{\partial t} = H\Psi(t), \Psi(t) = e^{-iHt/\hbar}\Psi(0), \tag{2.21}$$

where $\Psi(t)$ is the wave function at t and $\Psi(0)$ the wave function at t=0. When Ψ_i is the eigenstate of state i with energy E_i,

$$H\Psi_i = E_i\Psi_i, \Psi_i(t) = e^{-iE_it/\hbar}\Psi_i(0). \tag{2.22}$$

We have then the below equation (2.23)

$$\begin{aligned} &< f|b_{\boldsymbol{R}}\exp[i\boldsymbol{Q}\cdot\boldsymbol{R}]|i > \delta(E - E' - \hbar\omega) \\ &= \frac{1}{2\pi\hbar}\int_{-\infty}^{\infty} e^{-i\omega t} < fe^{-itE'/\hbar}|b_{\boldsymbol{R}}\exp[i\boldsymbol{Q}\cdot\boldsymbol{R}]|e^{itE/\hbar}|i > dt \\ &= \frac{1}{2\pi\hbar}\int_{-\infty}^{\infty} e^{-i\omega t} < f|e^{-itH'/\hbar}b_{\boldsymbol{R}}\exp[i\boldsymbol{Q}\cdot\boldsymbol{R}]|e^{itH/\hbar}|i > dt \\ &= \frac{1}{2\pi\hbar}\int_{-\infty}^{\infty} e^{-i\omega t} < f|b_{\boldsymbol{R}}\exp[i\boldsymbol{Q}\cdot\boldsymbol{R}(t)]|i > dt, \end{aligned} \tag{2.23}$$

which gives the scattering amplitude from atom $\boldsymbol{R}$ written in terms of a time-dependent operator $\boldsymbol{R}(t)$. All the states are now at time 0 and we sum over initial states, with probability (2.17), by taking thermal expectation value $<>_T$. Then we obtain a second basic equation for the differential scattering cross-section:

$$\frac{d^2\sigma}{d\Omega dE'} = \frac{k'}{k}\frac{1}{2\pi\hbar}\int_{-\infty}^{\infty} e^{-i\omega t}dt\sum_{\boldsymbol{R},\,\boldsymbol{R'}} < b_{\boldsymbol{R'}}\exp[-i\boldsymbol{Q}\cdot\boldsymbol{R'}(0)]b_{\boldsymbol{R}}\exp[i\boldsymbol{Q}\cdot\boldsymbol{R}(t)] >_T . \tag{2.24}$$

In this formulation, scattering can be seen to arise from the interference between a wave scattered from a stationary center at $\boldsymbol{R'}$ and a related wave scattered from the moving center at $\boldsymbol{R}$ (see Figure 2-3).

Space-Time Representation

We perform Fourier transform over space and time and first we do this using (2.24)

$$\begin{aligned}\frac{d^2\sigma}{d\Omega dE'} &= \frac{k'}{k}\frac{1}{2\pi\hbar}\int_{-\infty}^{\infty} e^{-i\omega t}dt \sum_{\boldsymbol{R'},\,\boldsymbol{R}} < b_{\boldsymbol{R'}}b_{\boldsymbol{R}} >< \exp[-i\boldsymbol{Q}\cdot\boldsymbol{R'}(0)]\exp[i\boldsymbol{Q}\cdot\boldsymbol{R}(t)] >_T \\ &= \frac{k'}{k}\frac{1}{2\pi\hbar}\int_{-\infty}^{\infty} e^{-i\omega t}dt\Big\{< b_{\boldsymbol{R}} >^2 \sum_{\boldsymbol{R},\,\boldsymbol{R'}} < \exp[-i\boldsymbol{Q}\cdot\boldsymbol{R'}(0)]\exp[i\boldsymbol{Q}\cdot\boldsymbol{R}(t)] >_T \\ &\qquad +(< b_{\boldsymbol{R}}^2 > - < b_{\boldsymbol{R}} >^2)\sum_{\boldsymbol{R}} < \exp[-i\boldsymbol{Q}\cdot\boldsymbol{R}(0)]\exp[i\boldsymbol{Q}\cdot\boldsymbol{R}(t)] >_T\Big\} \qquad (2.25) \\ &\equiv N\frac{k'}{k}\frac{1}{2\pi\hbar}\int_{-\infty}^{\infty} e^{-i\omega t}dt\sum_{\boldsymbol{r}} e^{i\boldsymbol{Q}\cdot\boldsymbol{r}}\{< b_{\boldsymbol{R}} >^2 G(\boldsymbol{r},t) + (< {b_{\boldsymbol{R}}}^2 > - < b_{\boldsymbol{R}} >^2)G_s(\boldsymbol{r},t)\},\end{aligned}$$

where we used below definitions

$$N\sum_{\boldsymbol{r}} G(\boldsymbol{r},t)e^{i\boldsymbol{Q}\cdot\boldsymbol{r}} = \sum_{\boldsymbol{R},\,\boldsymbol{R'}} < \exp[-i\boldsymbol{Q}\cdot\boldsymbol{R'}(0)]\exp[i\boldsymbol{Q}\cdot\boldsymbol{R}(t)] >_T \qquad (2.26)$$

$$N\sum_{\boldsymbol{r}} G_s(\boldsymbol{r},t)e^{i\boldsymbol{Q}\cdot\boldsymbol{r}} = \sum_{\boldsymbol{R}} < \exp[-i\boldsymbol{Q}\cdot\boldsymbol{R}(0)]\exp[i\boldsymbol{Q}\cdot\boldsymbol{R}(t)] >_T \qquad (2.27)$$

N is the number of scattering nuclei. $G(\boldsymbol{r},t)$ and $G_s(\boldsymbol{r},t)$ are the Van Hove correlation functions [2]. We have separated cross-section into two parts: coherent scattering and incoherent scattering cross-sections.

$$\frac{d^2\sigma_{coh}}{d\Omega dE'} = N\frac{k'}{k}\frac{1}{2\pi\hbar}\int_{-\infty}^{\infty} e^{-i\omega t}dt\sum_{\boldsymbol{r}}\exp[i\boldsymbol{Q}\cdot\boldsymbol{r}] < b >^2 G(\boldsymbol{r},t) \qquad (2.28)$$

$$\frac{d^2\sigma_{incoh}}{d\Omega dE'} = N\frac{k'}{k}\frac{1}{2\pi\hbar}\int_{-\infty}^{\infty} e^{-i\omega t}dt\sum_{\boldsymbol{r}}\exp[i\boldsymbol{Q}\cdot\boldsymbol{r}](< b^2 > - < b >^2)G_s(\boldsymbol{r},t) \qquad (2.29)$$

The equations (2.26) and (2.27) are the quantum-mechanical expressions of Van Hove correlation functions and the functions can be given a simple physical interpretation in the classical limit. The operators $\boldsymbol{R'}(0)$ and $\boldsymbol{R}(t)$ commute and we have

$$G(\boldsymbol{r},t) = \frac{1}{N}\sum_{\boldsymbol{R},\,\boldsymbol{R'}}\delta(\boldsymbol{r}+\boldsymbol{R'}(0)-\boldsymbol{R}(t)) \qquad (2.30)$$

$$G_s(\boldsymbol{r},t) = \frac{1}{N}\sum_{\boldsymbol{R}}\delta(\boldsymbol{r}+\boldsymbol{R}(0)-\boldsymbol{R}(t)). \qquad (2.31)$$

$G(\boldsymbol{r},t)$ gives the probability that if there is an atom $\boldsymbol{R'}(0)$ at at time=0, there will be an atom at $\boldsymbol{R}(t)$ at time t. $G_s(\boldsymbol{r},t)$ gives the probability that if there is an atom at $\boldsymbol{R}(0)$ at time=0, the same atom will be an atom at $\boldsymbol{R}(t)$ at time t (in Figure 2-4).

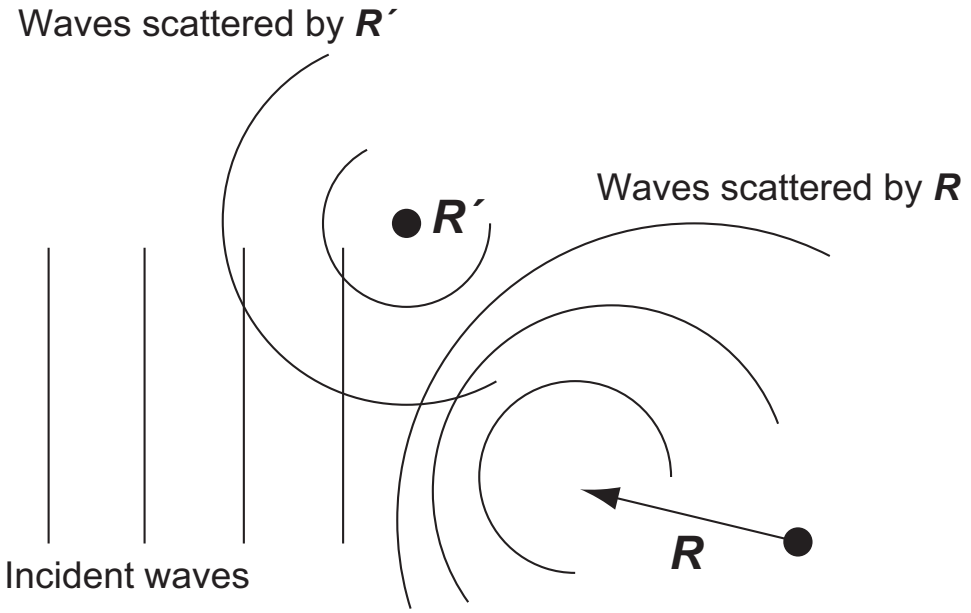

Figure 2.3: Interference between stationary centre $\boldsymbol{R}'$ and moving centre at $\boldsymbol{R}$.

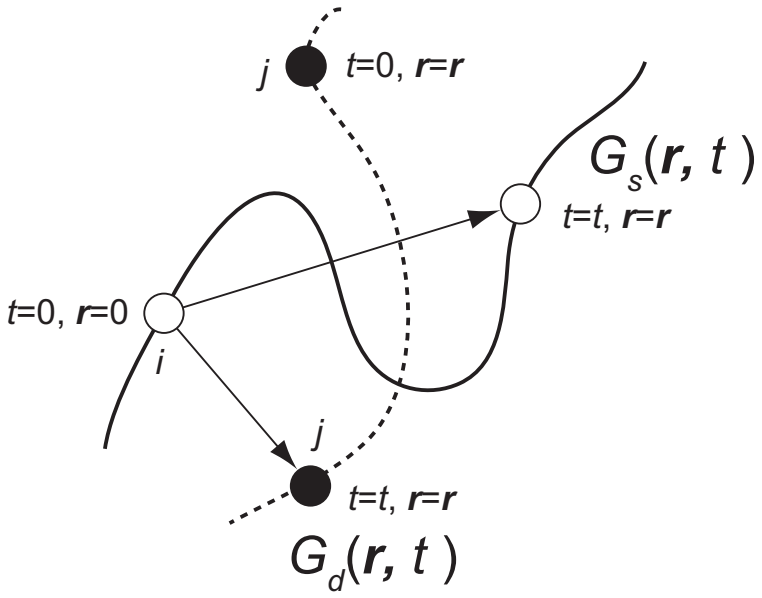

Figure 2.4: Schematic view of Van Hove correlation functions.

$$\frac{d^2\sigma_{coh}}{d\Omega dE'} = N\frac{k'}{k}\frac{< b >^2}{2\pi\hbar}\iint d\boldsymbol{r}\exp[i(\boldsymbol{Q}\cdot\boldsymbol{r}-\omega t)]G(\boldsymbol{r},t)dt \tag{2.32}$$

$$\frac{d^2\sigma_{incoh}}{d\Omega dE'} = N\frac{k'}{k}\frac{(< b^2 > - < b >^2)}{2\pi\hbar}\iint d\boldsymbol{r}\exp[i(\boldsymbol{Q}\cdot\boldsymbol{r}-\omega t)]G_s(\boldsymbol{r},t)dt. \tag{2.33}$$

(2.32) and (2.33) represent ($\boldsymbol{Q}$, ω) Fourier transform of the Van Hove correlation functions. Normally, we use the below equations.

$$S(\boldsymbol{Q},\omega) = \frac{1}{2\pi}\iint d\boldsymbol{r}\exp[i(\boldsymbol{Q}\cdot\boldsymbol{r}-\omega t)]G(\boldsymbol{r},t)dt \tag{2.34}$$

$$S_s(\boldsymbol{Q},\omega) = \frac{1}{2\pi}\iint d\boldsymbol{r}\exp[i(\boldsymbol{Q}\cdot\boldsymbol{r}-\omega t)]G_s(\boldsymbol{r},t)dt, \tag{2.35}$$

where scattering functions $S(\boldsymbol{Q},\omega)$ and $S_s(\boldsymbol{Q},\omega)$ are known as coherent and incoherent "scattering laws". The relations between the double differential cross-sections and the scattering laws are

$$\frac{d^2\sigma_{coh}}{d\Omega dE'} = N\frac{k'}{\hbar k} < b >^2 S(\boldsymbol{Q},\omega) \tag{2.36}$$

$$\frac{d^2\sigma_{incoh}}{d\Omega dE'} = N\frac{k'}{\hbar k}(< b^2 > - < b >^2)S_s(\boldsymbol{Q},\omega). \tag{2.37}$$

The space-time correlation functions represent basic dynamic properties of a scattering system, being independent of the properties of the scattered neutron, and the other scattering techniques can provide information about these functions. For example, X-ray scattering can tell us about $G(\boldsymbol{r},t)$ and infra-red spectroscopy about $G_s(\boldsymbol{r},t)$. Van Hove correlation function is a complex function of t, it is unsymmetrical function of ω after the Fourier transformation. The eigenfunction formulation tells us that the scattering laws for energy-loss (ω>0) and energy gain (ω<0) are related by

$$S(\boldsymbol{Q},\omega) = S(\boldsymbol{Q},-\omega)\exp(\hbar\omega/k_BT), \tag{2.38}$$

a property of $S(\boldsymbol{Q},\omega)$ which is frequently known as "detailed balance condition". In the classical limit ($\hbar \to 0$), $S(\boldsymbol{Q},\omega)$ is a symmetrical function and $G(\boldsymbol{r},t)$is a real quantity. $S_0(\boldsymbol{Q},\omega)$) is the value that was calculated from classical model and given by

$$S_0(\boldsymbol{Q},\omega) = \frac{1}{2}[S(\boldsymbol{Q},\omega) + S(\boldsymbol{Q},-\omega)] \tag{2.39}$$

Using (2.38), we can obtain the below equation

$$S_0(\boldsymbol{Q},\omega) = \frac{1}{2}S(\boldsymbol{Q},\omega)[1+\exp(-\hbar\omega/k_BT)]. \tag{2.40}$$

If scattering function is known from classical considerations, a detailed balance-corrected function is easily calculated.

Finally, we remark that in the analysis of neutron inelastic from liquids, the correlation function $G_d(\boldsymbol{r},t)$ is used. It is defined by

$$G(\boldsymbol{r},t) = G_s(\boldsymbol{r},t) + G_d(\boldsymbol{r},t) \tag{2.41}$$

and is called the distinct correlation function (see Figure 2-4).

Vibrational States of A Molecule

The δ function in the eigenstate formulation limits the neutron scattering to transition from an occupied state to another level since the sum over the initial and final states may be restricted to the single molecule. Unlike the infra-red or Raman scattering, there is no selection rule for neutron scattering, therefore it is easily understood by time-dependent formulation of the scattering cross-section. We assume that the displacement $\boldsymbol{R}(t)$ of the nth atom for a given vibrational mode of molecule is

$$\boldsymbol{R}(t) = \boldsymbol{n} + \boldsymbol{u_n}(t), \tag{2.42}$$

where $\boldsymbol{n}$ is the vector from the origin to the mean position of the atom and

$$\boldsymbol{u}(t) = \boldsymbol{u}_0\cos\omega_0 t = \boldsymbol{u}_0\frac{\exp(i\omega_0 t)+\exp(-i\omega_0 t)}{2}. \tag{2.43}$$

u_0 is the amplitude of the vibration and ω_0 its characteristic frequency. Substituting in (2.24), we have

$$\frac{d^2\sigma}{d\Omega dE'} = \frac{k'}{k}\frac{1}{2\pi\hbar}\int_{-\infty}^{\infty} e^{-i\omega t}dt \sum_{n,\,m} < b_n b_m > \exp[i\boldsymbol{Q}\cdot(\boldsymbol{n}-\boldsymbol{m})] \times < \exp[i\boldsymbol{Q}\cdot(\boldsymbol{u_n}(t)-\boldsymbol{u_m}(0))] >_T . \tag{2.44}$$

Assuming that u_0 is smaller than λ, (2.43) may be expanded in $\boldsymbol{u}$ as follows.

$$\begin{aligned} < \exp[i\boldsymbol{Q}\cdot(\boldsymbol{u_n}(t)-\boldsymbol{u_m}(0))] >_T =& < 1 + i\boldsymbol{Q}\cdot(\boldsymbol{u_n}(t)-\boldsymbol{u_m}(0)) \\ &+\frac{i^2}{2}[\boldsymbol{Q}\cdot(\boldsymbol{u_n}(t)-\boldsymbol{u_m}(0))]^2+\ldots >_T \\ =& < 1-\frac{1}{2}((\boldsymbol{Q}\cdot\boldsymbol{u_n}(t))^2+(\boldsymbol{Q}\cdot\boldsymbol{u_m}(0))^2) \\ +(\boldsymbol{Q}\cdot\boldsymbol{u_0})^2\frac{\exp(i\omega_0 t)+\exp(-i\omega_0 t)}{2} &+\ldots+\text{imaginary terms} >_T . \end{aligned} \tag{2.45}$$

Ignoring the imaginary terms, the time integration in (2.43) can be given by

$$\begin{aligned} \frac{d^2\sigma}{d\Omega dE'} = \frac{k'}{k}\frac{1}{2\pi\hbar}\sum_{n,\,m} < b_n b_m > \exp[i\boldsymbol{Q}\cdot(\boldsymbol{n}-\boldsymbol{m})]\times \\ \Big[\Big(1-\frac{1}{2}<(\boldsymbol{Q}\cdot\boldsymbol{u_n})^2>-\frac{1}{2}<(\boldsymbol{Q}\cdot\boldsymbol{u_m})^2>\Big)\delta(\hbar\omega)+\frac{1}{2}(\boldsymbol{Q}\cdot\boldsymbol{u_0})^2\delta(\hbar\omega-\hbar\omega_0) \\ +\frac{1}{2}(\boldsymbol{Q}\cdot\boldsymbol{u_0})^2\delta(\hbar\omega+\hbar\omega_0)+\ldots\Big]. \end{aligned} \tag{2.46}$$

By considering the real terms only, we have obtained (2.45) which is valid for classical limit, however it indicates some important points.

(1) The cross-section includes both elastic term and inelastic term.

(2) The inelastic terms contain a polarization factor $(\boldsymbol{Q}\cdot\boldsymbol{u_0})^2$, showing that inelastic scattering is a maximum for the scattering vector $\boldsymbol{Q}$ parallel to the polarization direction $\boldsymbol{u_0}$ and is 0 for $\boldsymbol{Q}$ at the right angles to $\boldsymbol{u_0}$.

(3) The vibrational intensities, for a fixed angle between $\boldsymbol{u_0}$ and $\boldsymbol{Q}$, are proportional to $Q^2 = 16\pi^2\sin 2\theta/\lambda^2$.

(4) Both elastic and inelastic contributions to the cross-section are attenuated by Debye-Waller factor (DWF). The contents of curly bracket in (2.45) represent the leading term of the exponential expression for DWF.

(5) The inelastic cross-section contains both coherent and incoherent scattering components. This can be clearly seen by considering the one-phonon terms in (2.45).

$$\begin{aligned}\frac{d^2\sigma^1}{d\Omega dE'} &= \frac{k'}{k}\frac{1}{2\pi\hbar}\sum_{n,\,m} < b_n b_m > \exp[i\boldsymbol{Q}\cdot(\boldsymbol{n}-\boldsymbol{m})]\times \\ &\qquad \frac{1}{2}(\boldsymbol{Q}\cdot\boldsymbol{u_0})^2(\delta(\hbar\omega+\hbar\omega_0)+\delta(\hbar\omega-\hbar\omega_0)) \\ &= \frac{k'}{k}\sum_{n,\,m} < b >^2 \exp[i\boldsymbol{Q}\cdot(\boldsymbol{n}-\boldsymbol{m})]\times\frac{1}{2}(\boldsymbol{Q}\cdot\boldsymbol{u_0})^2(\delta(\hbar\omega+\hbar\omega_0)+\delta(\hbar\omega-\hbar\omega_0)) \\ &\qquad +\frac{k'}{k}(< b^2 > - < b >^2)N\frac{1}{2}(\boldsymbol{Q}\cdot\boldsymbol{u_0})^2(\delta(\hbar\omega+\hbar\omega_0)+\delta(\hbar\omega-\hbar\omega_0)),\end{aligned} \tag{2.47}$$

where σ^1 indicates the one-phonon contribution to the cross-section. The first term is the one-phonon coherent scattering cross-section and the second term is the incoherent scattering cross-section.

Coherent Scattering from Phonons

Using the polarization vector $\boldsymbol{U_\rho^j}(\boldsymbol{q})$, the coherent one-phonon cross-section is given by

$$\begin{aligned}\frac{d^2\sigma^1_{coh}}{d\Omega dE'} &= \frac{(2\pi)^3}{v}\sum_{\boldsymbol{q},\,\boldsymbol{j}}\frac{k'}{k}\delta(\hbar\omega-\hbar\omega_{\boldsymbol{j}}(\boldsymbol{q}))\times\sum_{\boldsymbol{\tau}}\delta(\boldsymbol{Q}\mp\boldsymbol{q}-\boldsymbol{\tau}) \\ &\qquad \times\frac{\hbar(n_s+\frac{1}{2}\pm\frac{1}{2})}{2\omega_{\boldsymbol{j}}(\boldsymbol{q})} \\ &\qquad \times\Big|\sum_{\boldsymbol{\rho}}\frac{< b >_\rho}{M_\rho}\exp(i\boldsymbol{Q}\cdot\boldsymbol{\rho})\boldsymbol{Q}\cdot\boldsymbol{U_\rho^j}(\boldsymbol{q})e^{-w_\rho}\Big|^2.\end{aligned} \tag{2.48}$$

$\omega_{\boldsymbol{j}}(\boldsymbol{q})$ is the characteristic frequency of mode $\boldsymbol{j}$, $\boldsymbol{q}$, and $\boldsymbol{\tau}$ is the reciprocal lattice vector. $< b >_{\boldsymbol{\rho}}$ is the coherent scattering length of atom at $\boldsymbol{\rho}$ in the unit cell, $M_{\boldsymbol{\rho}}$ is its mass and $e^{-w_{\boldsymbol{\rho}}}$ is the Debye-Waller factor. The upper signs in the middle term refer to the neutron energy loss or phonon creation and the lower signs to the neutron energy gain or phonon annihilation. All the phonon modes are harmonic oscillators, therefore the population is described by the Bose-Einstein population factor (n_s or n_s +1), where n_s is given by

$$n_s = \frac{1}{[\exp(\hbar\omega_{\boldsymbol{j}}(\boldsymbol{q})/k_BT)-1]}. \tag{2.49}$$

There exist two delta functions in (2.47) and one represent the conservation on energy and another is the conservation of momentum and the existence of two delta functions

means the scattering occurs under special conditions. The last term of (2.47) is not so important because it only affects the intensity of phonon peaks and not their energy. However, it can provide a means of distinguishing the various modes in a complex phonon spectrum.

Incoherent Scattering from Phonons

The incoherent scattering offers less information than coherent scattering because of absence of momentum δ function. It also means that the relative orientation of $\boldsymbol{Q}$ and of the reciprocal lattice vector $\boldsymbol{\tau}$ is of little importance. The differential scattering cross-section for single-phonon process is given by

$$\frac{d^2\sigma^1_{incoh}}{d\Omega dE'} = \sum_{\boldsymbol{q},j} \frac{k'}{k}\delta(\hbar\omega \mp \hbar\omega_j(\boldsymbol{q})) \times \frac{\hbar(n_s + \frac{1}{2} \pm \frac{1}{2})}{2\omega_j(\boldsymbol{q})} \times \sum_{\boldsymbol{\rho}} \frac{(< b^2 >_\rho - < b >^2_\rho)}{M_\rho}\left|\boldsymbol{Q}\cdot\boldsymbol{U}^j_{\boldsymbol{\rho}}(\boldsymbol{q})\right|^2 e^{-2w_\rho}. \tag{2.50}$$

In this formulation, mode polarization term $|\boldsymbol{Q}\cdot\boldsymbol{U}|^2$ has lost its structure factor coefficient so that the intensity of a mode is proportional to the square of the vibrational amplitude of each atom in the mode and to the $4\pi(< b^2 >_\rho - < b >^2_\rho)$. Assuming that $< (\boldsymbol{Q}\cdot\boldsymbol{U})^2 >= \frac{1}{3}Q^2 < u^2 >$, (2.49) can be given by

$$\frac{d^2\sigma^1_{incoh}}{d\Omega dE'} = \frac{\hbar k'}{k}(< b^2 > - < b >^2)\frac{Q^2 < u^2 >}{6M}(n_s + \frac{1}{2} \pm \frac{1}{2})e^{-2w}\sum_{\boldsymbol{q},j}\frac{\delta(\hbar\omega \mp \hbar\omega_j(\boldsymbol{q}))}{\omega_j(\boldsymbol{q})} \tag{2.51}$$

Summation over $\boldsymbol{q}$ can be transformed to an integration over the density of phonon states $G(\omega)$:

$$\sum_{\boldsymbol{q},j}\frac{\delta(\hbar\omega \mp \hbar\omega_j(\boldsymbol{q}))}{\omega_j(\boldsymbol{q})} = \frac{1}{\hbar}\sum_{\boldsymbol{q},j}\frac{\delta(\omega \mp \omega_j(\boldsymbol{q}))}{\omega_j(\boldsymbol{q})} = \frac{3N}{\hbar}\frac{G(\omega)}{\omega}. \tag{2.52}$$

$3N$ is the total number of phonon states and $G(\omega)$ is normalized density $\int_0^\infty G(\omega)d\omega = 1$. Therefore the cross-section formula reduces to

$$\frac{d^2\sigma^1_{incoh}}{d\Omega dE'} = \frac{k'}{k}(< b^2 > - < b >^2)\frac{Q^2 < u^2 >}{2M}(n_s + \frac{1}{2} \pm \frac{1}{2})e^{-2w}N\frac{G(\omega)}{\omega}. \tag{2.53}$$

From the simple experimental measurements on a powder sample, we obtain phonon spectrum. In the case of hydrogenous materials, the observed inelastic scattering is

proportional to density of states of each mode multiplied by the mean square vibrational amplitude of the hydrogen atoms in that mode due to the strong incoherent scattering from hydrogen.

2.1.3 Quasielastic Scattering from Some Models

As described in the former section, inelastic scattering is used for investigating the vibrational modes under the conservation of energy, however quasielastic scattering is used for investigating relaxational process that was caused by random motions or energy dissipation. Basically the observable in quasielastic scattering is differential cross-section $\frac{d^2\sigma^1}{d\Omega dE'}$ that was the same for inelastic scattering, however $S(\boldsymbol{Q},\ \omega)$ is mainly used for discussion or analysis. We have already described the detail of $S(\boldsymbol{Q},\ \omega)$ in section (1.3.2), using Van Hove correlation functions, therefore we introduce some models in quasielastic scattering in this section and more detailed models and equations are referred to a book [3].

Simple Diffusion

In a liquid, in the presence of a macroscopic gradient of concentration, a flux of atoms occur, taking a direction in order to reduce the concentration gradient, and proportional to it: the constant of proportionality is denoted D. The concentration fluctuations in a volume element $d\boldsymbol{r}$ at $\boldsymbol{r}$ is given by $D\nabla^2 G_s(\boldsymbol{r},t)$ and is equal to the time rate of change of concentration

$$D\nabla^2 G_s(\boldsymbol{r},t) = \frac{\partial}{\partial t} G_s(\boldsymbol{r},t), \tag{2.54}$$

where D is a macroscopic diffusion constant. This equation is well-known Fick's law and using an initial condition $G_s(\boldsymbol{r},0) = \delta(\boldsymbol{r})$ and $\int G_s(\boldsymbol{r},t)d\boldsymbol{r} = 1$, we can solve easily and obtain with the below equation

$$G_s(\boldsymbol{r},t) = (4\pi Dt)^{-3/2} \exp\Big(-\frac{r^2}{4Dt}\Big) \tag{2.55}$$

$$< r^2 >= \int |\boldsymbol{r}|^2 G_s(\boldsymbol{r},t)d\boldsymbol{r} = 6Dt. \tag{2.56}$$

Fourier transform in ($\boldsymbol{Q}$, ω) space lead to the intermediate scattering function $I_s(\boldsymbol{Q}, t)$

$$I_s(\boldsymbol{Q}, t) = \int G_s(\boldsymbol{r}, t) \exp(-i\boldsymbol{Q} \cdot \boldsymbol{r}) d\boldsymbol{r} = \exp(-DQ^2 t) \tag{2.57}$$

$$S_s(\boldsymbol{Q}, \omega) = \frac{1}{\pi} \cdot \frac{DQ^2}{\omega^2 + (DQ^2)^2}. \tag{2.58}$$

Energy spectrum exhibits Lorentzian type function and we can evaluate D from the Q dependence of half-width at half-maximum Γ ($=DQ^2$), as shown in Figure 2-5.

Jump Diffusion Model

With the simple diffusion model, the behaviour of diffusion of liquid cannot be well described at high Q region, therefore other theoretical model was designed by Singwi and Sjölander in order to describe the liquid water. In this theory, a molecule executes an oscillatory motion for a mean time τ_0, as shown in Figure 2-6. Then it diffuses by continuous motion for a mean time τ_1. The sort of motion is continuously repeated. To calculate $G_s(\boldsymbol{r}, t)$, they divide the motion into steps numbered 0,1,$\cdots$.$2N$. At t=0, the particle is assumed to be oscillate about the origin $\boldsymbol{r}$=0. At later time t, it could have arrived at $\boldsymbol{r}$ after making 0,1,$\cdots$.$2N$ steps. 0 step corresponds to the oscillatory motion, step 1 to succeeding diffusive motion, step 2 again to oscillatory motion , step 3 to diffusive motion. $G_s(\boldsymbol{r}, t)$ is given by the expansion into probabilities related to the different processes

$$G_s(\boldsymbol{r}, t) = \sum_{i=0}^{\infty} F_i(\boldsymbol{r}, t). \tag{2.59}$$

The successive $F_i(\boldsymbol{r}, t)$. are evaluated as follows. One gets for step 0

$$F_0(\boldsymbol{r}, t) = g(\boldsymbol{r}, t) \cdot p(t), \tag{2.60}$$

where $g(\boldsymbol{r}, t)$ is the probability for finding a particle at $(\boldsymbol{r}, t)$ and $p(t)$ is the probability that particle remains in the same oscillatory motion at t. Singwi and Sjölander assumed for $p(t)$ the simple form

$$p(t) = \exp(-t/\tau_0), \tag{2.61}$$

where τ_0 is the lifetime of the oscillatory motion and is much larger than the period of oscillatory motion. The motion of molecule is similar to the solid state, therefore

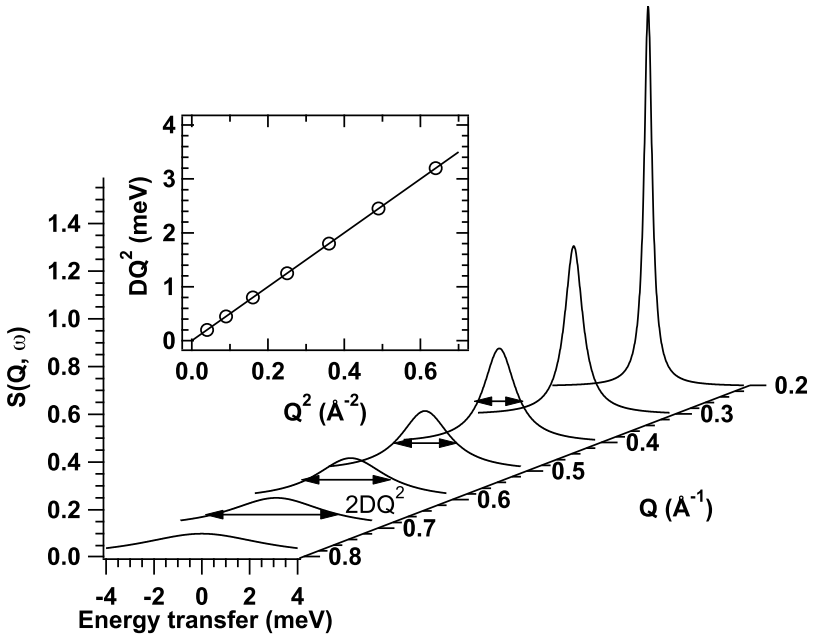

Figure 2.5: Scattering law corresponding to a simple diffusion model.

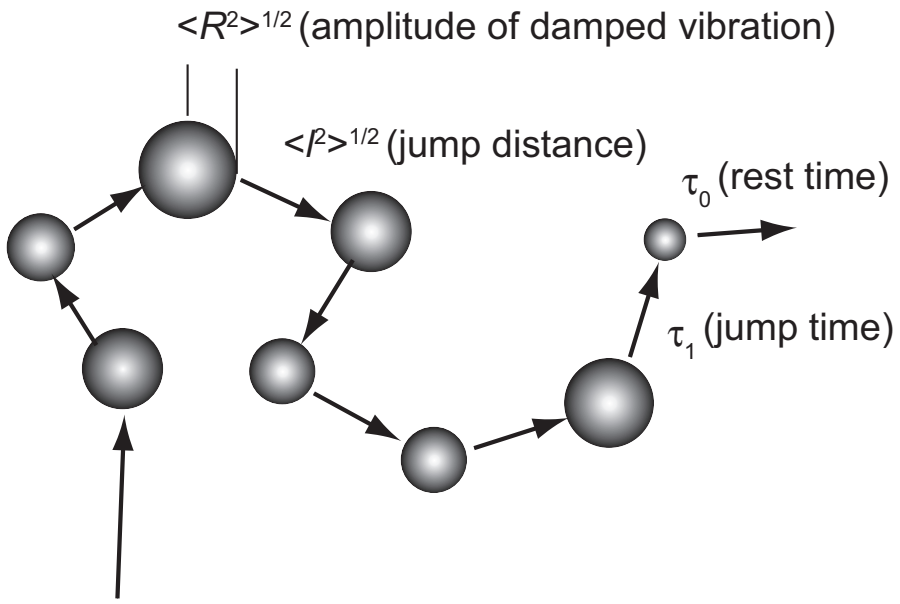

Figure 2.6: Schematic view of a jump simple diffusion model.

$g(\boldsymbol{r},t)$ is chosen based on Debye description. The obtained $g(\boldsymbol{r},t)$ is given by

$$g(\boldsymbol{r},t) = [2\pi\gamma(t)]^{-3/2}\exp\Big(-\frac{r^2}{2\gamma(t)}\Big), \tag{2.62}$$

where $\gamma(t)$ is the oscillatory width

$$\gamma(t) = \gamma_\infty\Big(1-\frac{\sin\omega_D t}{\omega_D t}\Big), \tag{2.63}$$

where ω_D is the characteristic for a harmonic Debye crystal and

$$\gamma_\infty = \frac{3k_BT}{M{\omega_D}^2} \tag{2.64}$$

is mean square amplitude for vibrating atom. The probability for step 1 is given by

$$F_1(\boldsymbol{r},t) = -\int_0^t dt_1\int d\boldsymbol{r_1}q(t-t_1)h(\boldsymbol{r}-\boldsymbol{r_1},t-t_1)p'(t_1)\cdot g(\boldsymbol{r_1},t_1). \tag{2.65}$$

$h(\boldsymbol{r},t)$ is the probability of finding a molecule at $(\boldsymbol{r},t)$, when it is performing a diffusive motion between two equilibrium positions and $h(\boldsymbol{r},t)$is the solution of (2.53).

$$h(\boldsymbol{r},t) = (4\pi D_1 t)^{-3/2}\exp\Big(-\frac{r^2}{4D_1t}\Big) \tag{2.66}$$

D_1 is defined to $D_1 =< l^2 > /6\tau_1$, where $< l^2 >$ is mean square displacement (MSD) in τ_1 during continuous diffusion take place and $q(t)$ gives the probability that particle remains in the same state of diffusive motion at t. It is assumed to have the same form as $p(t)$.

$$q(t) = \exp(-t/\tau_1) \tag{2.67}$$

The probability that the particle has its oscillatory state between t and $t+dt$ is given by

$$p'(t)dt = p(t+dt)-p(t). \tag{2.68}$$

Step 2 is given by

$$F_2(\boldsymbol{r},t) = (-1)^2\int_0^t dt_2\int_0^{t_2} dt_1\int d\boldsymbol{r_2}\int d\boldsymbol{r_1}p(t-t_2)g(|\boldsymbol{r}-\boldsymbol{r_2}|,t-t_2)q'(t_2-t_1)$$
$$\times h(|\boldsymbol{r_2}-\boldsymbol{r_1}|,t_2-t_1)p'(t_1)\cdot g(\boldsymbol{r_1},t_1) \tag{2.69}$$

$$q'(t)dt = q(t+dt)-q(t) \tag{2.70}$$

In a general way, for step $2N$, we have

$$F_{2N}(\boldsymbol{r},t) = (-1)^2 N \int_0^t dt_{2N} \int_0^{t_{2N}} dt_{2N-1} \ldots \int_0^{t_2} dt_1 \int d\boldsymbol{r_{2N}} \int d\boldsymbol{r_{2N-1}} \ldots \int d\boldsymbol{r_1}$$
$$p(t_2 - t_{2N}) g(|\boldsymbol{r} - \boldsymbol{r_{2N}}|, t - t_{2N}) q'(t_{2N} - t_{2N-1}) h(|\boldsymbol{r_{2N}} - \boldsymbol{r_{2N-1}}|, t_{2N} - t_{2N-1})$$
$$\ldots p'(t_1) \cdot g(\boldsymbol{r_1}, t_1) \quad (2.71)$$

By substituting F_i in (2.58), we can obtain $G_s(\boldsymbol{r},t)$ and $S(\boldsymbol{Q},\omega)$. After making following changes of variables

$$t - t_{2N} = \tau_{2N+1}, t_{2N} - t_{2N-1} = \tau_{2N}, \ldots\ldots t_2 - t_1 = \tau_2, t_1 = \tau_1 \quad (2.72)$$

we can obtain four terms

$$A = \int_0^\infty dt \int d\boldsymbol{r} \exp[i(\boldsymbol{Q}\cdot\boldsymbol{r} - \omega t)] p(t) \cdot g(\boldsymbol{r},t) = \exp\Big(-\frac{1}{2}Q^2\gamma_\infty\Big) \frac{\tau_0}{1 + i\omega\tau_0} \quad (2.73)$$

$$B = \int_0^\infty dt \int d\boldsymbol{r} \exp[i(\boldsymbol{Q}\cdot\boldsymbol{r} - \omega t)] q(t) \cdot h(\boldsymbol{r},t) = \frac{\tau_1}{1 + Q^2 D_1 \tau_1 + i\omega\tau_1} \quad (2.74)$$

$$C = -\int_0^\infty dt \int d\boldsymbol{r} \exp[i(\boldsymbol{Q}\cdot\boldsymbol{r} - \omega t)] p'(t) \cdot g(\boldsymbol{r},t) = A/\tau_0 \quad (2.75)$$

$$D = -\int_0^\infty dt \int d\boldsymbol{r} \exp[i(\boldsymbol{Q}\cdot\boldsymbol{r} - \omega t)] q'(t) \cdot h(\boldsymbol{r},t) = B/\tau_1. \quad (2.76)$$

We can write using the above equations

$$\int_0^\infty dt \int d\boldsymbol{r} \exp[i(\boldsymbol{Q}\cdot\boldsymbol{r} - \omega t)] F_{2N}(\boldsymbol{r},t) = AC^N D^N \quad (2.77)$$

$$\int_0^\infty dt \int d\boldsymbol{r} \exp[i(\boldsymbol{Q}\cdot\boldsymbol{r} - \omega t)] F_{2N+1}(\boldsymbol{r},t) = BC^{N+1} D^N. \quad (2.78)$$

Hence the time space Fourier transform of $G_s(\boldsymbol{r},t)$ is given by

$$\int_0^\infty dt \int d\boldsymbol{r} \exp[i(\boldsymbol{Q}\cdot\boldsymbol{r} - \omega t)] \sum_{N=0}^\infty F_N(\boldsymbol{r},t) = \frac{A + BC}{1 - CD} + \ldots. \quad (2.79)$$

The above expression was derived under the assumption that at t=0, all the particles start with an oscillatory motion. The same treatment has to be applied, with particles starting their motion as free diffusing particles.

$$\int_0^\infty dt \int d\boldsymbol{r} \exp[i(\boldsymbol{Q}\cdot\boldsymbol{r} - \omega t)] \sum_{N=0}^\infty F_N(\boldsymbol{r},t) = \frac{B + AD}{1 - CD} + \ldots. \quad (2.80)$$

By taking account the fractions of particles performing an oscillatory or diffusive motion

$$S(\boldsymbol{Q},\omega)=\frac{1}{2\pi}\left[\frac{\tau_0}{\tau_1+\tau_0}\frac{A[1+B{\tau_0}^{-1}]}{1-\frac{AB}{\tau_0\tau_1}}+\frac{\tau_1}{\tau_1+\tau_0}\frac{B[1+A{\tau_1}^{-1}]}{1-\frac{AB}{\tau_0\tau_1}}\right]. \tag{2.81}$$

Substituting into (2.80) the expression of DWF in a solid

$$2W=\frac{1}{2}Q^2<u^2>=\frac{1}{2}Q^2\gamma_\infty \tag{2.82}$$

with (2.72)-(2.75), we can obtain

$$S(\boldsymbol{Q},\omega)=\frac{1}{\pi}\frac{\exp(-2W)\tau_0}{1+\frac{\tau_1}{\tau_0}}\frac{(c+d\omega^2{\tau_0}^2)b}{b^2+\omega^2{\tau_0}^2(f+\omega^2{\tau_0}^2g)} \tag{2.83}$$

where

$$\begin{aligned} b &= 1+Q^2D_1\tau_1-\exp(-2W) && (2.84)\\ c &= 1+Q^2D_1\tau_1+2\frac{\tau_1}{\tau_0}+\left(\frac{\tau_1}{\tau_0}\right)^2\exp(-2W) && (2.85)\\ d &= \left(\frac{\tau_1}{\tau_0}\right)^2 2W && (2.86)\\ f &= (1+Q^2D_1\tau_1)^2+\left(\frac{\tau_1}{\tau_0}\right)^2+2\frac{\tau_1}{\tau_0}\exp(-2W) && (2.87)\\ g &= \left(\frac{\tau_1}{\tau_0}\right)^2. && (2.88) \end{aligned}$$

if $<\overline{R}^2>$is mean square radius of the thermal cloud developed in the oscillatory motion, the actual diffusion constant D, taking into account both diffusive and oscillatory states, is given by

$$D=\frac{<R^2>+<l^2>}{6(\tau_0+\tau_1)} \tag{2.89}$$

and differs from D_1. Because radius of the thermal cloud is assumed to be small compared with the mean length of continuous diffusion.

$$D_1\tau_1\simeq=D\tau_0\Big(1+\frac{\tau_1}{\tau_0}\Big).(\text{where } <R^2>\ll<l^2>). \tag{2.90}$$

We also consider the limiting case when τ_1 is much larger than τ_0. (2.82) reduces to

$$S(\boldsymbol{Q},\omega)=\frac{1}{\pi}\cdot\frac{DQ^2}{\omega^2+(DQ^2)^2}. \tag{2.91}$$

When τ_0 is much larger than n τ_1. (2.82) reduces to

$$S(\boldsymbol{Q},\omega)=\exp(-2W)\cdot\frac{\tau_0}{\pi}\frac{1-\frac{\exp(-2W)}{1+D\tau_0Q^2}}{\omega^2{\tau_0}^2+\left[1-\frac{\exp(-2W)}{1+D\tau_0Q^2}\right]} \tag{2.92}$$

$$\Gamma = \frac{1}{\tau_0} \cdot \Big[1 - \frac{\exp(-2W)}{1 + D\tau_0 Q^2}\Big] (2W = \frac{1}{2}Q^2 < R^2 >). \tag{2.93}$$

In the low Q limit, $\Gamma = DQ^2$, which is similar to the simple diffusion.
In the high Q limit $\Gamma = \frac{1}{\tau_0}$, which is independent on Q.

Jump Model among Two Sites

In real systems, random motions are often limited in a finite space. Hence we indicate jump motions between two sites as one example of restricted diffusion motion in this section. We consider the case that the finding probability of particle is described by $p(\boldsymbol{r_1}, t)$ and $p(\boldsymbol{r_2}, t)$ at time t, $\boldsymbol{r_1}, \boldsymbol{r_2}$. Then we can design a set of equations.

$$\frac{d}{dt}p(\boldsymbol{r_1}, t) = -\frac{1}{\tau}p(\boldsymbol{r_1}, t) + \frac{1}{\tau}p(\boldsymbol{r_2}, t) \tag{2.94}$$

$$\frac{d}{dt}p(\boldsymbol{r_2}, t) = \frac{1}{\tau}p(\boldsymbol{r_1}, t) - \frac{1}{\tau}p(\boldsymbol{r_2}, t), \tag{2.95}$$

where τ^{-1} is jump rate probability from one site to the other site with equal probability. We immediately get

$$\frac{d}{dt}[p(\boldsymbol{r_1}, t) + p(\boldsymbol{r_2}, t)] = 0 \tag{2.96}$$

$$p(\boldsymbol{r_1}, t) + p(\boldsymbol{r_2}, t) = 1. \tag{2.97}$$

The solutions for $p(\boldsymbol{r_1}, t)$ and $p(\boldsymbol{r_2}, t)$ are of the form:

$$p(\boldsymbol{r_1}, t) = A + Be^{-2t/\tau}, p(\boldsymbol{r_2}, t) = A - Be^{-2t/\tau} \tag{2.98}$$

where A and B are determined from initial conditions. Assuming that the particle was initially at $\boldsymbol{r_1}$ at t=0

$$p(\boldsymbol{r_1}, 0) = A + B = 1, p(\boldsymbol{r_2}, 0) = A - B = 0 \tag{2.99}$$

we obtain

$$p(\boldsymbol{r_1}, t; \boldsymbol{r_1}, 0) = \frac{1}{2}[1 + \exp(-2t/\tau)], p(\boldsymbol{r_2}, t; \boldsymbol{r_1}, 0) = \frac{1}{2}[1 - \exp(-2t/\tau)] \tag{2.100}$$

where $p(\boldsymbol{r_i}, t; \boldsymbol{r_j}, 0)$ denotes the probability that the proton is at $\boldsymbol{r_i}$ at time t, under the condition that it was at $\boldsymbol{r_j}$, t=0. And we can obtain for the case of a proton at $\boldsymbol{r_2}$ at time t=0.

$$p(\boldsymbol{r_1}, t; \boldsymbol{r_2}, 0) = \frac{1}{2}[1 - \exp(-2t/\tau)], p(\boldsymbol{r_2}, t; \boldsymbol{r_2}, 0) = \frac{1}{2}[1 + \exp(-2t/\tau)] \tag{2.101}$$

The equilibrium distribution is obtained by taking $t \to \infty$

$$p(\boldsymbol{r_1}, \infty) = p(\boldsymbol{r_2}, \infty) = \frac{1}{2} \tag{2.102}$$

The intermediate scattering function can be evaluated

$$\begin{aligned} I(\boldsymbol{Q}, t) =< e^{i\boldsymbol{Q}\cdot\boldsymbol{r}(t)} e^{-i\boldsymbol{Q}\cdot\boldsymbol{r}(0)} >= [p(\boldsymbol{r_1}, t; \boldsymbol{r_1}, 0) + p(\boldsymbol{r_2}, t; \boldsymbol{r_1}, 0) e^{i\boldsymbol{Q}\cdot(\boldsymbol{r_2} - \boldsymbol{r_1})}] p(\boldsymbol{r_1}, 0) \\ + [p(\boldsymbol{r_1}, t; \boldsymbol{r_2}, 0) e^{i\boldsymbol{Q}\cdot(\boldsymbol{r_1} - \boldsymbol{r_2})} + p(\boldsymbol{r_2}, t; \boldsymbol{r_2}, 0)] p(\boldsymbol{r_2}, 0). \end{aligned} \tag{2.103}$$

Assuming that the system was in equilibrium at t=0

$$p(\boldsymbol{r_1}, 0) = p(\boldsymbol{r_2}, 0) = \frac{1}{2}. \tag{2.104}$$

we obtain

$$I(\boldsymbol{Q}, t) = A_0(\boldsymbol{Q}) + A_1(\boldsymbol{Q}) \exp(-2t/\tau), \tag{2.105}$$

where

$$A_0(\boldsymbol{Q}) = [1 + \cos \boldsymbol{Q} \cdot (\boldsymbol{r_2} - \boldsymbol{r_1})]/2, A_1(\boldsymbol{Q}) = [1 - \cos \boldsymbol{Q} \cdot (\boldsymbol{r_2} - \boldsymbol{r_1})]/2. \tag{2.106}$$

After the Fourier transformation with respect to t, we finally obtain

$$S(\boldsymbol{Q}, \omega) = A_0(\boldsymbol{Q}) \delta(\omega) + A_1(\boldsymbol{Q}) \frac{1}{\pi} \frac{2\tau}{4 + \omega^2 \tau^2}. \tag{2.107}$$

In the case of a powder sample, we obtain

$$S(Q, \omega) = A_0(Q) \delta(\omega) + A_1(Q) \frac{1}{\pi} \frac{2\tau}{4 + \omega^2 \tau^2} \tag{2.108}$$

$$A_0(Q) = \frac{1}{2}[1 + j_0(Qd)], A_1(Q) = \frac{1}{2}[1 - j_0(Qd)], \tag{2.109}$$

where $j_0(x)$ is a spherical Bessel function of the 0th order and d is the jump distance.

2.2 Instrumentation

2.2.1 Principle of Time-of-Flight (TOF) Spectrometer

We used three time-of-flight (TOF) spectrometers, LAM-40 installed at KENS spallation cold source in High Energy Accelerator Research Organization (KEK) in

Tsukuba, OSIRIS and MARI installed at a pulsed neutron source in ISIS, Rutherford Appleton Laboratory, Didcot for inelastic and quasielastic scattering measurements. In this section, we would like to describe briefly the principle of TOF spectrometer at a pulse neutron source. TOF spectrometers are divided into two classes [4]. One is direct geometry spectrometers and the other is inverted geometry spectrometers.

Direct geometry spectrometers: in which E_1 is defined by a device such as a crystal or a chopper, and the final energy E_2 is determined by TOF and very simplified schematic view of this type of spectrometer is shown in Figure 2-7(a). In this spectrometer, the incident beam is monochromated using a Fermi chopper. A background chopper like disc chopper is effectively designed to prevent a large flux of epithermal neutrons entering the spectrometer where they will be thermalized and produce background signal. In all cases detector arrays tend to be as large as physically possible to maximize the efficiency of the spectrometer. In this thesis, MARI is this kind of spectrometer.

Inverted geometry spectrometers: in which the sample is illuminated by a white incident neutron and E_2 is defined by a crystal or a filter and E_1 is determined by TOF. A very simplified schematic view of spectrometer is shown in Figure 2-7(b). The inverted geometry spectrometers offer access to a wide energy range in neutron energy loss side. Many kinds of inverted geometry spectrometers with various designs have been constructed to provide various performances: crystal analyzer spectrometers like TOSCA at ISIS providing a wide energy window, backscattering spectrometers like IRIS at ISIS which give a very high energy resolution and coherent excitation spectrometers like PRISMA at ISIS to see dispersion relationship in the excitation. In this thesis, LAM-40 and OSIRIS are this kind of spectrometer.

Before going to describing the detail of each spectrometer, we simply explain the principle of TOF spectrometer, taking an inverted geometry TOF spectrometer as an example. The time when the neutron emitted from moderator is set to t=0 and the distance from the moderator to the sample is defined as L_1 (first flight path) and the distance from the sample to the energy analyzer and the distance from the energy

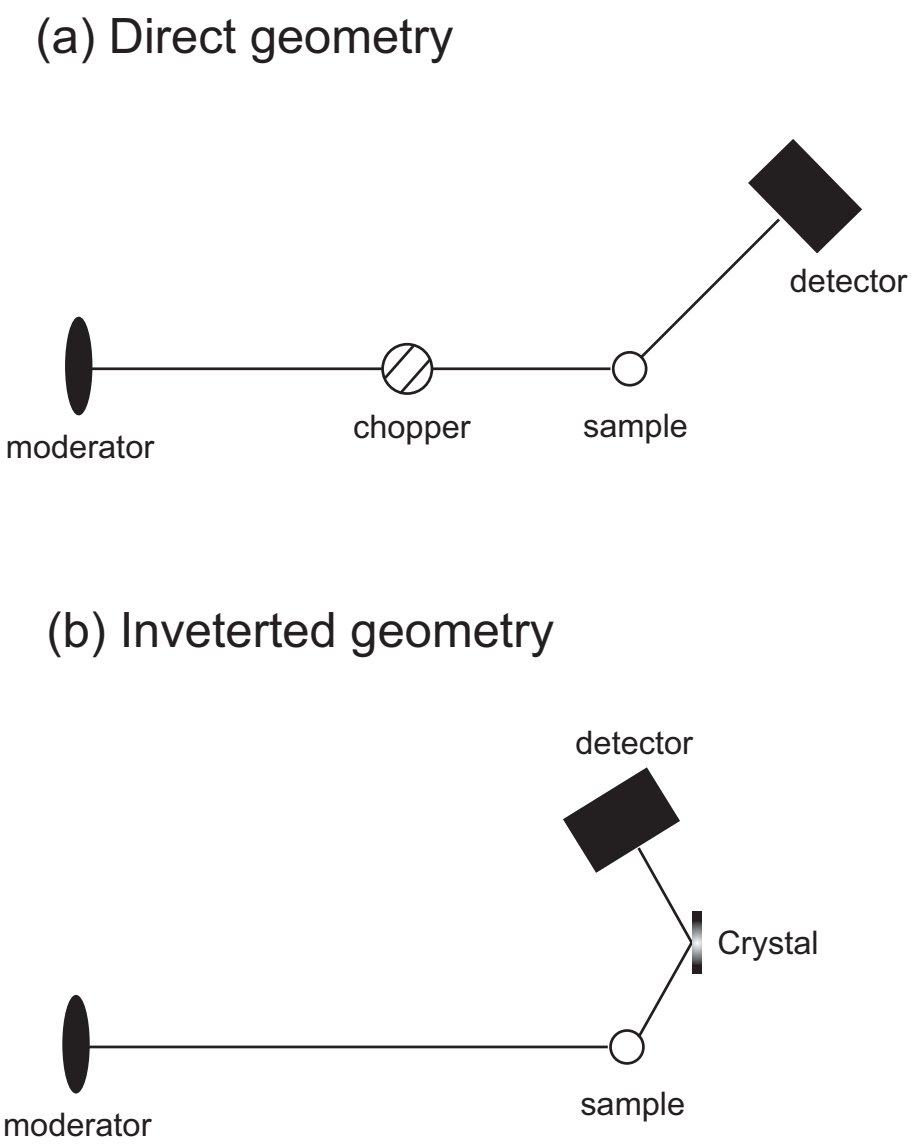

Figure 2.7: Simplified schematic view of (a) direct geometry and (b) inverted geometry spectrometer at a pulse neutron source.

analyzer to the detector is defined as $L_2/2$. The time (t) after the emission from the moderator to the detector is given by

$$t = t_1 + t_2 = \frac{L_1}{v_1} + \frac{L_2}{v_2}, \tag{2.110}$$

where v_1 and v_2 are the incident and scattered neutron velocities, respectively. Normally L_1 and L_2 are known and v_2 is calculated from wavelength that was detected by energy analyzer mirror, therefore we can readily calculate the incident neutron velocity (v_1) and energy (E_1) by the below equations.

$$E_1 = \frac{1}{2} m_n {v_1}^2 = \frac{1}{2} m_n \frac{L_1}{(t - L_2/v_2)^2} \tag{2.111}$$

$$k_1 = \frac{2\pi}{\lambda_1} = \frac{m_n}{\hbar} \frac{L_1}{(t - L_2/v_2)}, \tag{2.112}$$

where m_n is the mass of neutron. We can estimate the energy transfer ΔE and scattering vector $\boldsymbol{Q}$ through

$$\Delta E = E_2 - E_1 = \frac{1}{2} m_n ({v_2}^2 - {v_1}^2) = \frac{\hbar^2}{2m_n} ({k_2}^2 - {k_1}^2) = \hbar\omega \tag{2.113}$$

$$\boldsymbol{Q} = (\boldsymbol{k_2} - \boldsymbol{k_1}) \tag{2.114}$$

$$|\boldsymbol{Q}|^2 = |\boldsymbol{k_1}|^2 + |\boldsymbol{k_2}|^2 - 2|\boldsymbol{k_1}||\boldsymbol{k_2}| \cos\theta. \tag{2.115}$$

2.2.2 Spectrometers

(1) LAM-40 spectrometer [5]

Figure 2-8 indicates the schematic view of LAM-40, installed at the cold neutron source High Energy Accelerator Research Organization (KEK), Tsukuba, Japan. There are seven analyzer mirror with interval of 16 degree on a turn table. 72 pieces of pyrolytic graphite (PG) with the size of 12 mm×12 mm×2 mm were used as energy analyzer mirror and the Bragg angle for the energy analysis of scattered neutron was set to 39 degree. The wavelength of scattered neutron was 4.3 Å because d spacing of 002 of PG was 3.38 Å and the first flight path (L_1) and the second flight path (L_2) was 5.67 m and 1.2 m, respectively. In order to eliminate higher order reflection by PG, Be filter was installed just in front of ^{3}He counter. The energy resolution of LAM-40 was 0.20 meV at half width at half

maximum in neutron energy gain side and it has an energy window of about -2 meV to 10 meV. The length of scattering vector Q at the elastic position ranges from 0.2 to 2.6 Å^{-1}.

(2) MARI spectrometer [6]

Figure 2-9 indicates the schematic view of MARI, installed at S6 beam line in ISIS and views a CH_4 moderator cooled to 100 K. MARI is a direct geometry chopper spectrometer and the incident neutron energy can be changed from 9 to 1000 meV by Fermi chopper. The first flight path (L_1) and the second flight path (L_2) are 11.7 m and 4.00 m, respectively to give an energy resolution ($\delta E/E$) of 1$\sim$2 % and all the detectors are at the same secondary flight path, and the resolution is constant for all the detector banks. Two background suppression choppers are used, the first is a Nimonic chopper and the second is a disc chopper made of Boronated resin with a single hole. At present 922 detectors are installed and they are 10 bar ^{3}He gas proportional counters and their efficiency and background are almost the same. These detectors cover the angular range from 3 degree to 135 degree.

(3) OSIRIS spectrometer [7]

Figure 2-10 indicates the schematic view of OSIRIS, installed at the N6 (B) beam line in ISIS and views a decoupled liquid hydrogen moderator cooled to 22 K. The first flight path (L_1) and the average second flight path (L_2) are 34.0 m and 1.58 m, respectively. The pyrolytic graphite (PG) analyzer bank on OSIRIS is set approximately 0.9 m from the sample positioning the horizontal scattering plane and covers the scattering angles from 11 to 155 degree. The analyzed beam is almost back scattered at approximately 170 degree and detected using a multi-detector composed of 40 rows by 226 column array of PG crystals (10 mm$\times$10 mm$\times$2 mm) with a mosaic spread 0.8 degree mounted on an elliptically machined aluminum backing plate. The graphite analyzer intercepts about 9% of the total scattered beam. PG(002) affords with analyzing energy of 1.85 meV,

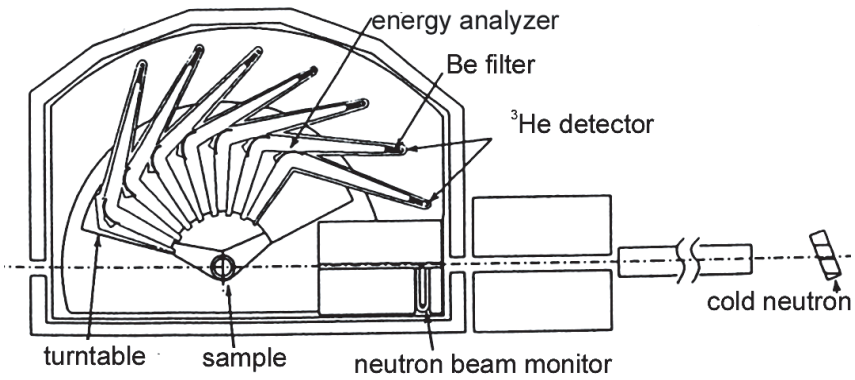

Figure 2.8: Schematic view of LAM-40.

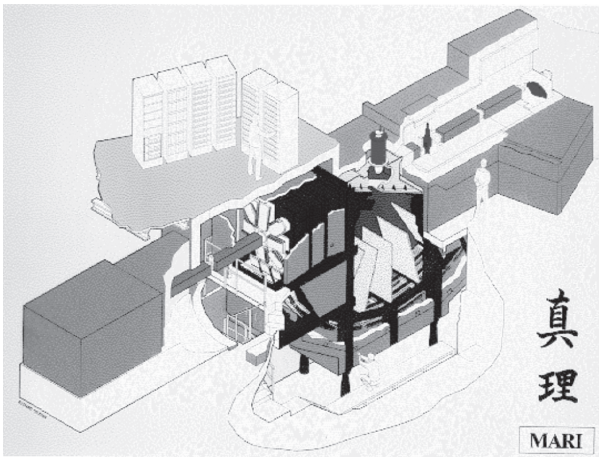

Figure 2.9: Schematic view of MARI.

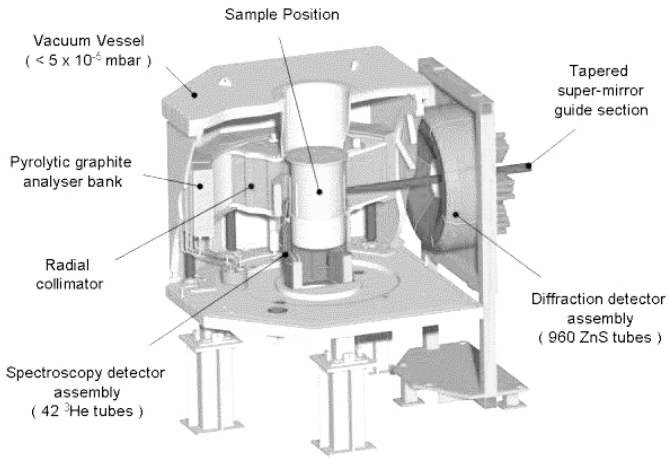

Figure 2.10: Schematic view of OSIRIS.

providing the energy resolution of 24.5 μeV at half width half maximum and the momentum transfer range at elastic position is from 0.18 Å^{-1} to 1.8 Å^{-1} .

2.3 Sample Preparation

Finally we would like to describe the detail of sample preparation for inelastic neutron scattering measurements and the detail of sample preparation for neutron reflectivity will be described in Chapter 8. We used polystyrene (PS) because physical properties of the PS thin films have been studied by various methods. PS thin films were prepared by spin-coating toluene solutions at 2000 rpm on flat glass plates rinsed with toluene prior to the spin-coating. The film thickness was controlled by changing the concentration of PS solution. Such prepared thin films were removed from the glass plate onto water surface carefully and then collected on Al foil 15 mm thick, as shown in Figure 2-11. Collected thin films were annealed at 413 K, which is well above bulk T_g ($\sim$373K) after drying in vacuum for two days. After the annealing, about 300 sheets of thin films on Al foil were rolled up and placed into a hollow cylindrical Al cell. Even though we used 300 sheets of PS thin films on Al foil, transmission of neutrons for 300 and 1000 Å thin films was 95 %, hence multiple scattering effect was almost negligible for the inelastic neutron scattering measurements.

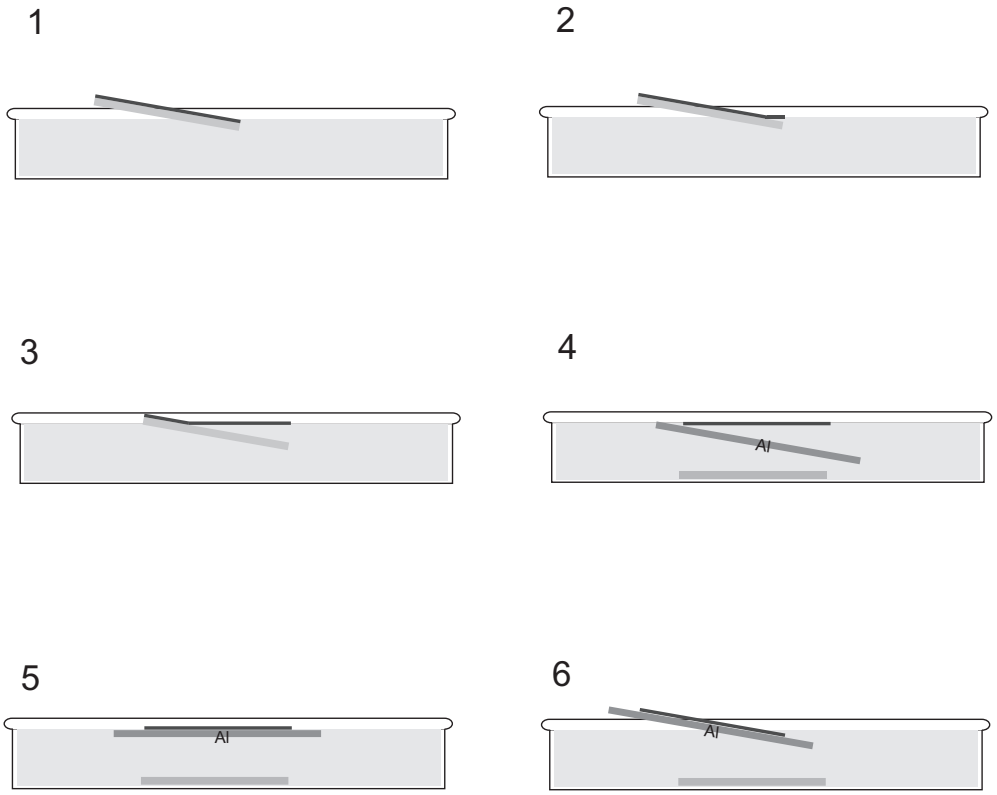

Figure 2.11: Schematic view of how to remove thin film from glass plate on water surface, and collect on Al foil.

References

[1] *Chemical Applications of Thermal Neutron Scattering*, edited by B. T. M. Wills, (Oxford University Press, 1997).

[2] L. Van Hove, Phys Rev. **95**, 249 (1954).

[3] M. Bée, *Quasielastic Neutron Scattering, Principles and Applications in Solid State Chemistry, Biology and Materials Science* (Bristol, 1988).

[4] NEUTRON DATA BOOKLET 2nd EDITION, edited by A. Dianoux, and G. Lander, (ocpscience, 2003).

[5] K. Inoue, Y. Ishikawa, N. Watanabe, K. Kaji, Y. Kiyanagi, H. Iwasa, and M. Kohgi, Nucl. Instr. Methods A **238**, 401 (1984).

[6] K. Yamada, M. Arai, Y. Endho, S. Hosoya, K. Nakajima, T. G. Perring, and A. D. Taylor, J. Phys. Soc. Jpn. **60**, 1197 (1991).

[7] M. T. F. Telling, and K. H. Anderson, Phys. Chem. Chem. Phys. **7**, 1255 (2005).

Chapter 3

Glass Transition Temperature (T_g) of Polystyrene Thin Films on Al Deposited Si Substrate

3.1 Introduction

It was reported that the glass transition temperature (T_g) of polystyrene (PS) thin films decreased with film thickness by various methods like ellipsometry, X-ray, neutron reflectivity, positron annihilation lifetime spectroscopy (PALS) and so on [1-6]. The decrease of T_g with film thickness was understood under the assumption that the mobile surface layer existed at the free surface. On the contrary, the situation is different in the case of poly(methylmethacrylate) (PMMA). Both increase or decrease of T_g were observed with decreasing film thickness depending on the surface nature of substrate [7,8]. On the basis of these experimental results, it was supposed that T_g of polymer thin films seemed to be strongly affected by surface or interfacial effects.

We observe the dynamical behavior of polymer thin films directly in order to understand the glass transition of polymer thin films because the glass transition is a relaxational process. Inelastic and quasielastic neutron scattering can probe molecular level dynamics and such a molecular level dynamics has not been studied very much, therefore using inelastic and quasielastic scattering supposed to be effective for the investigation of dynamics of polymer thin films. For the inelastic and quasielastic scattering study, we have to minimize the background and scattering from substrate because the scattering intensity from thin films is extremely weak. The neutron scat-

tering cross-section from Al is smaller than that from Si, hence Al is the candidate for the substrate for neutron scattering. Fukao et al. investigated the thickness dependence of T_g by thermal expansion spectroscopy and dielectric relaxation using PS thin film that was sandwiched with Al and found the decrease of T_g with film thickness [6]. However, there are no experimental results on T_g of PS thin films on Al substrate. Therefore we studied the Al effect on T_g of PS thin films on Al deposited Si substrate by measuring the film thickness by an ellipsometry as a function of temperature in this chapter.

3.2 Experimental

We used amorphous polystyrene (PS) with different molecular weight (M_w) 2.90×10^5 and the molecular weight distributions (M_w/M_n) 1.06, where M_w and M_n are the weight-average and the number-average of the molecular weight, respectively. Al deposition onto Si wafer was conducted with electron beam (EB) deposition by YAMANAKA SEMICONDUCTOR Co., LTD. The thickness of Al layer was at around 100 nm. PS thin films were prepared by spin-coating toluene solutions at 2000 rpm on the Al deposited Si substrate rinsed in toluene prior to spin-coating. The film thickness was controlled by varying the concentration of PS in solution and we annealed at 413 K for 12 h after drying in vacuum at room temperature for 2 days. The ellipsometry measurements were done with spectroscopic ellipsometer (M-2000, J. A. Woolam, USA) equipped with a temperature-controlled vacuum cell [9]. The sample was heated continuously at a constant rate of 1.62 K/min as indicate in Figure 3-1. This data guaranteed the good linear relation of temperature versus time during the measurements.

3.3 Results and Discussion

Figure 3-2 indicates the temperature dependence of film thickness normalized to that at room temperature for 4 different thicknesses at room temperature. Due to the difference of thermal expansivity between glassy state and molten state, we could

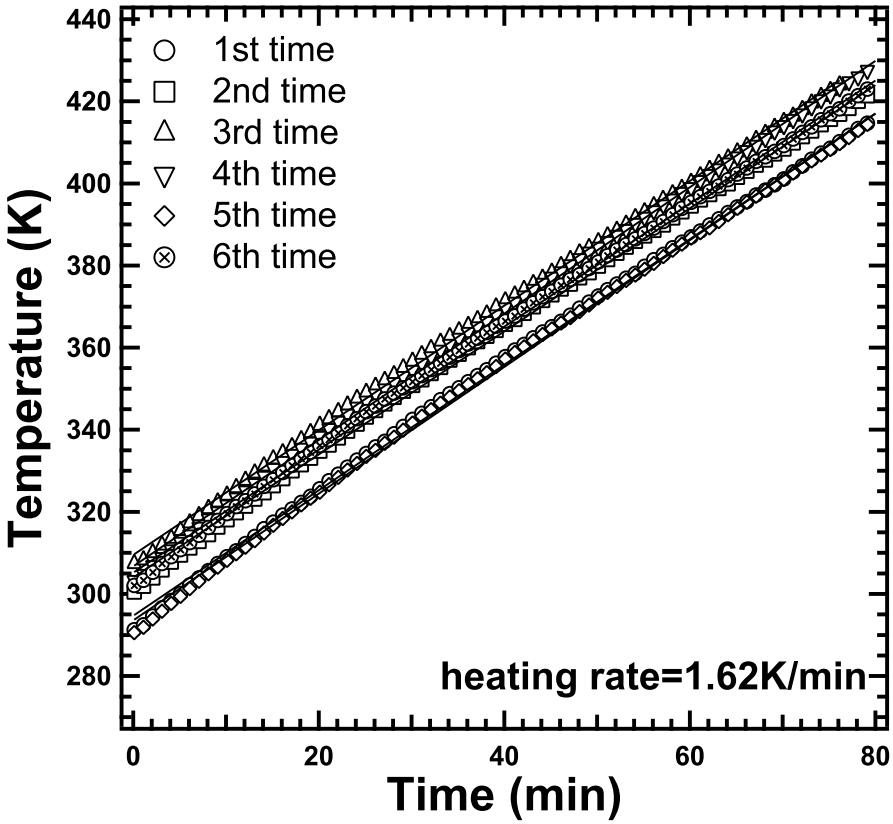

Figure 3.1: Time dependence of monitored sample temperature during ellipsometry measurements.

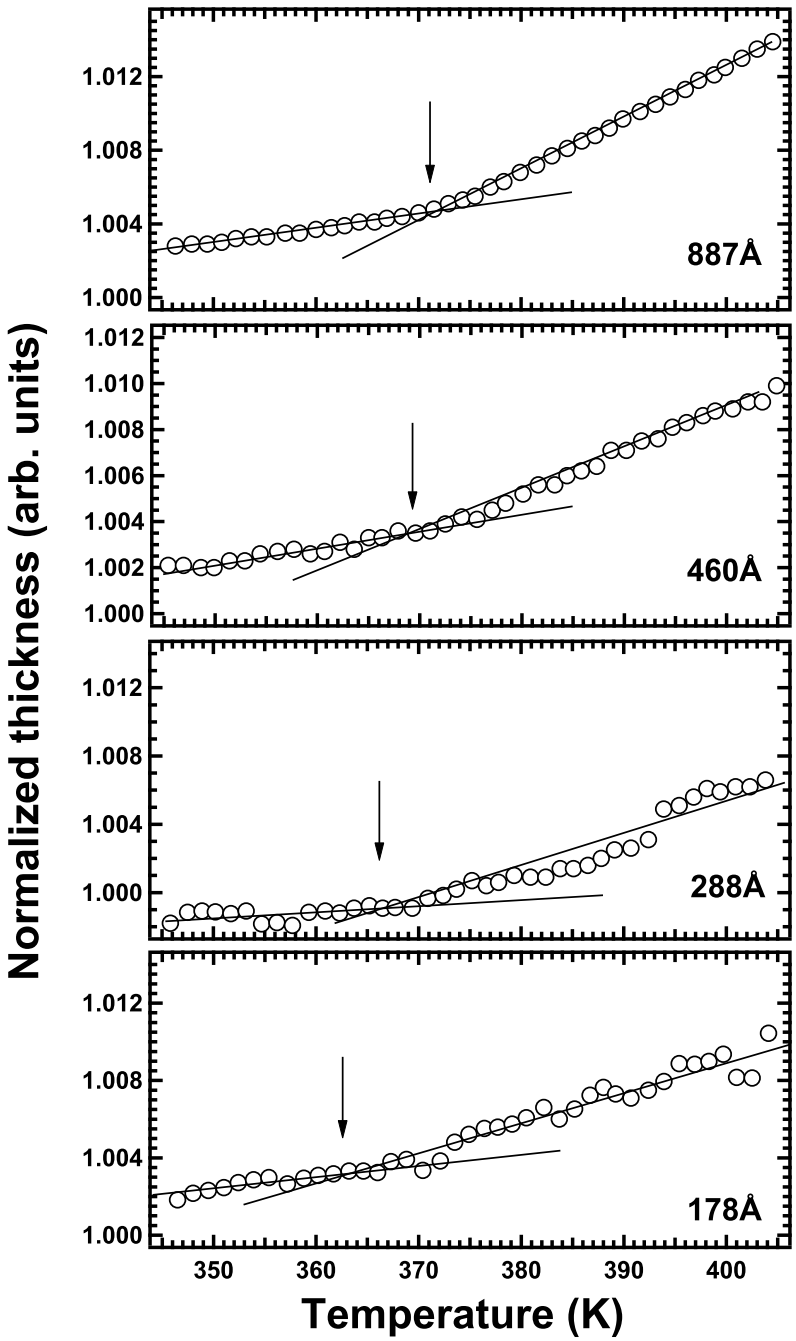

Figure 3.2: Temperature dependence of film thickness normalized by thickness at room temperature, which is shown in each box and the arrows indicate T_g.

observe the change of slope. For a thick film (=1650 Å), which is not shown in Figure 3-2, the change of slope was observed at around 373 K, which is almost same as a bulk T_g determined by differential scanning calorimetry (DSC). We could also evaluate the thermal exapnsivity of thin films from the temperature dependence of thickness, however the exact evaluation of thermal expnasivity is extremely difficult because thermal expansivity is strongly affected by thermal history [10]. Miyazaki et al. reported that T_g value was not affected by annealing time after annealing above T_g for 2 hours [3] and our annealing condition satisfied the restriction. Hence we don't discuss the estimation of thermal expansivity of thin films and we only focused on T_g of thin films in this chapter. As indicted by arrows in Figure 3-2, T_g shifted to lower temperature with decreasing film thickness and it indicated the similar thickness dependence of T_g with that for PS on Si substrate [1-3]. We also compared our data for the PS thin films on Si substrate studied by X-ray reflectivity (XR) [3]. The thickness dependence of both data was shown in Figure 3-3 and almost similar tendency was obtained within experimental error regardless of Al deposition. We try to evaluate the surface T_g and thickness of surface layer by assuming a two-layer model consisting of a surface layer and a bulk-like layer. In this model, the thickness dependence of the T_g is described as followed,

$$T_g = \frac{1}{D}(A \cdot T_g^{surf} + (D - A) \cdot T_g^{bulk}) \tag{3.1}$$

where D and A are the total film thickness and the surface layer thickness, and T_g^{bulk} and T_g^{surf} are the bulk T_g and the T_g of surface layer. The solid line in Figure 3-3 indicates the result of fit with (3.1) and the evaluated surface T_g was 357.4 K and thickness of surface layer was 84 Å and these values are similar to the reported values by Miyazaki et al. [3]. It seems that the existence of free mobile surface is supposed to be the main reason for the decrease of T_g and the effect of substrate on T_g is small in the case of PS. From ellipsomerty measurements, we could show that the thickness dependence of T_g of PS thin films on Al deposited Si substrate was very similar to that on Si substrate, confirming the effects of Al on T_g are not different from Si. This gives a basis on the discussion in Chapter 7 where inelastic neutron scattering results on PS

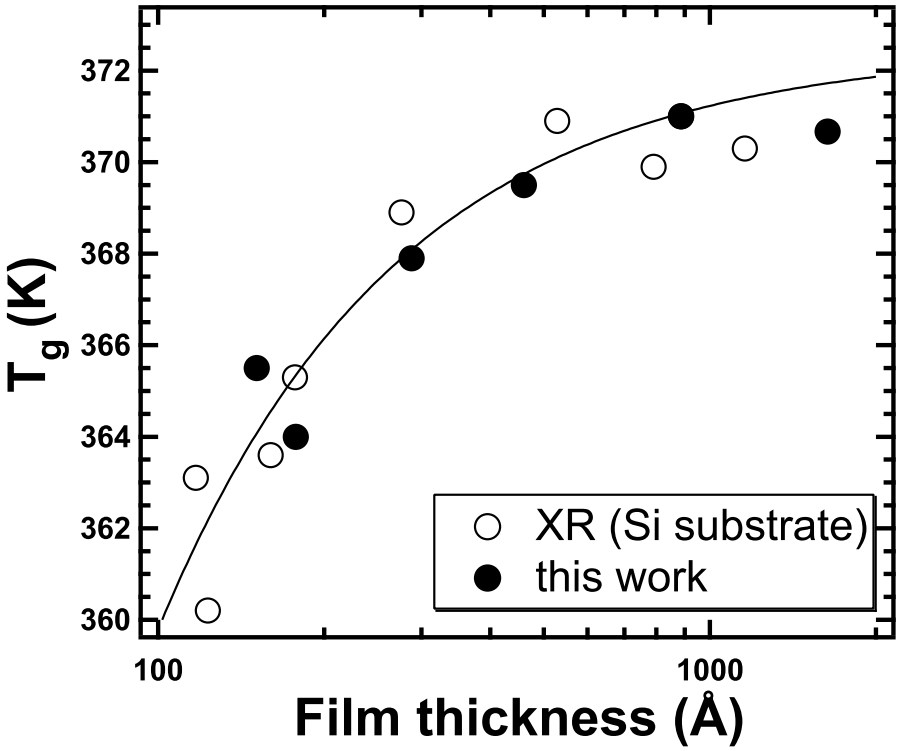

Figure 3.3: Thickness dependence of T_g obtained from this work (•) and the data obtained from XR (◦) and solid line is the result of fit with two-layer model.

thin films on Al substrate were compared with those on Si substrate.

3.4 Conclusion

In this chapter, we have studied the effect of Al on thickness dependence of T_g and found that T_g decreased with film thickness. The obtained results exhibited similar thickness dependence of T_g for PS on Si substrate, which were formerly investigated by various researchers. The result gives a basis on the discussion in Chapter 7 where inelastic neutron scattering results on PS thin films on Al substrate were compared with those on Si substrate.

References

[1] J. L. Keddie, R. A. L. Jones, and R. A. Cory, Europhys. Lett. **27**, 59 (1994).

[2] S. Kawana, and R. A. L. Jones, Phys. Rev. E **63**, 21501 (2001).

[3] T. Miyazaki, K. Nishida, and T. Kanaya, Phys. Rev. E **69**, 061803 (2004).

[4] W. E. Wallace, N. C. Beck Tan, and W. L. Wu, J. Chem. Phys. **108**, 3798 (1998).

[5] G. B. DeMaggio, W. E. Frieze, D. W. Gidley, M. Zhu, H. A. Hristov and A. F. Yee, Phys. Rev. Lett. **78**, 1524 (1997).

[6] K. Fukao, and Y. Miyamoto, Phys. Rev. E **64**, 011803 (2001).

[7] J. L. Keddie, R. A. L. Jones, and R. A. Cory, Faraday. Discuss. **98**, 219 (1994).

[8] D. S. Fryer, R. D. Peters, E. J. Kim, J. E. Tomaszewski, C. C. White, and Wenli-Wu, Macromolecules, **34**, 5627, (2001).

[9] S. Yamamoto, Y. Tsujii, and T. Fukuda, Macromolecules, **35**, 6077, (2002).

[10] T. Kanaya, T. Miyazaki, H. Watanabe, K. Nishida, H. Yamano, S. Tasaki, and D. B. Bucknall, Polymer, **44**, 3769 (2003).

Chapter 4

Low Energy Excitations and Fast Process of Polystyrene Thin Films

4.1 Introduction

Glass transition of polymer thin film is the one of the most interesting topics in the filed of polymer thin film, as was already written in Chapter 3. The glass transition is not a second order thermodynamical phase transition but a relaxational process, and the dynamical studies are needed to understand the mechanism of glass transition of polymer thin film. Dynamical behavior of polymer thin films was investigated by various methods such as dielectric relaxation [1-3], Broullion light scattering [4,5], dynamic light scattering [6], scanning probe microscope [7-11], X-ray photon correlation spectroscopy (XPCS) [12,13] and so on. In spite of the vigorous researches using the above listed methods, the definite mechanism of glass transition is still unknown. Inelastic and quasielastic neutron scattering provides unique information on fast and local dynamics compared to other methods and many dynamical features of bulk amorphous polymers were studied with this method [14-23]. Kanaya et al. successfully revealed that the decrease of thermal expansivity with film thickness was caused by the increase of harmonic force constant using X-ray reflectivity (XR) and inelastic neutron scattering [24]. Inelastic and quasielastic scattering would offer clue to understand the unresolved problems of polymer thin films by combing the results with those from other methods.

There have been a few reports on dynamical studies of polymer thin films with inelastic

neutron scattering and to the results only from elastic scattering were reported due to the extremely weak scattering intensity from the thin films [25-27]. In this chapter we study the dynamical properties of polymer thin films using inelastic and quasielastic neutron scattering from polystyrene thin supported films in meV region in a broad temperature range 11 K to 403 K above bulk T_g. We mainly focused on local dynamics like the low energy excitations including the Boson peak and the so-called picosecond fast process and the effect of the film thickness on such local fast dynamics.

4.2 Experimental

We used polystyrene (PS) with molecular weight $M_w = 2.9\times10^5$ and molecular weight distribution M_w/M_n=1.06, where M_w and M_n are the weight-average and the number-average of the molecular weight, respectively. The bulk glass transition temperature T_g determined by DSC measurements was 373 K. PS thin films were prepared by spin-coating toluene solutions at 2000 rpm on flat glass plates rinsed in toluene prior to spin-coating. The film thickness was controlled by varying the concentration of PS in solution and we prepared films 1000 Å and 400 Å thick. The film was removed from the glass plate onto water surface and then collected on Al foil 15 μm thick, and then annealed at 413 K for 12 h after drying in vacuum at room temperature for 2 days. 299 sheets of the films on Al foils were rolled up and placed into a hollow cylindrical Al cell 14 mm in diameter and 45 mm high in order to get enough inelastic scattering intensity. Bulk PS sample with thickness of 0.1 mm was prepared as a control sample.

The inelastic neutron scattering measurements were performed with an inverted geometry time of flight (TOF) spectrometer LAM-40 [28] installed at the cold spallation neutron source in High Energy Accelerator Research Organization (KEK), Tsukuba, Japan. In the spectrometer, the final energy of neutron and the energy resolution was 4.59 meV and ∼0.2 meV at the elastic position, respectively. The detail of inelastic and quasielastic scattering measurements were described in chapter 2. The measurements were carried out at temperatures from 11 K to 430 K, covering the bulk glass transition temperature T_g of 373 K. The observed TOF spectra of the 299 thin films on Al foils and

the empty can including 299 Al foils were corrected for the self-shielding, the counter efficiency and the incident neutron spectrum at each temperature and the empty can scattering was carefully subtracted from the sample scattering. The PS used in this experiment is fully protonated one, and the scattering intensity obtained here is mainly dominated by the incoherent scattering because the incoherent atomic scattering cross-section of hydrogen atom is much larger than coherent cross-section of hydrogen and incoherent/cohernet cross-section of carbon atom.

4.3 Results and Discussion

Figures 4-1(a) and (b) indicate the dynamic scattering laws $S(Q, \omega)$ of the films 400 and 1000 Å thick at temperatures from 11 K to 408 K, respectively, which were obtained by summing up 6 spectra from $Q = 0.87$ to 2.47 Å^{-1}. The intensities were normalized to the total scattering intensity at the lowest temperature 11 K. A broad inelastic peak, which is the so-called Boson peak [21,22] characteristic to amorphous materials, is observed at around 1.5 meV at low temperatures below about 150 K. With increasing temperature, the shape of spectrum changes from inelastic-like to quasielastic-like, implying the onset of a relaxation process, which is the so-called picosecond fast process [14-19].

First we analyzed the elastic scattering intensity $I_{el}(Q)$ to evaluate the mean square displacement $< u^2 >$. It is known that the Q dependence of incoherent elastic intensity $I_{el}(Q)$ is related to $< u^2 >$ through $I_{el}(Q) \sim \exp[- < u^2 > Q^2]$. According to this relation we plotted the elastic scattering intensity $I_{el}(Q)$ against Q^2. In Figure 4-2, an example of such plot is shown for the bulk and the 1000 Å and 400 Å films at 230 K, where the elastic scattering intensity $I_{el}(Q)_{230\mathrm{K}}$ is divided by$I_{el}(Q)_{11\mathrm{K}}$ at the lowest temperature 11 K in order to reduce the effect of coherent scattering under an assumption that the structure factor does not change with temperature. Therefore, the observed $< u^2 >$ corresponds to $< u^2 >_{230\mathrm{K}}$ - $< u^2 >_{11\mathrm{K}}$, meaning that the $< u^2 >$ is zero at 11 K. The decrease of slope, which corresponds to $< u^2 >$ was observed with film thickness. Similar evaluation was done at each temperature, and the

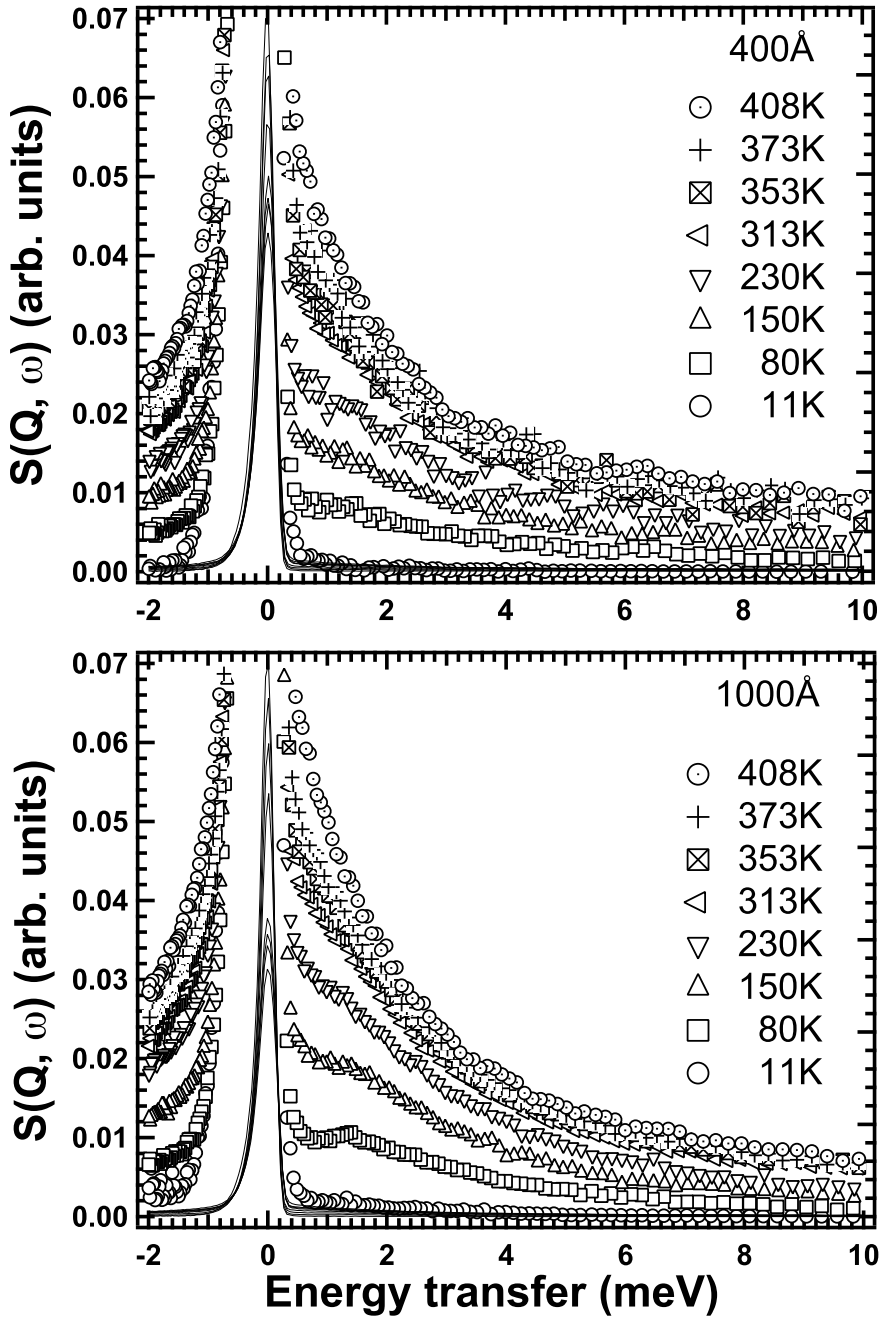

Figure 4.1: Dynamic scattering law $S(Q, \omega)$ of PS thin films measured with LAM-40 at various temperatures. (a): 400 Å and (b): 1000 Å. Solid curves show whole shapes of the spectra at each temperature and symbols are the expanded ones by factor 60.

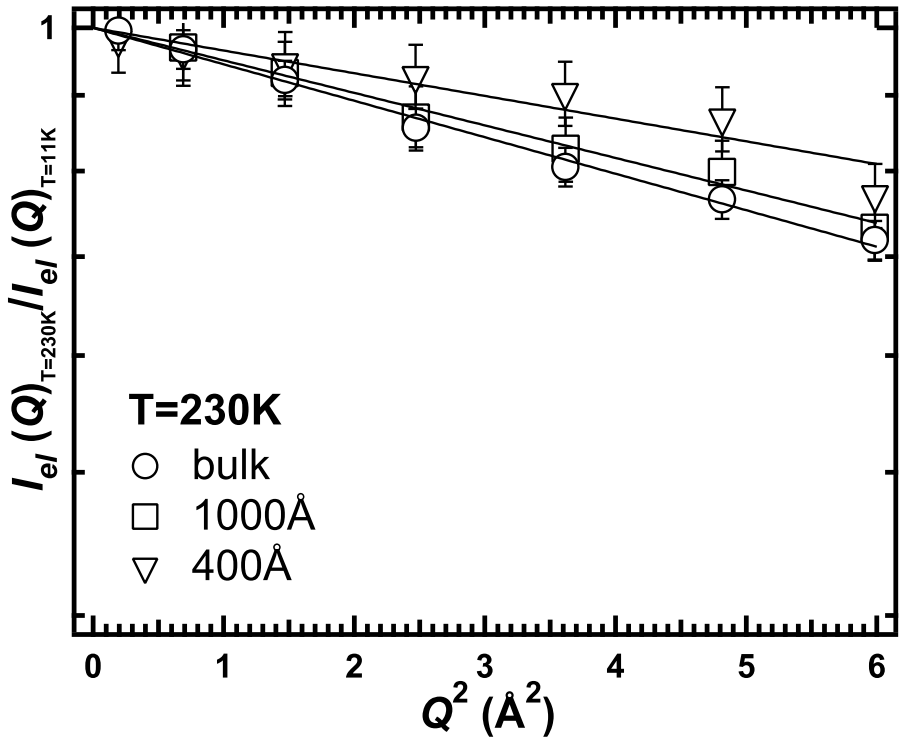

Figure 4.2: Q^2 dependence of elastic intensity $I_{el}(Q)$ at 230 K divided by that at 11 K: bulk(○),1000 Å (□), and 400 Å (▽).

temperature dependence of $< u^2 >$ is shown in Figure 4-3 for the bulk and the 1000 Å and 400 Å thin films. The mean square displacement $< u^2 >$ is almost proportional to T in the low temperature range below about 150 K as indicated by solid lines in the figure, showing harmonic nature of the vibration. The solid lines were drawn so as to go through $< u^2 >=0$ at T=11 K. As temperature further increases, the mean square displacement begins to deviate from the linear relationship and shows excess value over the harmonic contribution. This anharmonic contribution is caused by the onset of the picosecond fast process. The deviation temperature lies at around 150 K for bulk [15,16] and the 1000 Å film, but seems to shift to higher temperatures for the 400 Å tilm although the exact evaluation is not easy from this data only. It should be noted that the glass transition temperature T_g is not detected in the measurements because the so-called α-process is not observed with the present energy resolution (δE ~0.2 meV). In the whole temperature range examined the mean square displacement $< u^2 >$ decreases with the film thickness. As an example, the mean square displacement $< u^2 >$ at 80 K, which is in the harmonic temperature range, is plotted against the film thickness in Figure 4-4. The mean square displacement $< u^2 >$ of harmonic vibration is related to the density of phonon states $G(\omega)$ through the following relation [29]

$$< u^2 >= \frac{3\hbar}{2M} \int_0^\infty \frac{1}{\omega} \coth\Big(\frac{\hbar\omega}{2k_B T}\Big) G(\omega) d\omega. \tag{4.1}$$

The decrease in $< u^2 >$ with the film thickness below about 150 K suggests that the density of phonon states $G(\omega)$ is shifted to a high energy side or reduced in a low energy side. In other words, hardening of vibration mode occurs with decreasing the PS film thickness.

In order to see the origin of the hardening we analyze the inelastic scattering part of the thin films. The observed $S(Q, \omega)$ at 80 K was converted to the density of phonon states $G(\omega)$ after subtracting the elastic contribution and correcting for the Debye-Waller factor. For the subtraction, the elastic line was reconstructed from the sample scattering at 11 K because the shape of the elastic line is affected by the sample shape, and in addition the inelastic scattering at 11 K was evaluated from the spectrum at 80 K. The Debye-Waller factor used in the calculation of $G(\omega)$ was evaluated from the

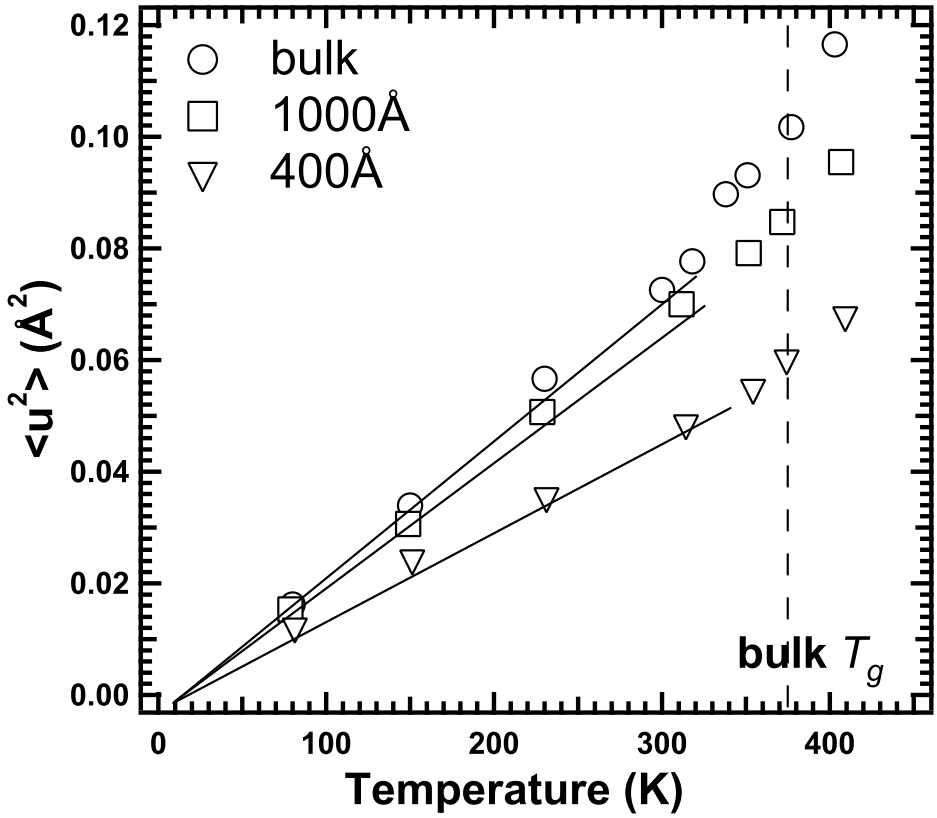

Figure 4.3: Temperature dependence of mean square displacement $< u^2 >$: bulk(○),1000 Å (□), and 400 Å (▽). Dashed line shows bulk glass transition temperature T_g.

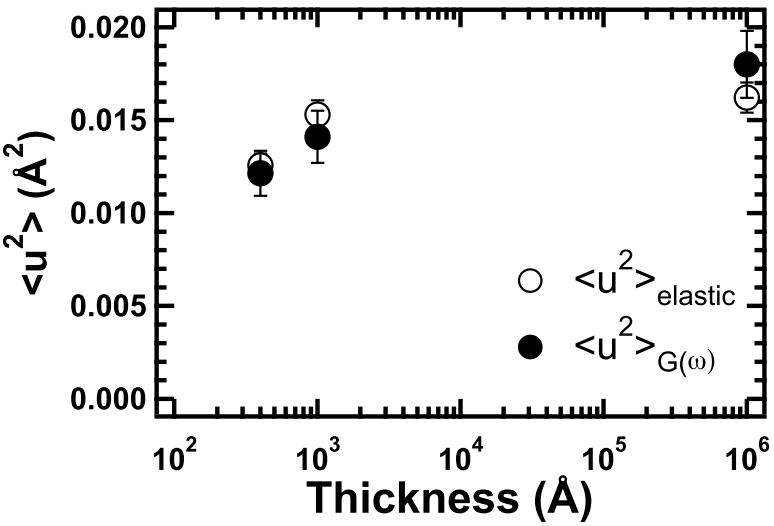

Figure 4.4: Thickness dependence of $< u^2 >_{\text{elastic}}$ evaluated from the elastic scattering intensity (○) and $< u^2 >_{G(\omega)}$ calculated from density of phonon states at 80 K(●).

elastic intensity. The evaluated $G(\omega)/\omega^2$ are shown in Figure 4-5 for the bulk and the 1000 and 400 Å films. It is clear that the $G(\omega)$ decreases with the film thickness in the energy region of 1 to 10 meV, suggesting that the decrease in $< u^2 >$ is caused by the decrease in $G(\omega)$. Using the observed $G(\omega)$, we have calculated $< u^2 >$ for the bulk and the 1000Å and 400Å films at 80 K through eq. (1) with $M = 104$ (monomer mass). The absolute value of $G(\omega)$ was evaluated by calculating heat capacity from $G(\omega)$ and comparing with the measured one [30], and was smoothly extrapolated to $3/{\omega_D}^3$ at 0 meV, where ω_D is the Debye frequency calculated from the sound velocity obtained in Brillouin scattering. In the calculation we took into account contributions from the Debye mode and the Boson peak mode, and the contribution of the Debye mode in $G(\omega)$ was evaluated from the Debye frequency ω_D. The contribution of the Boson peak mode was obtained by subtracting the Debye contribution from the total one. For the thin films the Debye contributions were estimated assuming that the amplitudes of the Debye mode and the Boson peak mode are independent of film thickness. The calculated $< u^2 >$ was plotted in Figure 4-4 as a function of film thickness. It is clear that the reduction in $< u^2 >$ could be attributable to the reduction in $G(\omega)$.

We now consider which mode is hardening or reduced with decreasing the film thickness in the low energy region below about 10 meV. In this energy region there exist at least two modes [21]: the localized mode (Boson peak mode) and the extended mode (Debye mode). As seen in Figure 4-5, the Boson peak energy (or frequency) lies at around 1.5 meV for all the samples and the peak position is independent of film thickness within the experimental error. If we assume the peak energy is simply given by $\omega = \sqrt{f/m}$, where f and m are the harmonic force constant and the effective mass, the present result means the hardening of the Boson peak mode is very small. Nevertheless, we observed the reduction in $G(\omega)$ with the film thickness. The Debye contribution $G_D(\omega)$ to the density of phonon states was calculated for the bulk and the thin films under an assumption that the amplitude of the two modes are independent of film thickness and indicated in Figure 4-5 by dashed lines, showing the clear decrease in $G_D(\omega)$. We also evaluated the contribution of the Boson peak mode $G_B(\omega)$ to the density of phonon

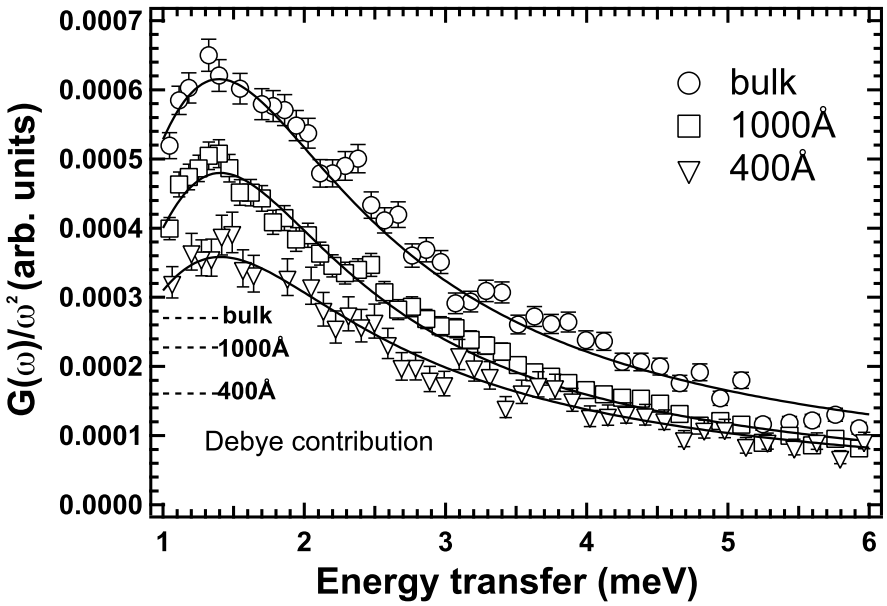

Figure 4.5: Density of phonon states $G(\omega)$ divided by ω^2: bulk(○),1000 Å (□), and 400 Å (▽). Dotted lines show the Debye contributions $G_D(\omega)/\omega^2$.

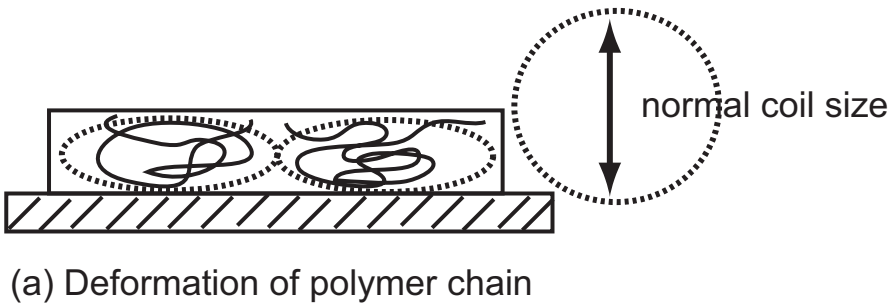

(a) Deformation of polymer chain

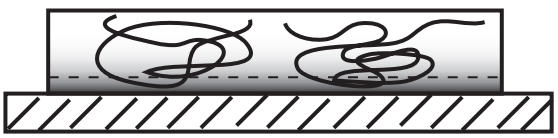

(b) Hard layer at the interface (dead layer)

Figure 4.6: Schematic view of molecular pictures for the hardening with decreasing the film thickness. (a) Deformation of polymer chain. (b) Hard layer at the interface (dead layer).

states by subtracting the Debye contribution $G_D(\omega)$ from the total one, and found that $G_B(\omega)$ also decreased with film thickness although the Boson peak energy is unaltered with the film thickness. Therefore, the observed decrease in $< u^2 >$ could be attributed to the decrease in the density of phonon states in both the Debye mode and the Boson peak mode.

We proposed two molecular pictures for the hardening with decreasing the film thickness. One is the hardening due to polymer chain confinement in a thin film. In a thin film below polymer coil size, which can be represented by twice the radius of gyration ($2R_g$), polymer chains could not sustain the normal coil form and the deformation would occur as shown in Figure 4-6(a). Such deformed polymer chains would have higher restoring force than that of normal coil, resulting in the increase of f with decreasing film thickness. In fact, the R_g of PS used in this experiment is about 147 Å [31] and the twice of R_g is about 294 Å. Taking into account of the distribution of polymer coil sizes, the confinement effects may be expected for the 400Å film, but not for the 1000 Å film. Nevertheless the reduction in $< u^2 >$ was observed even in the 1000 Å film. This implies another possibility for the hardening. A hard layer at the interface, which is often called "dead layer" [32], is also a candidate for the hardening. If we assume such hard layer with constant thickness independent of total film thickness at the interface, it is expected that the average force constant increases with decreasing the total film thickness because the fraction of the hard layer increases with decreasing the film thickness as shown in Figure 4-6(b). Assuming $< u^2 > = 0$ in the hard layer, we estimated that the thickness of the hard layer was at least ∼110 Å, which seems rather large but still in a range of reported values for the hard layer [1, 26, 32]. We would like to discuss which possibility is more plausible to explain the decrease in the density of phonon states of both the Debye mode $G_D(\omega)$ and the Boson peak mode $G_B(\omega)$. The density of phonon states$G_D(\omega)$ of the Debye mode is related to the average sound velocity v through the relation [21] $G_D(\omega) = \frac{4\pi V\omega^2}{v^3}$, where V is the average atomic volume. One possibility for the reduction in the Debye mode is the cut-off of the long wavelength phonon due to the confinement. Zorn et al. explained the decrease of low

frequency mode in salol and polydimethylsiloxane (PDMS) in porous glass in terms of the cut-off of the phonon with wavelength longer than the pore size [33, 34]. We evaluated the sound velocity of PS at 80 K based on the generalized Rao function presented by Schuyer [35]. The cut-off energy (or frequency) using the procedure by Zorn et al. for the 400 Å PS thin films was calculated to be about 0.095 meV. This cut-off energy is located within the elastic scattering in this experiment (δE ~0.2 meV), therefore the cut-off of the long wavelength phonon is not the cause for the reduction in the inelastic intensity above 0.2 meV with the film thickness. Another possibility for the reduction in $G_D(\omega)$ is the increase of sound velocity (v) due to the densification with decreasing the film thickness. It was reported that polymer chains tend to form ordered structure exhibiting layering [36] near the interface that is related to the radius of gyration of polymer [37] as pointed out by Mukherjee et al. [38]. The density of layer at the interface must become larger due to such ordered structure, resulting in the increase in sound velocity with decreasing the film thickness. This ordered layer act as the hard layer (or the dead layer), resulting in the decrease of the Debye contribution $G_D(\omega)$. It is noteworthy that no signs of the free surface were observed in the measurements, to which the reduction in T_g is often assigned. One possibility is that the free surface motion is too slow to be detected with the present energy resolution δE ~0.2 meV.
The hard layer at the interface could explain the decrease in the Boson peak contribution $G_B(\omega)$ as well. The densification near the interface leads to the decrease in the number of defects or voids. If the origin of the Boson peak concerns defects or voids [39-42], the decrease of the defects or voids leads to the decrease in the number of the Boson peak mode, resulting in thee decrease of $G_B(\omega)$, which is a kind of mode reorganization. The concept of chain confinement can explain the decrease of the Debye mode while it seems hard to explain the decrease in the Boson peak mode. Hence, the hard layer or the dead layer seems more plausible to explain the decrease in the density of phonon than the chain confinement in a thin film. Further discussion will be given in Chapter 5.

The energy region that we focused almost corresponds to the temperature region

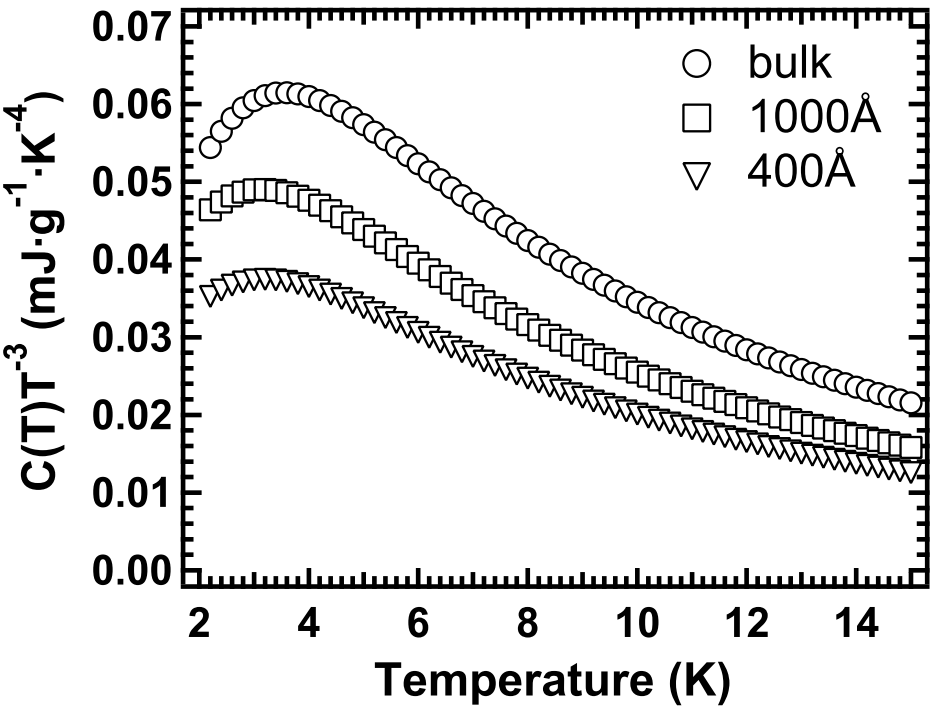

Figure 4.7: Temperature dependence of $C(T)$ calculated from the fitting curves of $G(\omega)$ for bulk ($\circ$) and thin films 1000 Å ($\square$), 400 Å ($\triangledown$) thick.

range of 5 to 20 K. In this temperature range, the heat capacity $C(T)$ much exceeds the value that was expected for crystalline solids due to the existence of Boson peak. The $C(T)$ was calculated from the $G(\omega)$ through the below relation [43].

$$C(T) = \int_0^\infty \frac{e^{\beta\hbar\omega}(\hbar\omega)^2}{(e^{\beta\hbar\omega}-1)^2}\frac{G(\omega)}{k_B T^2}d\omega, \tag{4.2}$$

where $\beta = 1/k_B T$. Lupascu et al. have already measured the $C(T)$ of PS thin films at around T_g [44], however the $C(T)$ due to the Boson peak of polymer thin films has not been studied yet. Therefore, we tried to evaluate the $C(T)$ in the temperature range from 2 K to 15 K. The calculated $C(T)$ of bulk was multiplied by an appropriate factor to fit with the observed $C(T)$ of bulk value because we have not measured absolute $G(\omega)$ values [45]. By multiplying the same factor as bulk, we have calculated the $C(T)$ for bulk, 1000 Å and 400 Å thin films in Figure 4-7. As expected from the thickness dependence of $G(\omega)$, the decrease of $C(T)$ value was evaluated with film thickness.

In the next, we discuss the quasielastic scattering due to the picosecond fast process in a temperature range above about 150 K. The observed dynamic scattering law $S(Q, \omega)$ was scaled by the Bose factor after the correction for the Debye-Waller factor using $< u^2 >$ evaluated from Q^2 dependence of the elastic scattering. The scaled spectra are shown in Figure 4-8 for the 1000 and 400 Å films, where the reference temperature is 80 K. The spectra were well scaled in the energy range above about 1.5 meV including the Boson peak, while below 1.5 meV the excess scattering was pronounced with increasing temperature above about 200 K. This suggests the onset of the so-called fast process [14-19]. In order to see the deviation from the Bose scaling, we integrated the scaled spectrum in the quasielastic region (0.70 meV to 1.5 meV) avoiding the effect of elastic scattering and plotted against temperature in Fig. 4-6 for the bulk and the 1000 Å and 400 Å films. It is hard to estimate the deviation temperature because the data points are rather little and the experimental error is large. We assumed that the deviation for the bulk started at around 150∼200 K as reported in the previous works [15], and that the excess scattering was not yet observed at 150 K as indicated by solid lines in Figure 4-9. From the figure we can say that the temperature dependence of the integrated intensity in the 400 Å thin film is almost flat compared to the bulk and the 1000 Å

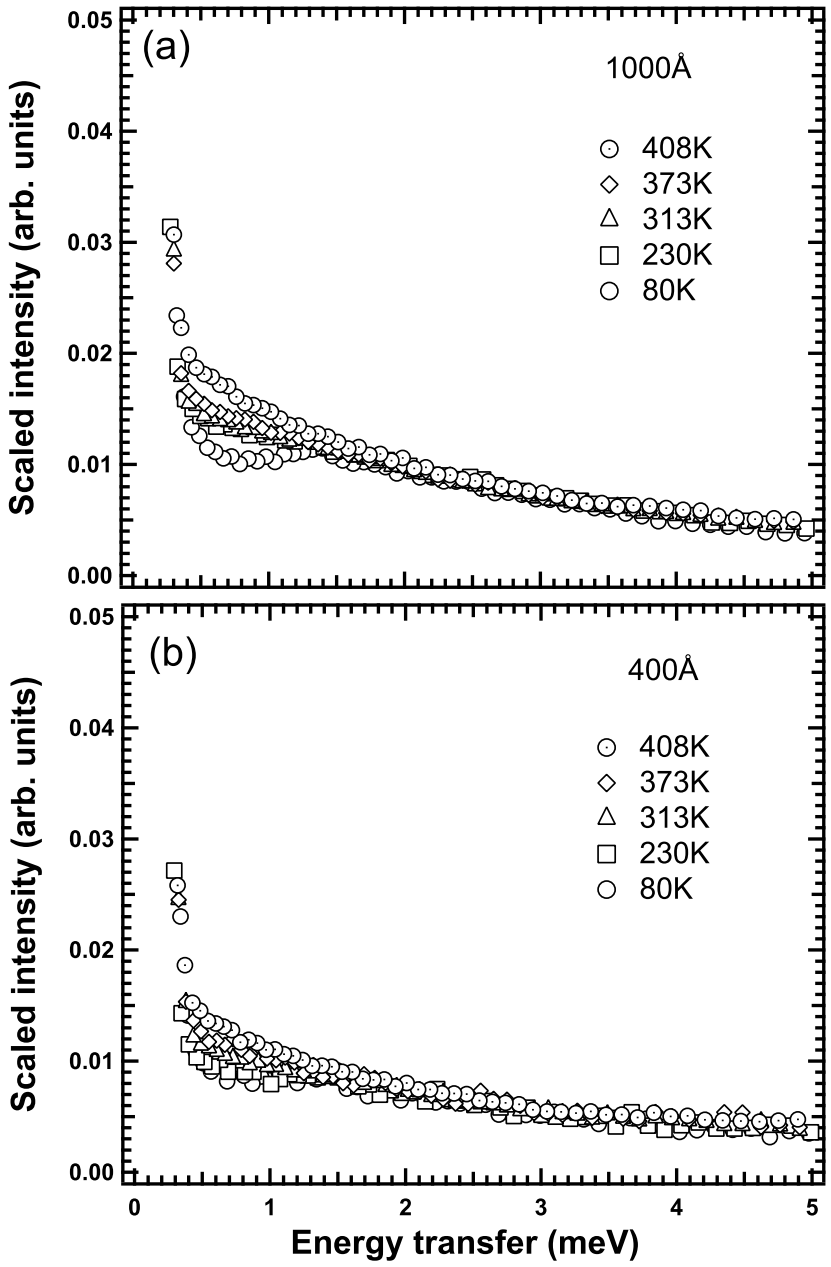

Figure 4.8: Bose-scaled inelastic scattering intensity after correcting for the Debye-Waller factor: (a): 1000 Å and (b): 400 Å. The reference temperature is 80 K for both (a) and (b).

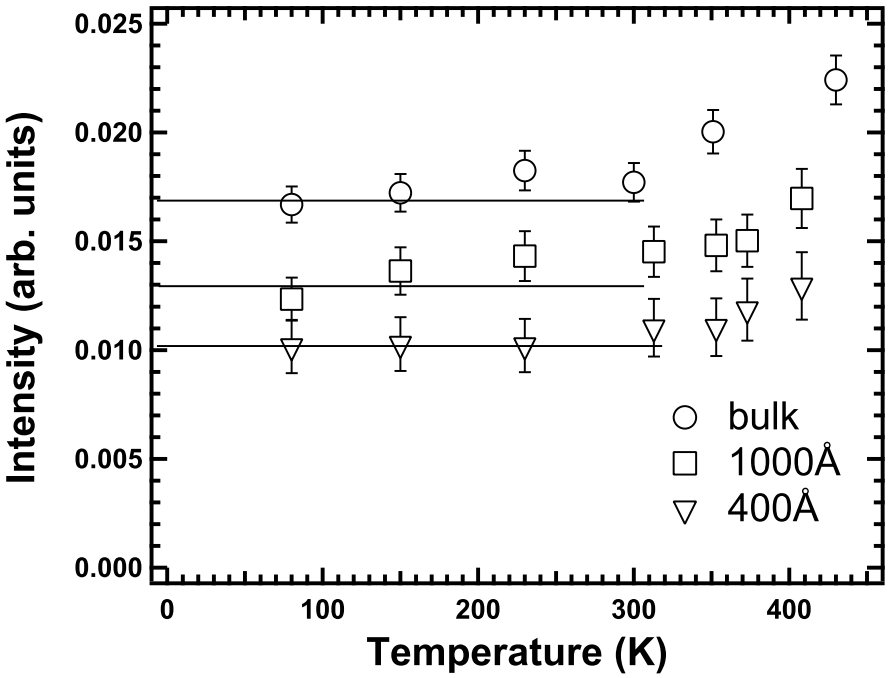

Figure 4.9: Temperature dependence of integrated intensity of the Bose-scaled spectra in Figure 4-8 in an energy range from 0.70 meV to 1.5 meV: bulk (○), 1000 Å (□) and 400 Å (▽).

thin films in a low temperature region below ∼230 K. This qualitatively corresponds to the higher deviation temperature in $< u^2 >$ for the 400 Å film than the bulk and the 1000Å film. The results suggest that the quasielastic scattering due to thermal fluctuations becomes hard to occur in the thinner films, agreeing with the picture of hardening. In order to study the characteristic features of the fast process in more detail, the observed dynamic scattering law $S(Q, \omega)$ were fitted to a model function convoluted with the resolution function of the spectrometer. We employed the following model function which could describe the $S(Q, \omega)$ for the bulk [16].

$$S(Q,\omega) = C(Q)[(1 - A_{fast}(Q))\delta(\omega) + A_{fast}(Q)L(\Gamma,\omega)] + B(Q), \qquad (4.3)$$

where $A_{fast}(Q)$ is a fraction of the fast process, and the $\delta(\omega)$ and $L(\Gamma,\omega)$ are a δ-function and a Lorentzian with an half-width at half-maximum (HWHM) Γ, respectively. $C(Q)$ and $B(Q)$ are constants, representing the Debye-Waller factor and inelastic flat background, respectively. It is not clear how to separate the inelastic scattering component from the fast process. In this fit, it was assumed that the Boson peak could be included in the inelastic flat component $B(Q)$ at least in the limited energy range below 3 meV. A δ-function was introduced to describe immobile parts of polymer chains as well as slow relaxation processes within the energy resolution function such as slow β process, α process and reptation motion [16,46,47]. The results of the fits for the 1000 Å and 400 Å films at 408 K are shown Figure 4-10. We found that he fast process of PS thin films were also described by a single Lorentzian as was the case of the bulk [16]. No other relaxation processes were observed even above T_g except for the fast process in the energy region above ∼0.2 meV, meaning that we could not detect T_g due to the limited energy resolution in this measurement. It is noted that we also performed another analysis, in which we described the Boson peak and the Debye contributions by a spectrum predicted from the 80 K data by the Bose factor and fitted an additional Lorentzian to the observed $S(Q, \omega)$. The results of fits were not bad, but we employed the former model including the inelastic flat background in this report because the deviation plot was better than the latter model. In order to study the nature of the fast process furthermore, logarithms of the relaxation rate Γ

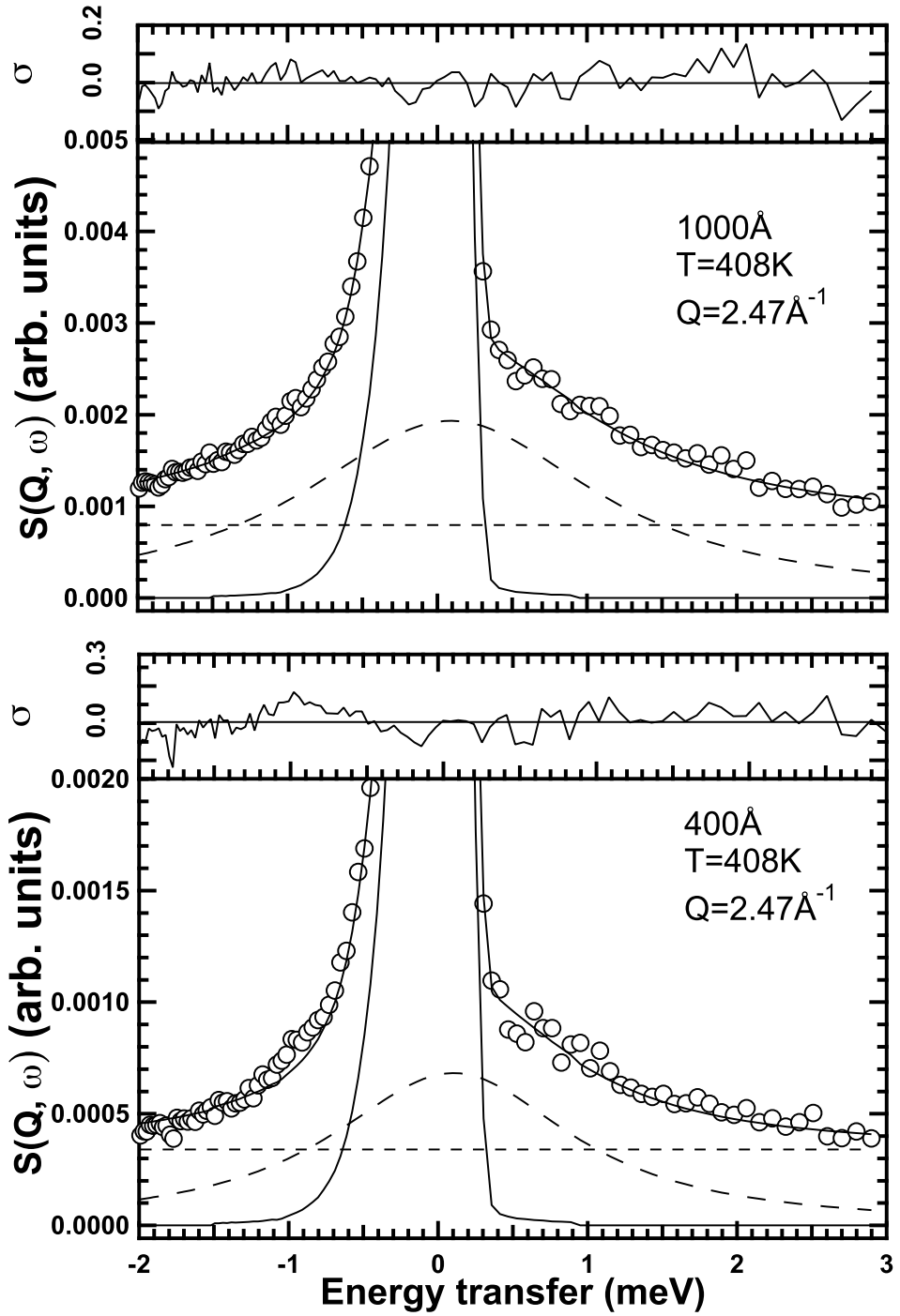

Figure 4.10: Results of curve fitting to the LAM-40 spectra of 1000 Å and 400 Å thin films at $T = 408$ K and $Q = 2.47$ Å^{-1}. (—): elastic component, (– – –): quasielastic Lorentzian and (- - -): flat background.

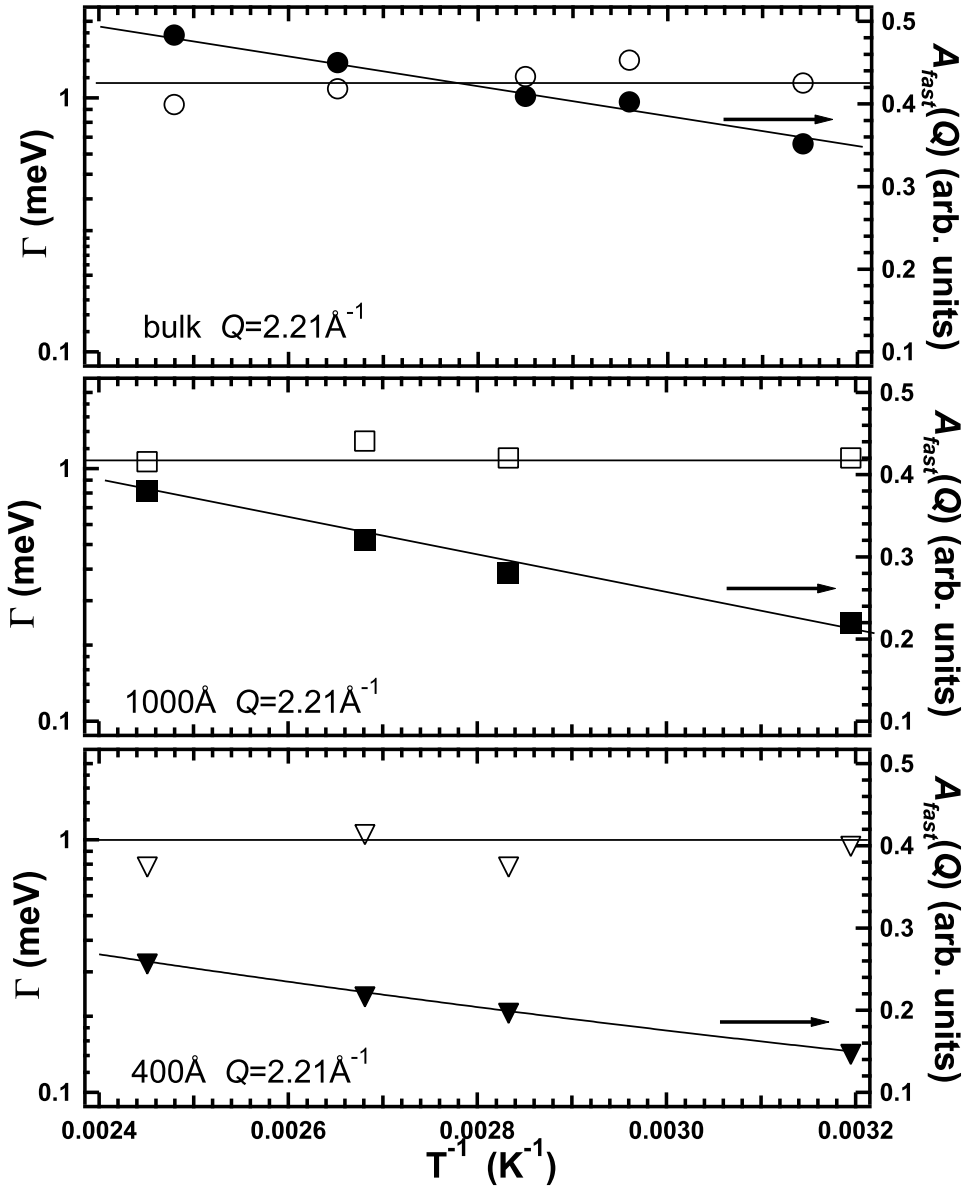

Figure 4.11: Temperature dependence of relaxation rate Γ and fraction $A_{fast}(Q)$ of the fast process. bulk ($\circ, \bullet$), 1000 Å ($\square, \blacksquare$), 400 Å ($\triangledown, \blacktriangledown$). Open and closed symbols correspond to Γ and $A_{fast}(Q)$, respectively.

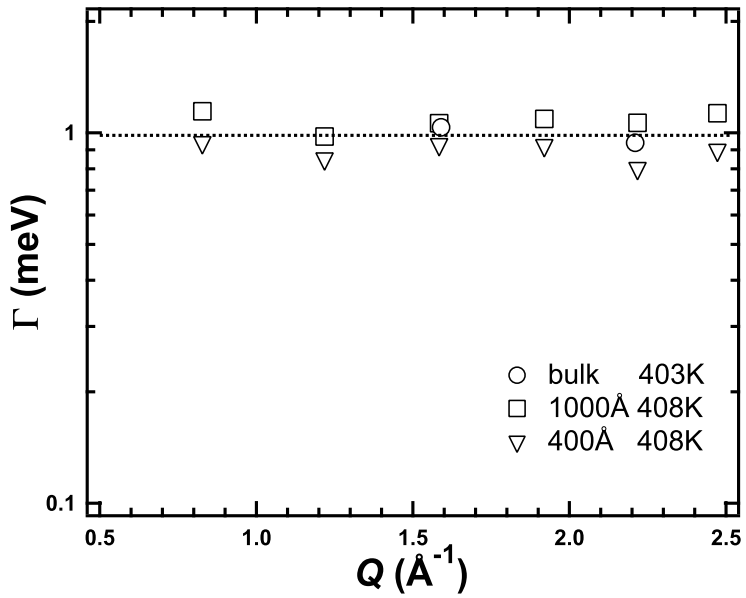

Figure 4.12: Q dependence of relaxation rate Γ of the fast process for bulk (○), 1000 Å (□), 400 Å (▽).

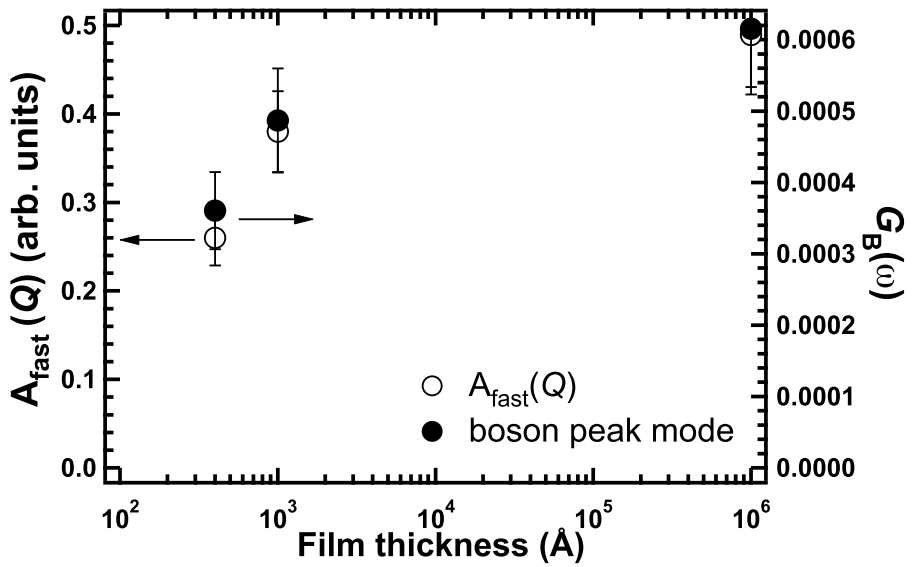

Figure 4.13: Thickness dependence of fraction of the fast process $A_{fast}(Q)$(○) and density of phonon states of the Boson peak mode $G_B(\omega)$(●).

and the fraction $A_{fast}(Q)$ are plotted against inverse of T in Figure 4-11 for the bulk and the 1000 Å and 400 Å films. The relaxation rate Γ is almost independent of temperature for the bulk and the 1000 Å and 400 Å films, showing that the activation energy of the fast process is almost zero or very small. This result implies that fast process is a localized motion within a potential well (cage motion) [16], which is also supported by the fact that the relaxation rate Γ is independent of Q [43,47] for all the samples as shown in Figure 4-12. On the other hand, the fraction $A_{fast}(Q)$ of the fast process increases with temperature, which must correspond to the increase in the amplitude of the motion because the fast process is a localized motion in a potential well. What we have to emphasize here is that the fraction $A_{fast}(Q)$ decreases with the film thickness. The film thickness dependence of $A_{fast}(Q)$ is shown in Figure 4-13 As discussed above, the Boson peak intensity $G_B(\omega)$ also decreases with the film thickness, which is indicated in Figure 4-13. The film thickness dependence is very similar between $A_{fast}(Q)$ and $G_B(\omega)$, suggesting that the two modes are caused by the same origin. In addition, both of the relaxation rate Γ of the fast process ($\sim$1 meV) and the characteristic energy of the Boson peak (the peak energy $\sim$1.5 meV) are close each other and are independent of the film thickness. This also suggests that the origin of the two modes are the same.

In the discussion on the Boson peak, we assumed that the decrease in the density of phonon states $G_B(\omega)$ was caused by the decrease of defects or voids in the hard layer at the interface. This picture would explain the decrease of the faction of the fast process $A_{fast}(Q)$ as follows. Assuming that the fast process is originated from the same defects or voids as the Boson peak, the decrease of them also induces the decrease in the fraction of the fast process. The fact that the the Boson peak energy and the relaxation rate Γ of the fast process are independent of the film thickness would predict that the defects or voids in the hard layer decreases in the number but not so different from the bulk in nature, such as the distributions of size and shape. It is therefore considered at the moment that the hard layer or the ordered layer is one of the most plausible causes for the decrease of Boson peak mode as well as the fast process.

4.4 Conclusion

In this chapter, we have studied the low energy excitations and the picosecond fast process in polystyrene thin films using inelastic and quasielastic neutron scattering in a temperature range from 11 K to 430 K, covering the bulk glass transition temperature T_g. We found in the analysis of elastic scattering that the mean square displacement $< u^2 >$ decreased with the film thickness in the whole temperature range, showing the hardening in the thinner films. In the inelastic scattering, we also found that the density of phonon states $G(\omega)$ decreased with the film thickness in both the Debye mode and the Boson peak mode although the Boson peak energy was unaltered. Furthermore, in the quasielastic scattering, the fraction of the picosecond fast process $A_{fast}(Q)$ decreased with the film thickness without changing the relaxation rate Γ. The thickness dependence of $A_{fast}(Q)$ is very similar with that of the density of phonon states of the Boson peak $G_B(\omega)$, suggesting that the Boson peak and the fast process are originated from the same molecular origin. We have examined two possibilities for the hardening: chain confinement effects in a thin film and the hard layer at the interface. Assuming that the defects or voids are the molecular origin for the both modes, the decrease in the number of the defects or voids in the hard layer without changing the nature could explain all the observations in the experiments. It is therefore concluded at the moment that the hard layer at the interface is one of the most plausible reasons for the hardening with decreasing the film thickness.

References

[1] K. Fukao, and Y. Miyamoto, Phys. Rev. E **61**, 1743 (2001).

[2] K. Fukao, and Y. Miyamoto, Phys. Rev. E **64**, 011803 (2001).

[3] R. D. Rriestly, L. J. Broadbelt, J. M. Torkelson, and K. Fukao, Phys. Rev. E **75**, 061806 (2007).

[4] J. Mattsson, J. A. Forrest, and L. Broejsson, Phys. Rev. E **62**, 5187 (2000).

[5] J. A. Forrest, K. Dalnoki-Veress, J. R. Stevens, and J. R. Dutcher, Phys. Rev. Lett. **77**, 2002 (1996).

[6] J. A. Forrest, C. Svanberg, K. Révész, M. Rodahl, L. M. Torell, and B. Kasemo, Phys. Rev. E **58**, R1226 (1998).

[7] T. Kajiyama, K. Tanaka, and A. Takahara, Polymer, **39**, 4665 (1998).

[8] T. Kajiyama, K. Tanaka, N. Satomi, and A. Takahara, Macromolecules, **31**, 5150 (1999).

[9] N. Satomi, A. Takahara, and Kajiyama, Macromolecules, **32**, 4474 (1999).

[10] N. Satomi, K. Tanaka, A. Takahara, T. Kajiyama, T. Ishizone, and S. Nakahama, Macromolecules, **34**, 8761 (2001).

[11] K. Tanaka, K. Hashimoto, T. Kajiyama, and A. Takahara, Langmuir, **19**, 6573 (2003).

[12] H. Kim, A. Rühm, L. B. Lurio, J. K. Basu, J. Lal, D. Lumma, S. G. J. Mochrie, and S. K. Sinha, Phys. Rev. Lett. **90**, 068302 (2003).

[13] Z. Jiang, H. Kim, X. Jiao, H. Lee, Y. -J. Lee, Y. Byun, S. Song, D. Eom, C. Li, M. H. Raofailovich, L. B. Lurio, A. Rühm, and S. K. Sinha, Phys. Rev. Lett. **98**, 227801 (2007).

[14] B. Frick, and D. Richter, Phys. Rev. B **47**, 14795 (1993).

[15] B. Frick, U. Buchenau, and D. Richter, Colloid Polym. Sci. **274**, 413 (1995).

[16] T. Kanaya, T. Kawaguchi, and K. Kaji, J. Chem. Phys. **104**, 3841 (1996).

[17] U. Buchenau, C. Schönfeld, D. Richter, T. Kanaya, K. Kaji, and R. Wehrmann, Phys. Rev. Lett. **73**, 2344 (1994).

[18] R. Zorn, A. Arbe, J. Colmenero, B. Frick, D. Richter, and U. Buchenau, Phys. Rev. E **52**, 781 (1995).

[19] R. Zorn, T. Kanaya, T. Kawaguchi, D. Richter, and K. Kaji, J. Chem. Phys. **105**, 1189 (1996).

[20] D. Richter, B. Frick and B. Farago, Phys. Rev. Lett. **61**, 2465 (1988).

[21] K. Inoue, T. Kanaya, S. Ikeda, K. Kaji, K. Shibata, M. Misawa, and Y. Kiyanagi, J. Chem. Phys. **95**, 5333 (1991).

[22] U. Buchenau, M. Prager, N. Nücker, A. J. Dianoux, N. Ahmad, and W. A. Phillips, Phys. Rev. B **34**, 5665 (1986).

[23] T. Kanaya, T. Kawaguchi, and K. Kaji, Macromolecules, **32**, 1672 (1999).

[24] T. Kanaya, T. Miyazaki, R. Inoue and K. Nishida, Phys. Stat. Sol. (b) **242**, 595 (2005).

[25] C. L. Soles, J. F. Douglas, W. Wu, and R. M. Dimeo, Phys. Rev. Lett. **88**, 037401 (2002).

[26] C. L. Soles, J. F. Douglas, W. Wu, H. Peng, and D. W. Gidley, Macromolecules, **37**, 2890 (2004).

[27] B. Frick, K. Dalnoki-Veress, J. A. Forrest, J. Dutcher, C. Murray, and A. Higgins, Eur. Phys. J. E **12**, s01, 93 (2003).

[28] K. Inoue, Y. Ishikawa, N. Watanabe, K. Kaji, Y. Kiyanagi, H. Iwasa and M. Kohgi, Nucl. Instr. Methods A **238**, 401 (1984).

[29] W. Marshall and S. W. Lovesey, *Theory of Thermal Neutron Scattering* (Clarendon, Oxford, 1971).

[30] C. L. Choy, R. G. Hunt, and G. L. Salinger, J. Chem. Phys. **52**, 3629 (1970).

[31] J. Brandrup, E. H. Immergut, and E. A. Grulke, *POLYMER HANDBOOK* (JOHN WILEY SONS, INC, 1998).

[32] G. B. DeMaggio, W. E. Frieze, D. W. Gidley, M. Zhu, H. A. Hristov, and A. F. Yee, Phys. Rev. Lett. **78**, 1524 (1997).

[33] R. Zorn, L. Hartmann, B. Frick, D. Richter, and F. Kremer, J. Non-Cryst. Solids. **307**, 547 (2002).

[34] R. Zorn, B. Frick, L. Hartmann, D. Richter, F. Kremer, A. Schönhals, and D. Richter, Physica B **350**, e1115 (2004).

[35] J. Schuyer, J. Polym. Sci. **36**, 475 (1959).

[36] M. K. Sanyal, J. K. Nasu, A. Datta, and S. Banerjee, Europhys. Lett. **36**, 265 (1996).

[37] J. Kraus, P. Müeller-Buschbaum, T. Kuhlmann, D. W. Schubert, and M. Stamm, Europhys. Lett. **49**, 210 (2000).

[38] M. Mukherjee, M. Bhattacharya, M. K. Sanyal, T. Geue, J. Grenzer, and U. Pietsch, Phys. Rev. E **66**, 061801 (2002).

[39] T. Nakayama, Phys. Rev. Lett. **80**, 1244 (1998).

[40] Y. Inamura, M. Arai, M. Nakamura, T. Otomo, N. Kitamura, S. M. Bennington, A. C. Hannon , and U. Buchenau, J. Non-Cryst. Solids. **293**, 389 (2001).

[41] S. P. Das, Phys. Rev. E **59**, 3870 (1999).

[42] A. V. Granato, Physica B **220**, 270 (1996).

[43] O. Yamamuro, Y. Madokoro, H. Yamasaki, T. Matsuo, I. Tsukushi and K. Takeda, J. Chem. Phys. **115**, 9808 (2001).

[44] V. Lupascu, H. Huth, C. Schick, and M. Wübbenhorst, Thermochimica Acta, **432**, 222 (2005).

[45] T. Kanaya, K. Kaji, and K. Inoue, Physica B **180**, 814 (1992).

[46] T. Kanaya, T. Kawaguchi, and K. Kaji, J. Chem. Phys. **105**, 4342 (1996).

[47] T. Kanaya, T. Kawaguchi, and K. Kaji, J. Chem. Phys. **98**, 8262 (1993).

Chapter 5

Molecular Weight Dependence of Mean Square Displacement in Polystyrene Thin Films

5.1 Introduction

We studied the glassy dynamics of polymer thin films with inelastic neutron scattering to observe the decrease of mean square displacement $< u^2 >$ as well as the inelastic and quasielastic neutron scattering intensity with film thickness in Chapter 4. We considered two main possibilities for the decrease of $< u^2 >$ with film thickness. One is the hardening of polymer chains due to the spatial confinement (confinement effect) as was shown in Figure 4-6(a). When the film thickness decreased in in a size less than the polymer chain coil size that is characterized by twice radius of gyration ($2R_g$), polymer chains cannot sustain the normal coil form and the deformation of polymer chains would occur. Under this condition, the deformed polymer chains would have higher restoring force than the normal coil, resulting in the decrease of mobility. The decrease of mobility ($=< u^2 >$) was observed even for 1000 Å thin film, which is much larger than $2R_g$ in bulk. In order to understand this phenomenon, we assumed that the hard layer (lower mobility layer) would exist at the interface between the polymer thin film and the substrate. With decreasing the film thickness, the fraction of such a hard layer becomes large under the assumption that the thickness of the hard layer is independent of the total film thickness. This is another possibility (interface effect) as was shown in Figure 4-6(b). Except the two possibilities we considered other minor

possible reasons for the decrease of $< u^2 >$. One is the end group effect. According to the experiment by Satomi et al. [1], it was negligible for M_w above 10^5 but not for M_w below 10^5. The other is the surface roughness of polymer thin films. Miyazaki et al. investigated the surface roughness of PS thin films for different M_w by X-ray reflectivity (XR) in a wide thickness range [2], however the observed roughness was less than 7 Å and not dependent on thickness or M_w. Therefore, this is negligible either.

In the former chapter, we concluded that the interface effect was the candidate for the decrease of $< u^2 >$ with film thickness. However, it was not enough for the final conclusion. In order to settle this problem, we prepared thin films with same film thickness for different molecular weights (M_w), giving different ratios of the film thickness ($=d$) to the twice radius of gyration ($2R_g$). If the confinement effect were dominant, the decrease of $< u^2 >$ would be observed with the decrease of ratio of $d/2R_g$ because decreasing the ratio $d/2R_g$ means the increase of spatial confinement. And if the interface effect were dominant, $< u^2 >$ would be constant regardless of the ratio $d/2R_g$ because the ratio is constant under the same film thickness. Conducting the experiment of M_w effect, we can understand which factor is responsible for the decrease of $< u^2 >$ with film thickness.

5.2 Experimental

We used three amorphous polystyrenes (PS) with different molecular weights (M_w) 2.90×10^5, 1.05×10^6 and 1.88×10^6 and the molecular weight distributions (M_w/M_n) 1.06, 1.07 and 1.13, respectively, where M_w and M_n are the weight-average and the number-average of the molecular weight, respectively, and calculated values of R_g are 147, 280 and 374 Å for $M_w = 2.90\times10^5$, 1.05×10^6 and 1.88×10^6, respectively, under the unperturbed chain approximation [3]. The detail of preparation of thin films was already described in Chapter 4 and we prepared films 400 Å in thickness for three different M_w's and this film thickness is less than the size of $2R_g$ for M_w=1.05×10^6 and 1.88×10^6. The annealing condition was already described in Chapter 4. 300 sheets of the films on Al foils were rolled up and placed into a hollow cylindrical Al cell 14

mm in diameter and 45 mm high and inelastic neutron scattering measurements were performed with an inverted geometry time-of-flight (TOF) spectrometer LAM-40 and the energy resolution was about 0.20 meV the elastic position on the energy gain side. The measurements were carried out at temperatures from 11 K to 300 K that is far below the bulk glass transition temperature T_g (=373 K), meaning that we mainly focused on the glassy state.

5.3 Results and Discussion

The mean square displacement $< u^2 >$ can be evaluated from the Q^2 dependence of elastic intensity $I_{el}(Q)$ using the equation $I_{el}(Q) \sim \exp[- < u^2 > Q^2]$. The mean square displacement $< u^2 >$ decreases with film thickness for the PS films with M_w=2.90×10^5 and the thickness dependence was well described by the following equation.

$$< u^2 >=< u^2 >_{bulk} \left[1 - \left(\frac{d_0}{d}\right)^{\delta}\right], \tag{5.1}$$

where $< u^2 >_{bulk}$, d, d_0, δ are mean square displacement of bulk, film thickness, constant, exponent, respectively. Although we have no theoretical basis for this equation, we used it in analogy with the thickness dependence of T_g suggested by Keddie et al. [4]. In this chapter we studied $< u^2 >$ for the film thickness of 400 Å as a function of molecular weight M_w. First we focus on the temperature dependence of elastic intensity for three different molecular weights. Figure 5-1 indicates the temperature dependence of elastic intensity normalized to that of the lowest temperature (=11 K) for M_w=2.90×10^5, 1.05×10^6 and 1.88×10^6 at Q=2.20 Å^{-1} and the error bars were evaluated from the raw counts of TOF spectrum at each temperature. The logarithm of the normalized elastic intensity decreases almost linearly with temperature as shown by solid lines in Figure 5-1 in the low temperature range, indicating that the vibrational motion is harmonic. In the case of bulk PS, onset of fast process is observed at around 200 K, leading to the deviation from the harmonic behavior [5,6]. However, the onset temperature of the fast process increases (260 K for the 400 Å film) and the obtained spectrum were well scaled by Bose population factor at 230 K for 400 Å thin films, as

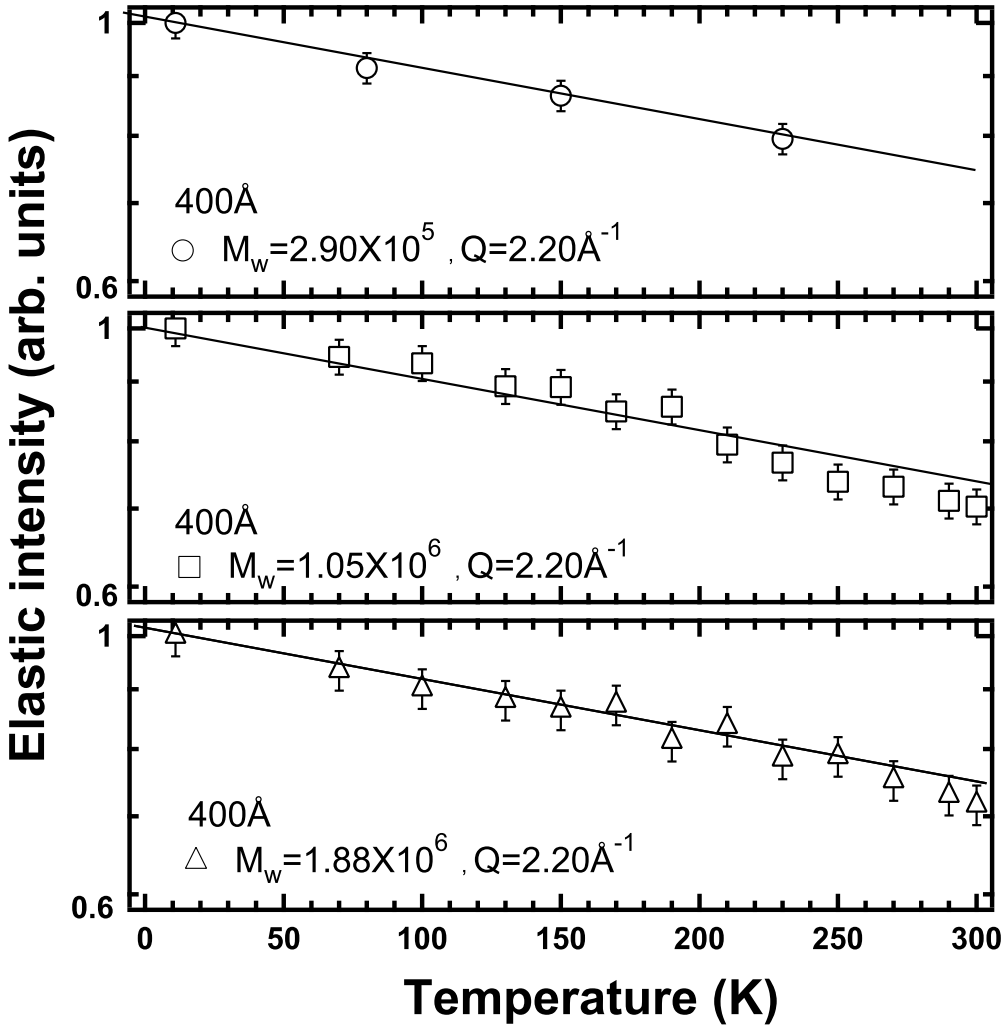

Figure 5.1: Temperature dependence of elastic scattering intensity divided by that of the lowest temperature 11 K for $M_w = 2.90\times10^5$ (○), 1.05×10^6(□) and 1.88×10^6 (△) at Q=2.20 Å^{-1}.

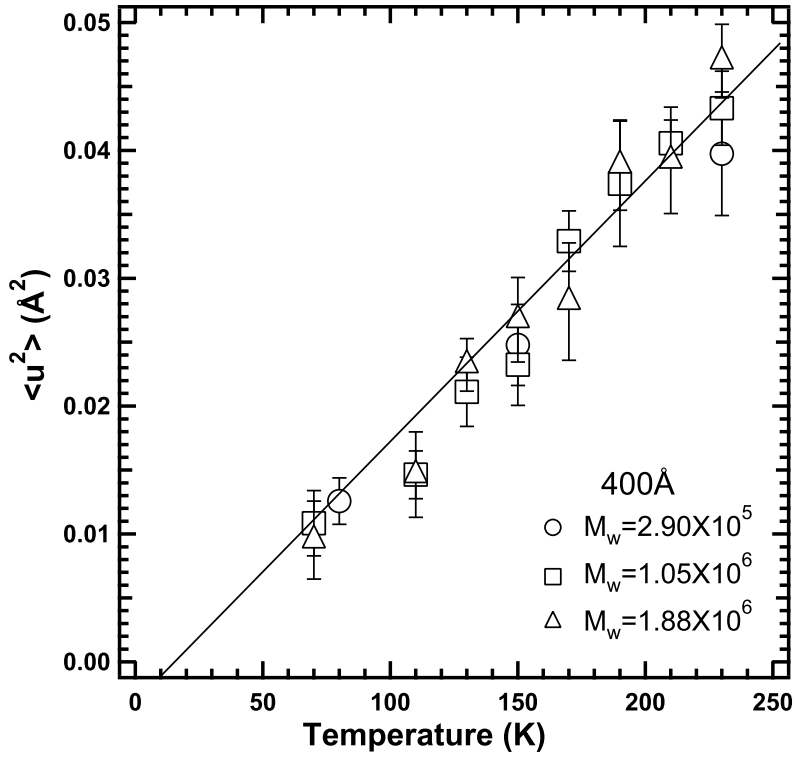

Figure 5.2: Temperature dependence of mean square displacement $< u^2 >$ for $M_w = 2.90\times10^5$ (○), 1.05×10^6(□) and 1.88×10^6 (△).

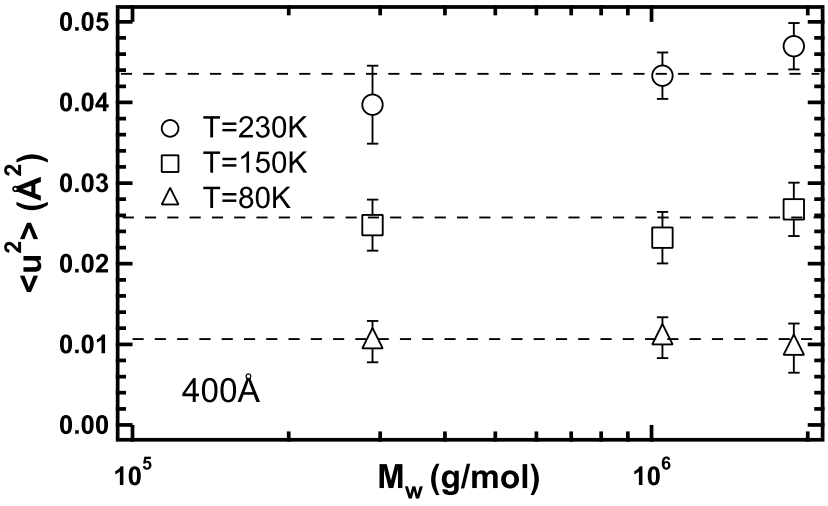

Figure 5.3: M_w dependence of mean square displacement $< u^2 >$ at 80 K(△), 150 K (□) and 230 K (○) for 400 Å thin films and dotted line was drawn by eye.

shown in Figure 4-8. Thus, the fast process is suppressed and hard to observe as the film thickness decreases. Even if the fast process observed at 230 K, the effect on $< u^2 >$ is so small that the discussions in this chapter are not affected. Therefore, we don't go into the detail about the fast process in this chapter and focused on the vibrational behavior under the harmonic approximation (T<260 K). The temperature dependence of elastic intensity for 3 different M_w's was almost the same within the experimental error. We also evaluated temperature dependence of $< u^2 >$ and show the results in Figure 5-2 for 3 different M_w's. The error bars in Figure 5-2 were estimated from the uncertainties of the fit. $< u^2 >$ is almost proportional to T as shown in Figure 5-2, indicating again that the motion is harmonic. Evaluated values of $< u^2 >$ for different M_w's lie on a straight line within the experimental error. It was found that $< u^2 >$ in the 400 Å film is independent of M_w in the temperature range examined. To confirm this, $< u^2 >$ values for 400 Å thin films are plotted as a function of M_w at some temperatures in Figure 5-3. If the confinement effects were dominant, a decrease of $< u^2 >$ would be observed with increasing M_w because higher M_w is more spatially confined than lower M_w under the same film thickness. It was therefore concluded that the confinement effect was not the main reason for the decrease of mobility with film thickness.

Unfortunately we have to admit that the experimental error is not so small because of the very weak scattering intensity from the thin films in the present measurement. If the molecular weight M_w dependence of $< u^2 >$ due to the confinement effect is within the error, we could not conclude that the decrease of $< u^2 >$ was caused by the interface layer and we have to deny the possibility of confinement effect. Unfortunately we have to admit that the experimental error is not so small because of the very weak scattering intensity from the thin films in the present measurement. If the M_w dependence of $< u^2 >$ were so small that it falls within the error bounds, we could not conclude that the decrease of $< u^2 >$ is caused by the interface layer. To check it, we plotted $< u^2 >$ as a function of the ratio of film thickness to twice of radius of gyration ($d/2R_g$) in Figure 5-4(a), which can be regarded as a measure of the deformation of polymer coils

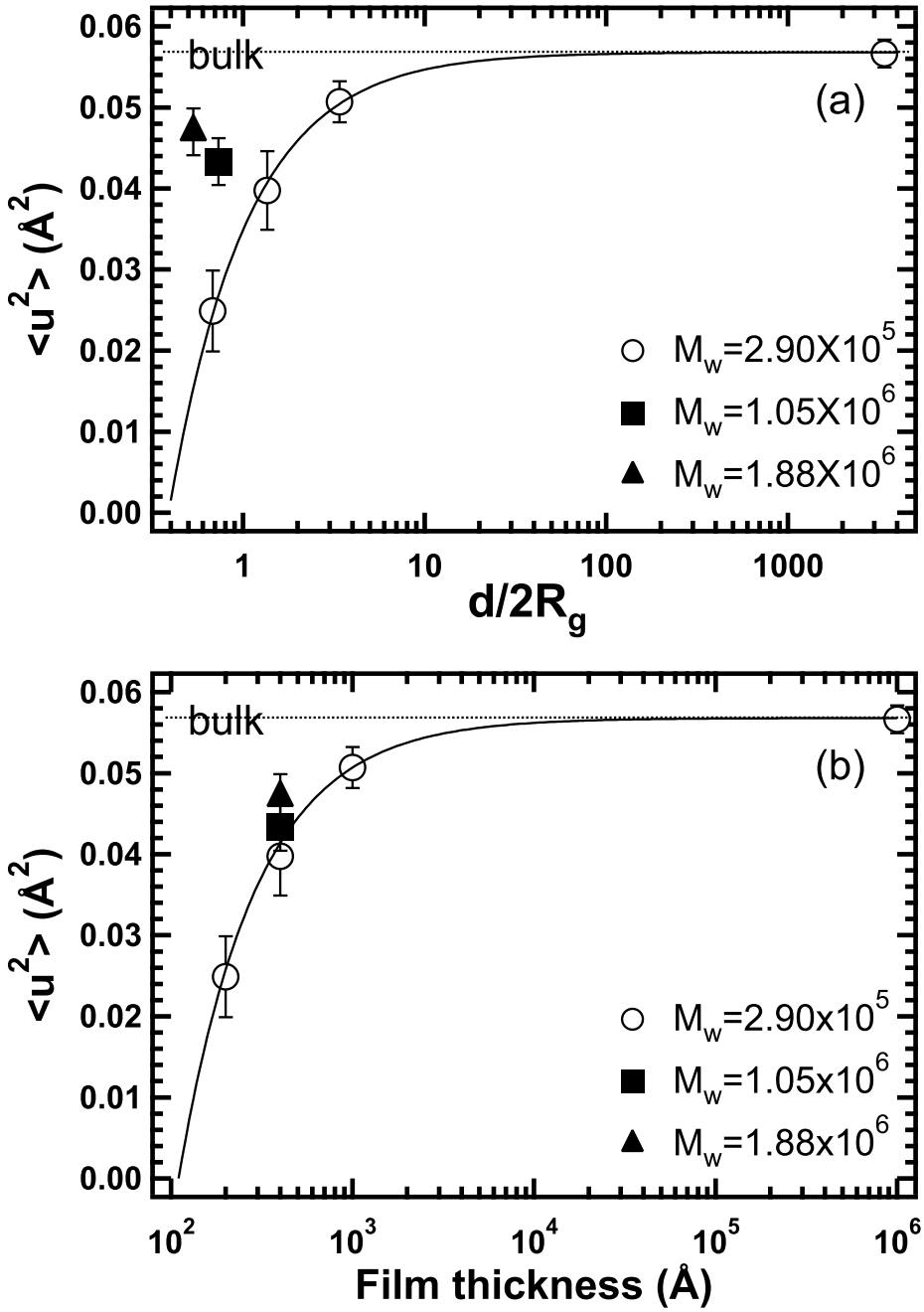

Figure 5.4: (a) Mean square displacement $< u^2 >$ as a function of ration of film thickness to twice radius of gyration ($d/2R_g$) at 230 K for $M_w = 2.90\times10^5$ (○), 1.05×10^6 (■) and 1.88×10^6 (▲). (b) Mean square displacement $< u^2 >$ as a function of film thickness (d) at 230 K for $M_w = 2.90\times10^5$ (○), 1.05×10^6 (■) and 1.88×10^6 (▲). And solid lines are results of fit with (5.1).

[7]. In the figure $< u^2 >$'s for different film thicknesses from Chapter 4 and Chapter 6 are included. We also plotted the same data as a function of the film thickness d for different molecular weight M_w in Figure 5-4(b). It is very clear that the $< u^2 >$ is scaled by d, not $d/2R_g$ within the accuracy in the measurements. This directly suggests that the $< u^2 >$ is not dominated by the deformation of polystyrene coils. It is concluded that the main reason for the decrease of $< u^2 >$ with film thickness is not the confinement of polymer coils but the interface hard layer.

Zhang et al. [8] revealed orientation of molecular chain axis of poly(methyl methacrylate) at the interface using reflection-absorption infrared (RAIR) and surface-enhanced Raman scattering (SERS). Especially in the case of PS, phenyl rings tend to orient parallel to the interface between PS and substrate, revealed by IR-visible sum-frequency generation (SFG) spectroscopy [9]. Such orientation or ordering at the interface between polymer and substrate may be related to the hard layer so-called "dead layer". As the result of orientation or ordering at the interface, the mobility would be smaller than that in bulk due to the high contribution from the hard layer.

5.4 Conclusion

We have investigated the effect of molecular weight (M_w) on mean square displacement $< u^2 >$ in order to disclose the origin of decrease of $< u^2 >$ with film thickness. Observed $< u^2 >$ values are independent of the molecular weight M_w within the experimental error, and the molecular weight dependence of $< u^2 >$ expected from the confinement effect could not describe the observed reduction of $< u^2 >$ well, even though experimental errors were considered. It was therefore concluded that the decrease of $< u^2 >$ with film thickness was caused by the interface hard layer.

References

[1] N. Satomi, K. Tanaka, A. Takahara, T. Kajiyama, T. Ishizone, and S. Nakahama, Macromolecules, **34**, 8761 (2001).

[2] T. Miyazaki, K. Nishida, and T. Kanaya, Phys. Rev. E **69**, 061803 (2004).

[3] J. Brandrup, E. H. Immergut, and E. A. Grulke, *POLYMER HANDBOOK* (JOHN WILEY SONS, INC, 1998).

[4] J. L. Keddie, R. A. L. Jones, and R. A. Cory, Europhys. Lett. **27**, 59 (1994).

[5] B. Frick, U. Buchenau, and D. Richter, J. Colloid Polym Sci. **274**, 413 (1995).

[6] T. Kanaya, T. Kawaguchi and K. Kaji, J. Chem. Phys. **104**, 3841 (1996).

[7] K. Shuto, Y. Oishi, T. Kajiyama, and C. C. Han, Macromolecules, **26**, 6589 (1993).

[8] J. M. Zhang, D. H. Zhang, and D. Y. Shen, Macromolecules, **35**, 5140 (2002).

[9] K. S. Gautam, A. D. Schwab, A. Dhinojwala, D. Zhang, S. M. Dougal, and M. S. Yeganeh, Phys. Rev. Lett. **85**, 3854 (2000).

Chapter 6

Dynamic Anisotropy and Heterogeneity of Polystyrene Thin Films

6.1 Introduction

The decrease in T_g with film thickness is often discussed in terms of a mobile layer at the free surface, which was directly confirmed by atomic force microscopy (AFM) measurements [1,2] and the decrease in thermal expansivity with film thickness [3-6], which is often discussed in terms of three layer model consisting of a surface layer, a bulk-like layer and an interface hard layer. The idea of two-layer and/or three-layer model is supposed to be a candidate for understanding the structure of polymer thin film. More generally, multi-layer structure with different T_g in a polymer thin film has been proposed and experimentally examined by Torkelson et al. [7,8] using fluorescence/multilayer method.

We found that the decrease of the mean square displacement $< u^2 >$ with film thickness was caused by the hard layer at the interface as shown in Chapter 4, 5. This result suggests anisotropic and heterogeneous structure of polymer thin films. We believe that one of the most important keys to solve the unusual properties of polymer thin films is heterogeneous structure or multi-layer structure. We propose to study the heterogeneity of polymer thin films in terms of non-Gaussian parameter A_0, which can be evaluated using a neutron spectrometer that is accessible to high Q region [9,10]. In addition, we also studied the dynamic anisotropy of polymer thin films. It is expected

that the hard layer has ordered structure of polystyrene, exhibiting layering [11]. If the picture is correct we expect that the dynamic anisotropy would be observed in a very thin film having a total thickness comparable with the hard layer. As far as we know, there are no experimental reports on the dynamic anisotropy of polymer thin films in the glassy state although a molecular dynamics (MD) simulation has been done on polymer thin films in melt to see the dynamic anisotropy in a time scale of diffusion [12]. In this Chapter we have studied anisotropic motions in polystyrene thin films in the glassy state in meV region by measuring the thin films in transmission and reflection geometries. In the former and the latter we can set scattering vector Q parallel and perpendicular to the film surface for the elastic scattering at scattering angle of 90°.

6.2 Experimental

The sample used for the scattering experiments was amorphous polystyrene (PS) with molecular weight M_w= 2.90×10^5 and molecular weight distribution M_w/M_n=1.06, where M_w and M_n are the weight-average and the number-average of the molecular weight, respectively. This polymer is the same as in the previous chapters. The detail of sample preparation was written in Chapter 4 and we prepared films 1000 Å and 200 Å thick in this chapter. 300 sheets of the films on Al foils were placed into a cylindrical Al cell 42.1 mm in diameter and 66.5 mm high to keep two scattering geometries; transmission and reflection geometries. In the former and the latter the scattering vector Q is almost parallel and perpendicular to the film surface, respectively, and hence we can observe the molecular motion parallel and perpendicular to the surface direction as was shown in Figure 6-1. In the present experiments, the film surface was set at ±45° to the incident neutron beam, therefore exact parallel and perpendicular geometries are hold at Q = 3.8 Å^{-1} for the elastic scattering. We used 300 sheets for both 1000 and 200 Å films, and the total thickness is different between them.

Elastic and inelastic neutron scattering measurements were performed on a direct geometry spectrometer MARI installed at the pulsed neutron source in ISIS, Rutherford

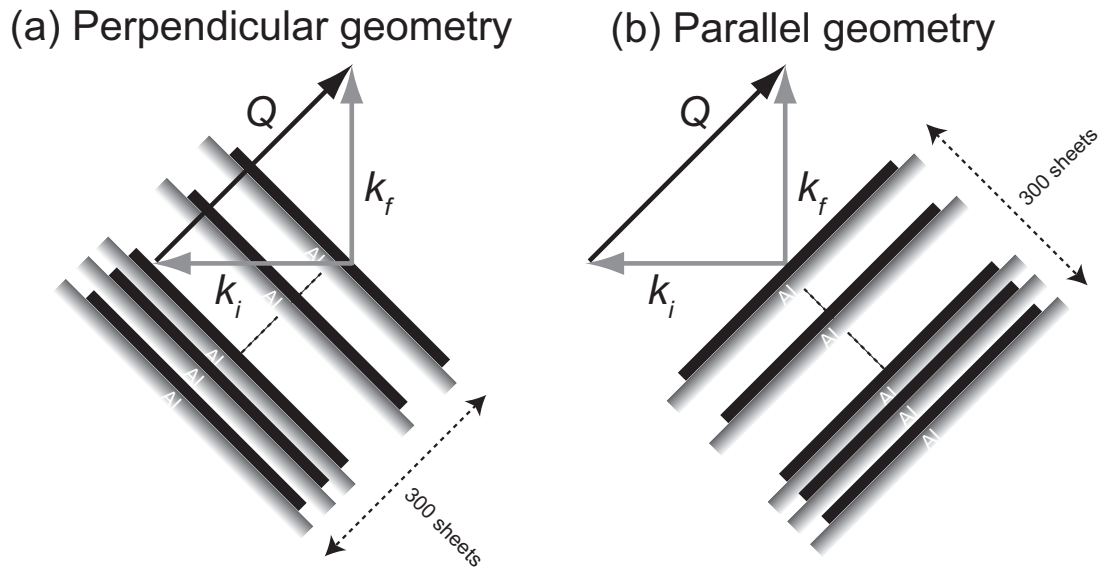

Figure 6.1: Sample geometry for MARI measurements. (a) Perpendicular and (b) Parallel geometry. The figure corresponds to the case of elastic scattering ($\boldsymbol{k_i} = \boldsymbol{k_f}$).

Appleton Laboratory, Didcot. In the present measurements, we have selected an incident energy to achieve a high-energy resolution δE of 0.34 meV, which was evaluated from the half-width at the half-maximum of elastic scattering on the energy gain side. The neutron detector banks of the MARI spectrometer are spread from 3 to 134° with 1000 detectors, so that a very wide and continuous range of Q is covered. Under the present experimental condition, the Q range was from 0.2 to 5 Å^{-1}, which is extremely wide compared with a conventional time-of-flight (TOF) spectrometer at a cold neutron source [13-15]. This wide Q range is a distinct feature of this experiment.

6.3 Results and Discussion

Figure 6-2 indicates the observed dynamic scattering law $S(Q, \omega)$ for the 1000 Å and 200 Å thin films at $Q = 3.8$ Å^{-1} in the parallel and perpendicular geometries at various temperatures. Apparently the inelastic and quasielastic intensities hardly depend on temperature even above the glass transition temperature (408 K), but it is due to the large Debye-Waller factor. The inelastic scattering spectra were well Bose-scaled for both the scattering geometries after correcting the Debye-Waller factor, as shown in In Figure 6-3. The excess intensity over the Bose-scaled spectrum at a high temperature above T_g (408 K) was observed for 1000 Å due to the onset of fast process, which was also observed in chapter 4. However, the fast process was hard to be seen for 200 Å thin films because of the large statistical error. The decrease of fraction or intensity of the fast process with film thickness might be related to above results, as was already discussed in chapter 4.

First we paid our attention on the temperature dependence of the incoherent elastic scattering intensity $I_{el}(Q)$ in order to examine the dynamic anisotropy of the thin films. We plotted the elastic scattering intensities $I_{el}(Q)$ from the 200 and 1000 Å films in Figure 6-4 against temperature for the two scattering geometries at $Q = 3.8$ Å^{-1}, which satisfies the exact parallel and perpendicular geometries. The elastic intensities were normalized to that at the lowest temperature (∼5 K). In case of the 1000 Å film no differences in the temperature dependence were observed in the parallel and

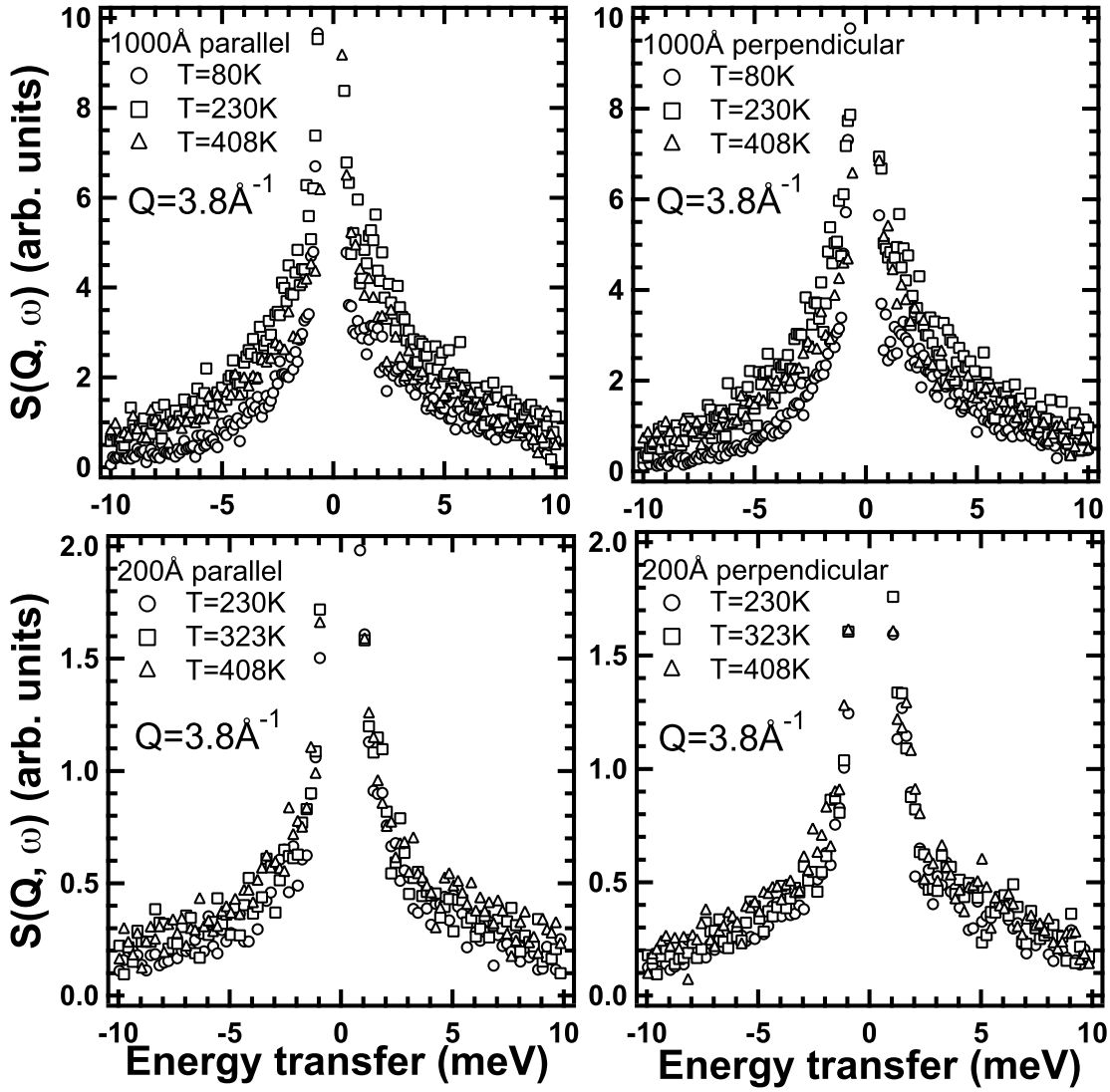

Figure 6.2: Dynamic scattering law $S(Q, \omega)$ of 1000 and 200 Å PS thin films at various temperatures at Q=3.8 Å^{-1} in perpendicular and parallel geometries.

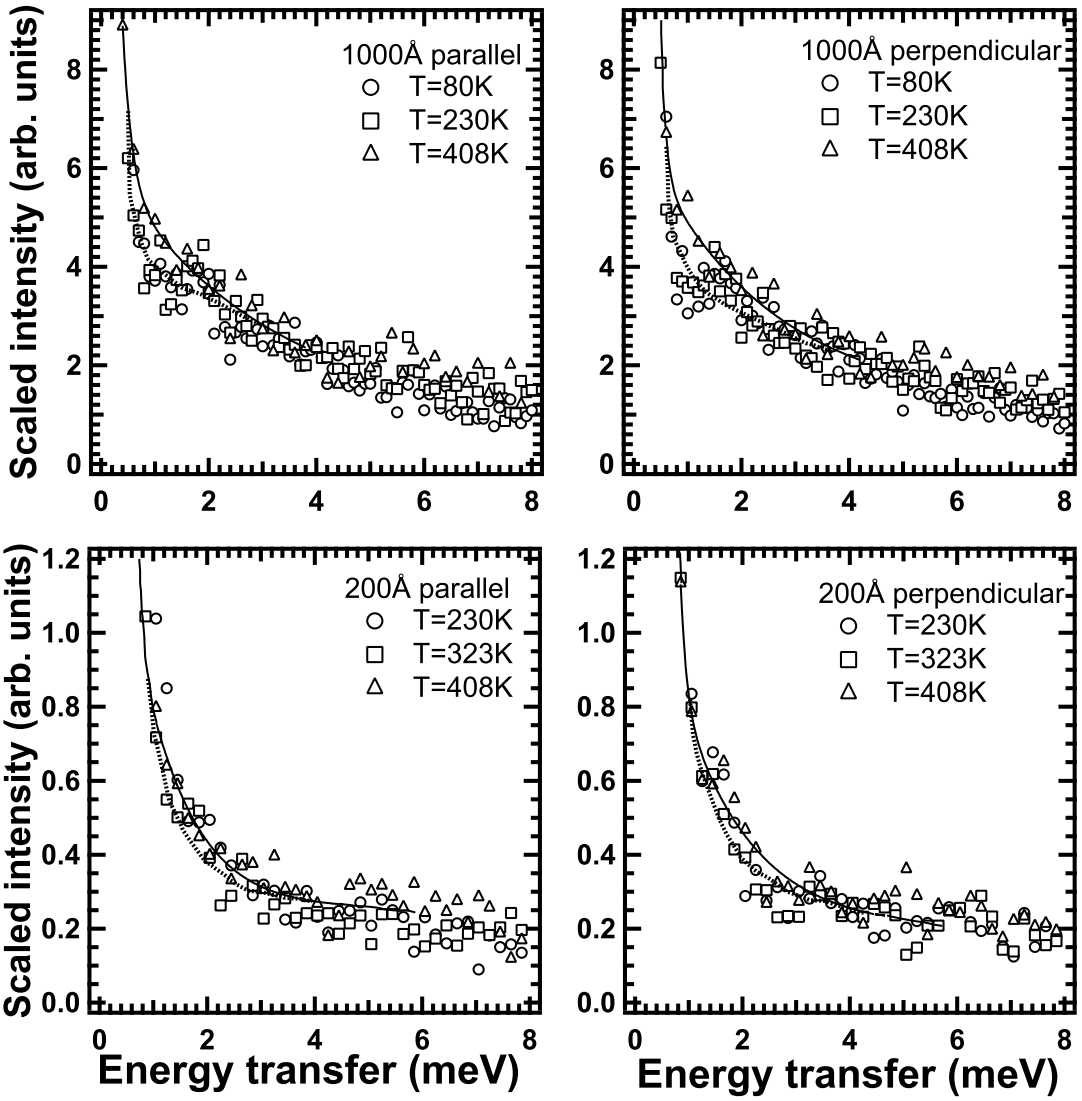

Figure 6.3: Bose-scaled dynamic scattering law $S(Q, \omega)$ of 1000 and 200 Å PS thin films at various temperatures at Q=3.8 Å^{-1} in perpendicular and parallel geometries after correcting for Debye-Waller factor. Solid lines were drawn by eye for the spectra at 408 K for both 1000 and 200 Å films. Dashed lines were also drawn by eye for the spectra at 80 K for 1000 Å film and at 230 K for 200 Å film in the low energy region below 2 meV

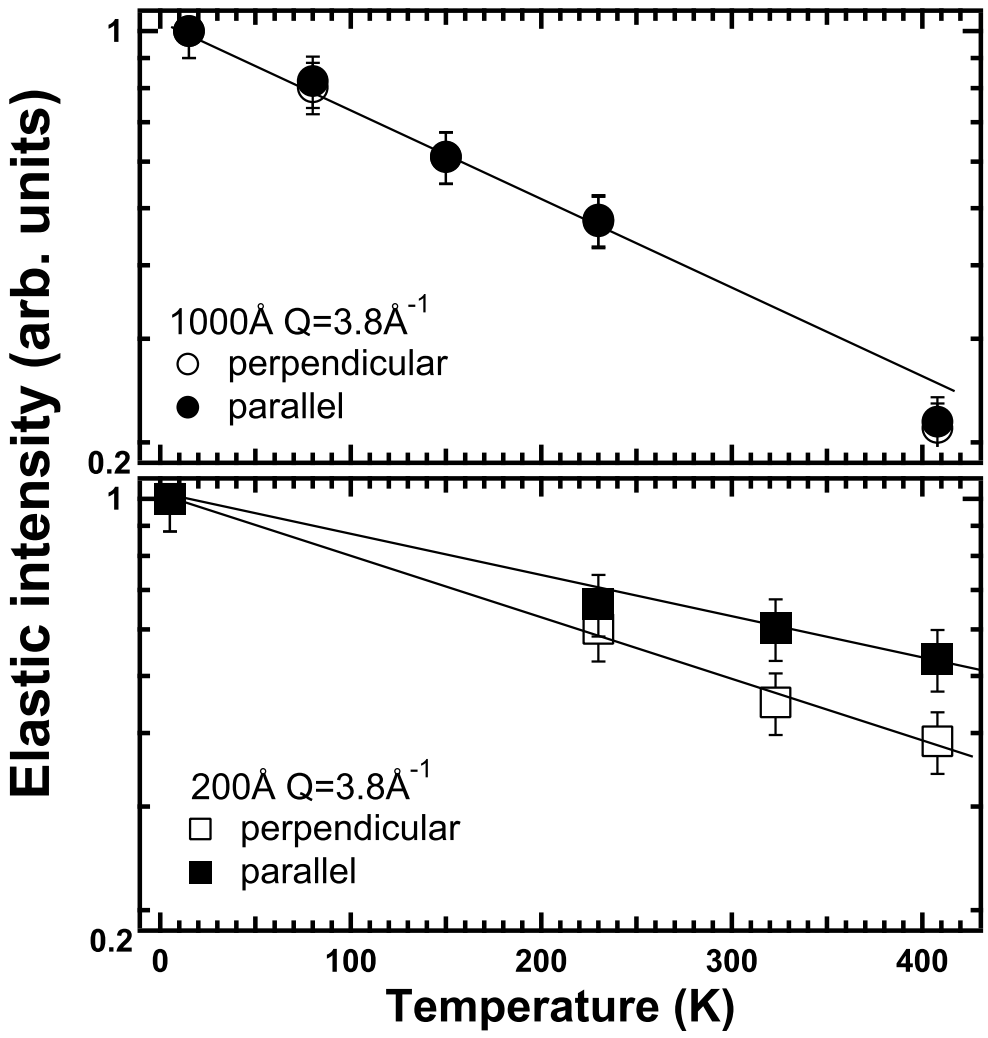

Figure 6.4: Temperature dependence of elastic intensity $I_{el}(Q)$ at Q=3.8 Å^{-1} for 1000 Å and 200 Å thin films in parallel (•, ■) and perpendicular (∘, □) geometries. Solid lines are guided by eye.

perpendicular geometries, showing that the dynamic anisotropy is negligible. On the other hand, the elastic scattering intensity of the 200 Å film in the perpendicular geometry decreases with temperature more steeply than in the parallel geometry, suggesting that molecules (or segments) are more mobile in the perpendicular direction than in the parallel one although the difference is not so large (about 20% difference at 408 K). We also found that the temperature dependence of the elastic scattering intensity $I_{el}(Q)$ for the 200 Å thin film was smaller than that for the 1000 Å thin film in both the geometries, indicating the decrease in mobility with the film thickness. In Chapters 4 and 5, we found that the mean square displacement $< u^2 >$ for isotropic polystyrene thin films decreased with film thickness, showing the potential hardening with film thickness. The present observation corresponds to the decrease in the mean square displacement $< u^2 >$ with film thickness. We also discussed the cause of the hardening in the chapter 4,5 to conclude that it is not due to the confinement effect of polymer chains but a hard layer at the interface between the polymer thin film and the substrate. The thickness of the hard layer was estimated to be ∼110 Å which is in a range of the reported values although they are rather scattered [3, 16, 17]. The interface hard layer is supposed to be a candidate for the dynamic anisotropy in the 200 Å film. It was reported that polymer chains tend to form ordered structure or layering at the interface [18,19], and Zhang et al. [20] revealed orientation of molecular chain axis of poly(methyl methacrylate) at the interface using reflection-absorption infrared (RAIR) and surface-enhanced Raman scattering (SERS). In case of PS, IR-visible sum-frequency generation (SFG) spectroscopy [21] has shown that phenyl rings orient parallel to the surface near the interface. Torsional motion of oriented phenyl rings to the surface have larger amplitude of motion in the perpendicular direction than in the parallel one, agreeing with the present observation in the 200 Å film. For the 1000 Å thin film, on the other hand, the hard layer is only ∼10% in the total thickness and 90% must be isotropic bulk-like layer. In this situation the bulk contribution is much larger than that of the hard layer, and hence the dynamical anisotropy was not observed for the 1000 Å film. We now consider the inelastic and quasielastic

scattering, which is a counter part of the elastic scattering. In the spectra of the 200 and 1000 Å films in Figure 6-3 the boson peak is hardly recognized even in the spectra at 80 K although it was seen in the previous measurements by LAM-40 with energy resolution of $\delta E = 0.20$ meV. This is not surprising because a rather long tail of the energy resolution function of MARI ($\delta E = 0.34$ meV) hides the boson peak which lies at around 1.5 meV in PS. However, we can recognize the excess scattering over the Bose-scaled spectrum, which corresponds to the so-called picosecond fast process, in a low energy region below about 2 meV in a high temperature region above about 200 K. This is demonstrated in the Bose-scaled spectra after correcting the Debye-Waller factor in Figure 6-3.

In order to study the characteristic features of the fast process, the observed dynamic scattering law $S(Q, \omega)$ at the highest temperature (= 408 K) were fitted to a model function convoluted with the resolution function of the spectrometer. We employed the same model function, which was used for the fitting of quasielastic scattering obtained with LAM-40 (Chapter 4). The results of the fits for the 1000 Å and 200 Å films at 408K for the two geometries at Q=3.8 Å^{-1} are shown Figure 6-5. Although the fitness is not bad the statistical error in the data is rather large, and hence we have to admit the results of fits include large error. The evaluated half-width at half-maximum Γ, which corresponds to the relaxation rate, and the fraction of the fast process $A_{fast}(Q)$ were shown in Figure 6-6 as a function of film thickness for the parallel and perpendicular geometries. The relaxation rates Γ are at around 1meV regardless the film thickness while the fraction of the fast process decreases with the film thickness. These results agree with the previous experiments for 1000 Å and 400 Å thin films, as shown in Figure 4-11 and we again confirm that the fraction of the fast process decreases with the film thickness. On the other hand, the differences of Γ and $A_{fast}(Q)$ between the two scattering geometries could not be observed for the 1000 Å film. As for the 200 Å film, $A_{fast}(Q)$ in the perpendicular direction is larger than the parallel direction by ∼20 %. This qualitatively corresponds to the elastic scattering results (see Figure 6-3), but it is hard to discuss this difference because of the large

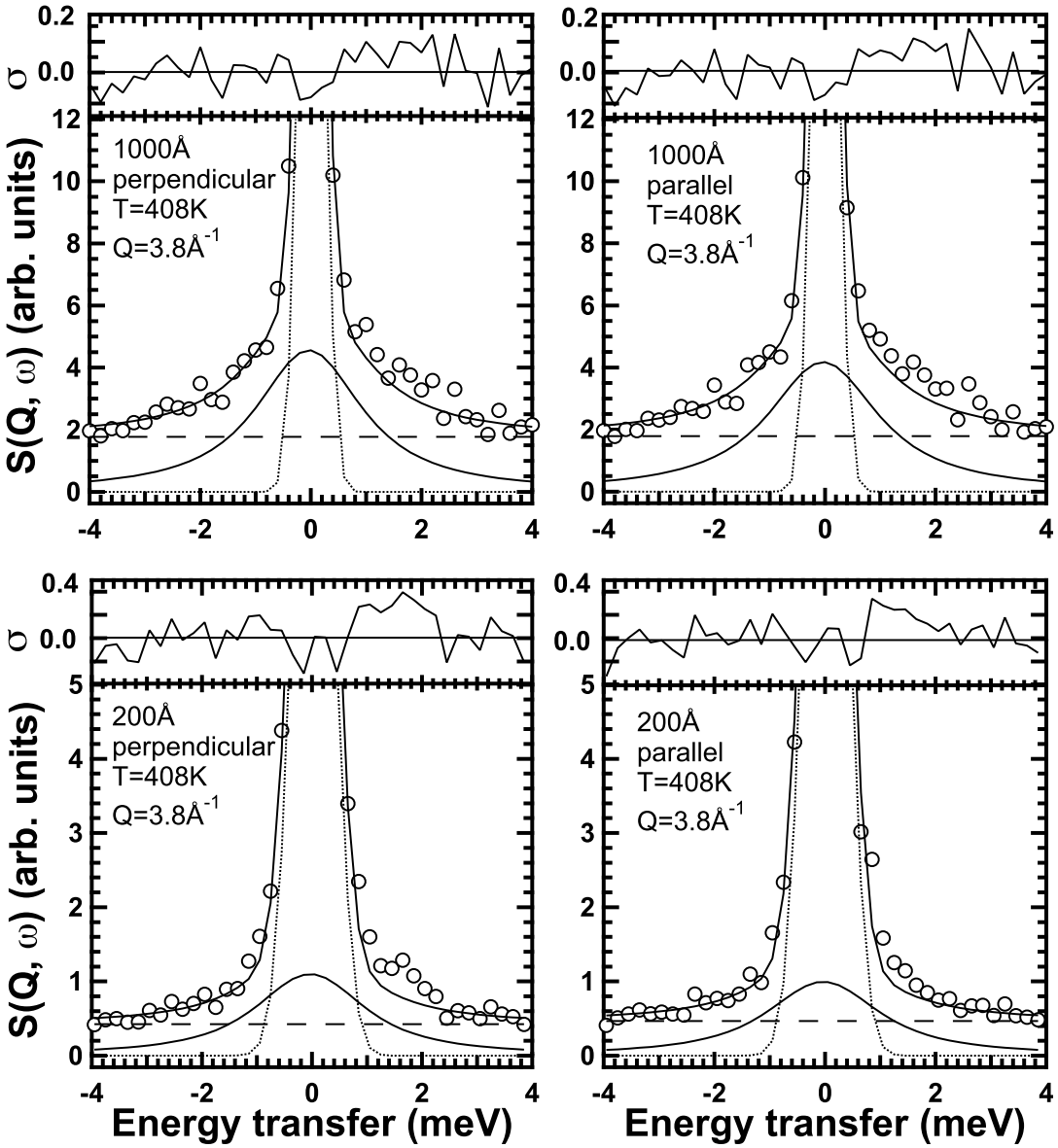

Figure 6.5: Results of curve fits to $S(Q, \omega)$ of 1000 and 200 Å PS thin films at 408 K at Q=3.8 Å^{-1} for parallel and perpendicular geometries. ($\cdots$): elastic component, (—): quasielastic Lorentzian and (- - -): flat background.

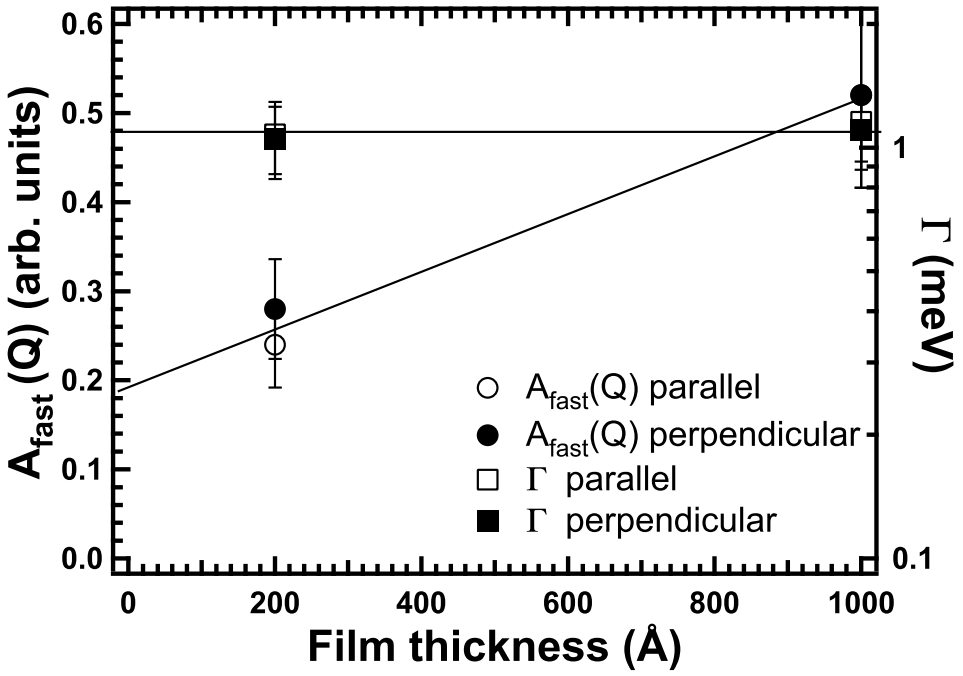

Figure 6.6: Film thickness dependence of relaxation rate Γ and fraction $A_{fast}(Q)$ of the fast process at 408 K for parallel and perpendicular geometries. Parallel ($\circ$, $\square$) and perpendicular ($\bullet$, $\blacksquare$). Square and circle symbols correspond to Γ and $A_{fast}(Q)$, respectively.

statistical error in the quasielastic scattering spectra.

Next, we examined the Q dependence of the incoherent elastic scattering intensity $I_{el}(Q)$ in order to evaluate the mean square displacement $< u^2 >$ as well as the dynamic heterogeneity in the thin films. Figure 6-7 indicates the Q^2 dependence of elastic scattering intensities $I_{el}(Q)$ for the 1000 Å and 200 Å films in the transmission and reflection geometries at 230K which were divided by $I_{el}(Q)$ at the lowest temperature (= 5 K) in order to reduce the contribution from the coherent scattering. It is well know that the Q dependence of incoherent elastic scattering under the Gaussian approximation is described by

$$I_{el}(Q,t) = \exp(-\alpha Q^2), \tag{6.1}$$

where $\alpha = < u^2 >$. As seen in Figure 6-7 it is obvious that $I_{el}(Q)$ cannot be described within the Gaussian approximation, deviating in a high Q region above about 2.5 Å^{-1}. This must be due to higher order terms of Q. In order to describe the Q dependence of $I_{el}(Q)$ we have to take into account higher order terms of Q, including non-Gaussian parameter A_0. The non-Gaussian parameter was first introduced by Rhaman et al. [22]. According to them, the incoherent intermediate scattering function $I(Q,\ t)$ is obtained from the cumulant expansion up to the order of Q^4 as follows

$$I(Q,t) = \exp\Big(-\frac{< \Delta r^2 > (t)}{6}Q^2 + \frac{A_0(t)[< \Delta r^2 > (t)]^2}{72}Q^4\Big). \tag{6.2}$$

In this expression, the integrals of the velocity correlation functions, denoted by $\gamma_1(t)$ and $\gamma_2(t)$ in ref. [22], have been expressed in terms of the mean square displacement $< \Delta r^2 > (= 6< u^2 >)$. The non-Gaussian parameter $A_0(t)$ is given by an expression

$$A_0(t) = \frac{3 < \Delta r^4 > (t)}{5[< \Delta r^2 > (t)]^2} - 1. \tag{6.3}$$

In the Gaussian approximation, the intermediate scattering function is given in the form up to the order of Q^2. This approximation perfectly holds for harmonic oscillators, perfect gases and diffusion processes at infinite time though it is valid only for a low Q range in real systems. In a high Q range, we have to take into accounts the non-Gaussianity. It has been shown by Zorn [23] that the non-Gaussian parameter

could be due to different phenomena such as dynamic heterogeneity, anharmonicity and dynamical anisotropy. In glass-forming materials the most plausible origin of non-Gaussian parameter A_0 was attributed to dynamical heterogeneity due to the difference of local environments using several polymeric glass-formers [24-26]. In case of polymer thin films in the glassy state the dynamic heterogeneity must be a leading term in the non-Gaussian parameter. In addition, we have to consider the heterogeneity due to multi-layer structure (or heterogeneous layer structure) in the thin films. However, contributions to the non-Gaussian parameter from other factors such as anharmonisity and dynamic anisotropy seem very small in the PS thin films. Almost linear relationship between the mean square displacement and temperature in the thin films up to 230 K supports that the anhamonisity effect on the non-Gaussian parameter is negligible. As shown in Figure 6-4, we observed the small dynamic anisotropy in the 200 Å film. This effect is not large even in the unoriented bulk sample. We now measure the oriented samples, and hence the effect is negligible. Therefore, we analyze the Q dependence of the incoherent elastic scattering intensity assuming that the non-Gaussian parameter in the thin films arises from the dynamic heterogeneity intrinsic to bulk glassy state and the multi-layer structure.

Let us assume that the motion in the individual environment is Gaussian, so that the intermediate scattering function $I(Q, t)$ is given by eq. (6.2). It is further assumed that the mean square displacement has a distribution $g(\alpha)$. There are many possible distribution functions such as Gaussian, log-Gaussian and bimodal distributions. For simplicity of calculation, we assume a Gaussian distribution as follows:

$$g(\alpha) = \frac{1}{\sqrt{2\pi\sigma^2}} \exp\Big(-\frac{(\alpha - \overline{\alpha})^2}{2\sigma^2}\Big), \tag{6.4}$$

where $\sigma^2 = \overline{\Delta\alpha^2} = \overline{(\alpha - \overline{\alpha})^2}$. From eqs. (6.1) and (6.4), the incoherent intermediate scattering function $I(Q, t)$ up to the order of Q^4 is obtained by averaging over the distribution:

$$I(Q,t) = \exp\Big(-\overline{\alpha}Q^2 + \frac{A_0\overline{\alpha}^2}{2}Q^4\Big), \tag{6.5}$$

where the non-Gaussian parameter A_0 is given by

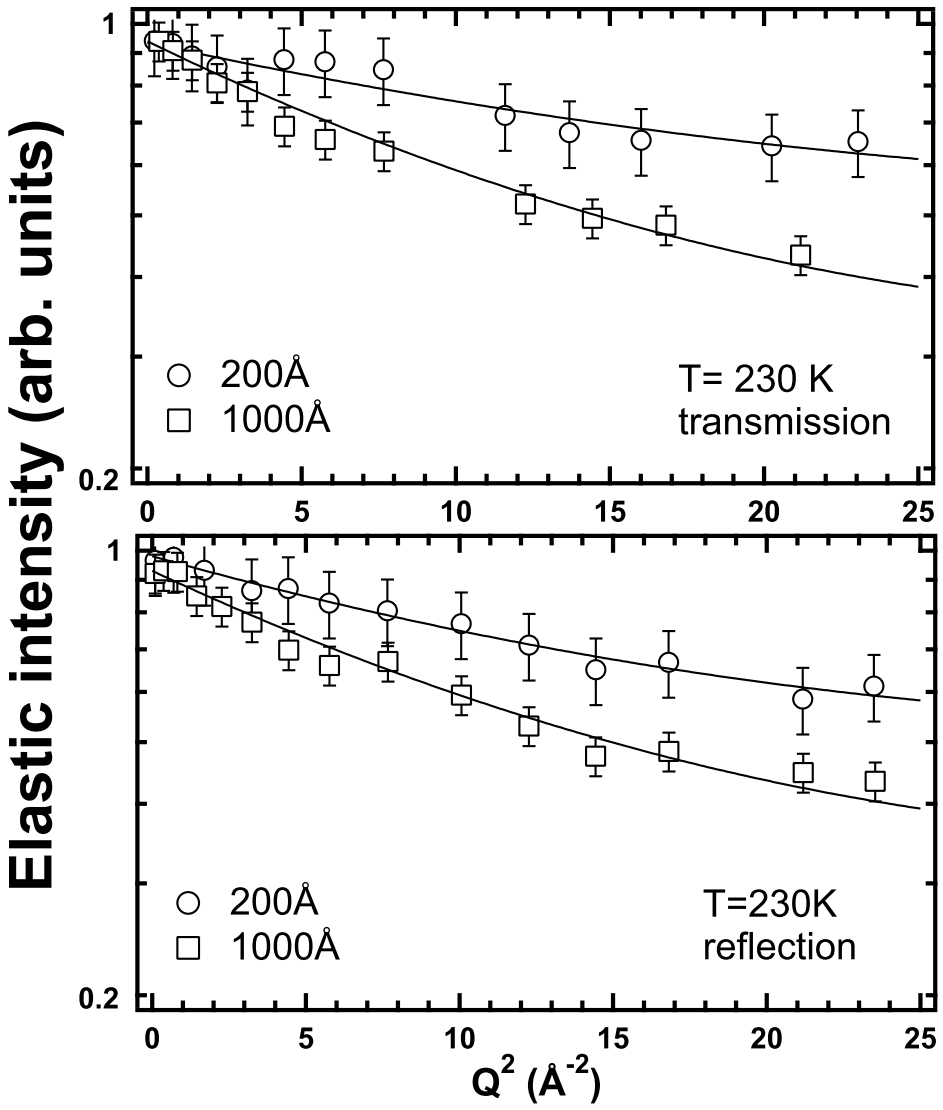

Figure 6.7: Q^2 dependence of $I_{el}(Q)$ for 1000 Å (□) and 200 Å (○) thin films in transmission and reflection geometries at 230 K and solid lines indicate the results of fit with eq. (6.7).

$$A_0 = \frac{\overline{\alpha^2} - \overline{\alpha}^2}{\overline{\alpha}^2}. \tag{6.6}$$

In the present experiment, we observe the incoherent elastic scattering intensity of dynamic scattering law $S(Q, \omega{=}0)$ as a function of Q, which is given by

$$S(Q, \omega = 0) = \exp\Big(-\overline{\alpha}Q^2 + \frac{1}{2}A_0\overline{\alpha}^2Q^4\Big). \tag{6.7}$$

As seen in eq. (6.6), the non-Gaussian parameter is a dimensionless normalized standard deviation, hence, it is a measure of dynamic heterogeneity of a system. Equation (6.7) was fitted to the observed data in Figure 6-7 and the results of fits are shown by solid curves, giving good agreements. From the non-Gaussian fits, we have evaluated the mean square displacement and the non-Gaussian parameter A_0. Note that the evaluated does not contain the contribution from at the lowest temperature (= 5 K) because the elastic scattering intensity $I_{el}(Q)$ was divided by that at the lowest temperature in order to reduce the effects from coherent scattering. We have evaluated the $\overline{\alpha}$ at the lowest temperature from the density of states $G(\omega)$ below 10 meV obtained in the Chapter 4 and corrected $\overline{\alpha}$ for this effect. These corrected mean square displacement $\overline{\alpha}$ and non-Gaussian parameter A_0 from both geometries are plotted against temperature in Figure 6-8 for the bulk, 1000 and 200 Å films. Note that the bulk data were taken from the previous paper [24], which were evaluated using triple axis spectrometer with energy resolution of 1 meV. In Figure 6-9, we also indicated the scaled distribution function of reduced $\alpha/\overline{\alpha}$ with different film thickness using obtained A_0 values. The mean square displacement $\overline{\alpha}$ increases almost linearly with temperature in the glassy state although it slightly deviates from the linear relationship in the bulk sample above about 200 K. It is due to the onset of the fast picoseocnd process. In case of thin films the onset of the fast process is suppressed, and hence the deviation is hard to see in Figure 6-2. In this chapter, therefore, we do not discuss the fast process any more. As the film thickness decreases the mean square displacement $\overline{\alpha}$ decreases, and the non-Gaussian parameter A_0 increases with decreasing temperature and film thickness, showing that the dynamic heterogeneity increases with decreasing

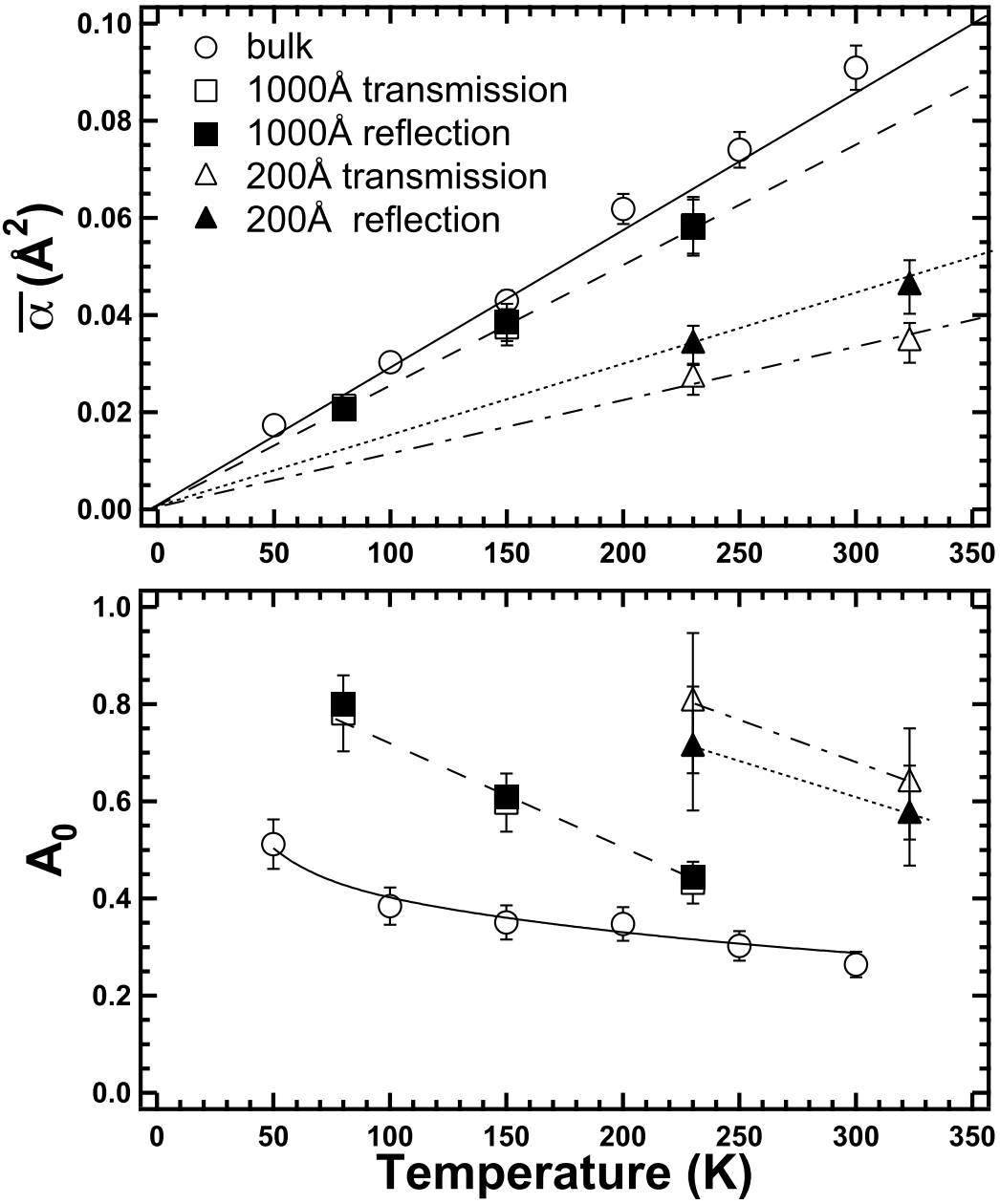

Figure 6.8: Temperature dependence of mean square displacement $\overline{\alpha}$ and non-Gaussian parameter A_0 for bulk (○), 1000 Å film in transmission (□) and reflection (■) geometries, and 200 Å film in transmission (△) and reflection (▲) geometries.

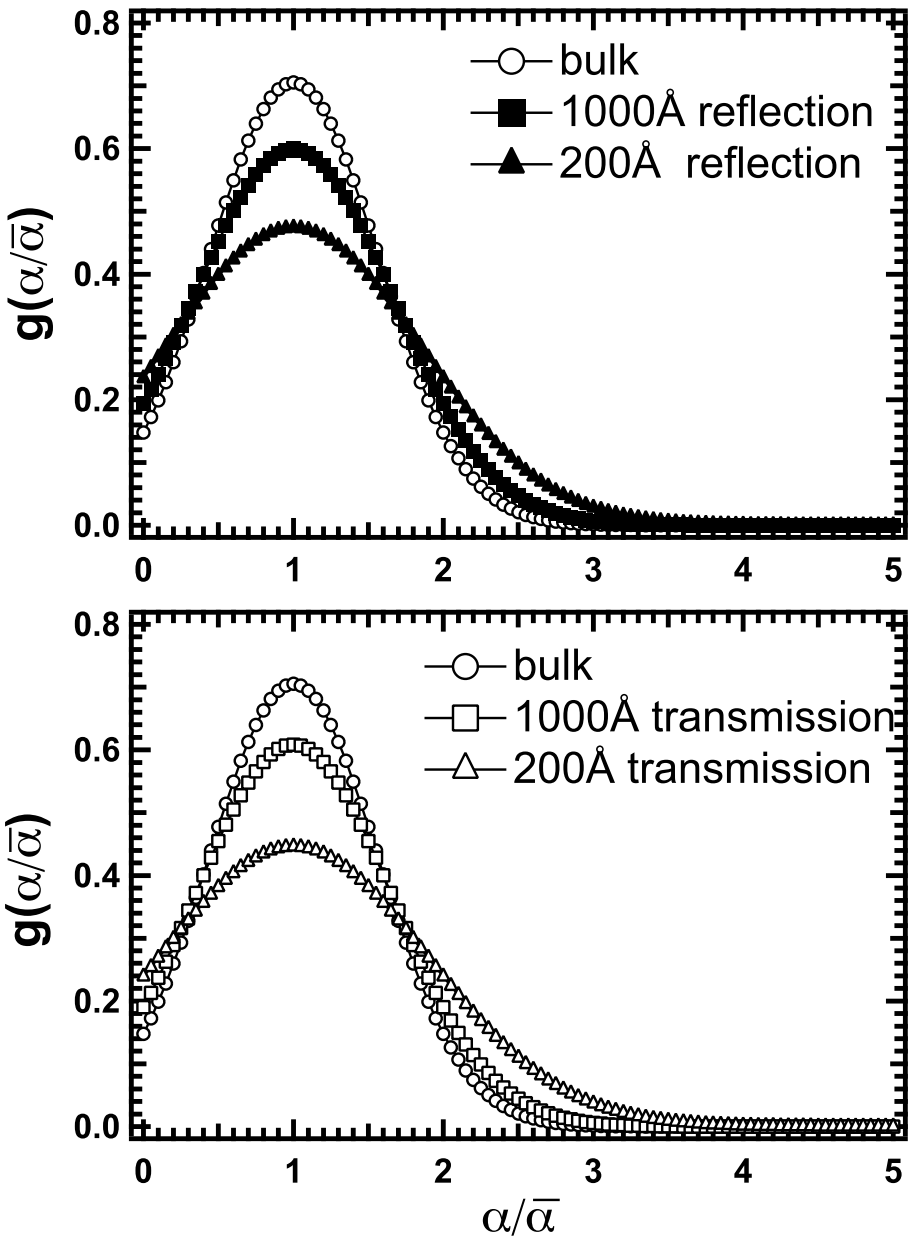

Figure 6.9: Scaled distribution function of reduced mean square displacement at 230 K for bulk, 1000 Å and 200 Å thin films.

temperature and film thickness. No differences of A_0 and $\overline{\alpha}$ were observed for the 1000 Å thin film between both geometries, indicating no dynamical anisotropy. On the other hand, the difference of $\overline{\alpha}$ value was observed for the 200 Å thin film. The A_0 value in the transmission geometry is slightly larger than that in the transmission one for the 200 Å film, which must come from the anisotropic motion. However, as mentioned above the contribution from the anisotropy to A_0 is very small and the errors in the fit are relatively large (about 20%), and hence we don't discuss the difference in both the geometries in this paper.

In order to see the film thickness dependence of $\overline{\alpha}$ and A_0 quantitatively we plotted $\overline{\alpha}$ and A_0 at 230 K in Figure 6-10 as a function of film thickness. The bulk sample (d =100μm) shows the non-Gaussian parameter of 0.32, which represents the dynamic heterogeneity intrinsic to the bulk glassy state [24-26]. As the film thickness decreases the non-Gaussian parameter increases. It is about 0.43 at 1000Å for both geometries, which is slightly higher than the bulk value, and shows steep increase below 1000 Å . The value of A_0 is about 0.80 and 0.70 for the transmission and reflection geometries at 200 Å . It is clear that the dynamic heterogeneity increases with decreasing film thickness. This excess heterogeneity must be caused by the multi-layer structure of polymer thin films, consisting of the bulk-like layer and the interface hard layer. The latter has smaller mean square displacement than the former. If the thickness of the hard layer is very small compared with the total thickness, the heterogeneity due to the multi-layer structure must be small. The steep increase in the non-Gaussian parameter A_0 below about 1000 Å may suggest that the thickness of the interface hard layer becomes not negligible below 1000 Å . In fact, the thickness of the interface hard layer [3, 16, 17] evaluated in the Chapter 4 is ∼110 Å , supporting the hypothesis that the increase in the non-Gaussian parameter is due to the multi-layer structure of the polystyrene thin films. In order to analyze the thickness dependence of A_0 we calculated A_0 assuming that the thin film consists of a bulk-like layer and an interface hard layer (bi-layer model). Here, we neglected the effect of surface layer (mobile layer) because it was not observed or detected in the glassy state. Under this assumption

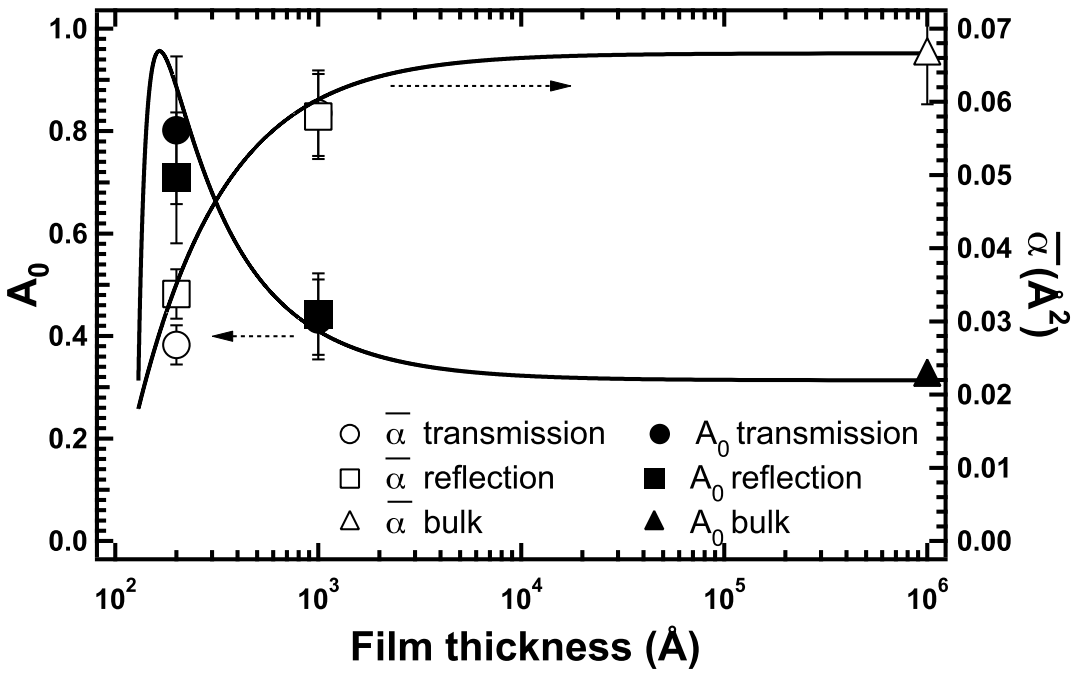

Figure 6.10: Thickness dependence of mean square displacement $\overline{\alpha}$ in transmission (○) and reflection (□) geometries, and non-Gaussian parameter A_0 in transmission (•) and reflection (■) geometries at 230 K. $\overline{\alpha}$ (△)and A_0 (▲) for bulk are also shown in figure. Solid curves are the results of fit using bi-layer model.

$\overline{\alpha}$ and $\overline{\alpha^2}$ were calculated using equations (6.8) and (6.9).

$$\overline{\alpha} = \left(1-\frac{\delta}{d}\right)\int \alpha g(\alpha)_{bulk} d\alpha + \frac{\delta}{d}\int \alpha g(\alpha)_{dead} d\alpha \tag{6.8}$$

$$\overline{\alpha^2} = \left(1-\frac{\delta}{d}\right)\int \alpha^2 g(\alpha)_{bulk} d\alpha + \frac{\delta}{d}\int \alpha^2 g(\alpha)_{dead} d\alpha, \tag{6.9}$$

where d, δ, $g(\alpha)_{bulk}$ and $g(\alpha)_{dead}$ are the total thickness, the hard layer thickness, distribution functions of α in the bulk-like layer and in hard layer, respectively. In this calculation we assumed that the hard layer thickness was independent of the total film thickness. Using the thickness of the hard layer d and the mean square displacement in the hard layer as adjustable parameters in the bi-layer model we have calculated both A_0 and $\overline{\alpha}$ to reproduce the observed film thickness dependences at 230 K and the results are shown in Figure 6-10 by solid curves. The bi-layer model seems to describe the thickness dependences of observed A_0 and $\overline{\alpha}$ well. We found in this calculation that the thickness of the hard layer was ∼130 Å and was ∼ 0.018 Å^2 at 230 K. The estimated value of the thickness is very close to that evaluated from the thickness dependence of $< u^2 >$ in Chapter 4. The value of $\overline{\alpha}$ in the hard layer (∼0.018 Å^2) at 230 K is very small compared with the bulk value (∼0.066 Å^2), supporting the multi-layer (bi-layer model in this calculation) structure in polymer thin films from dynamic point of view.

6.4 Conclusion

In this chapter, we have studied the dynamic anisotropy and the dynamic heterogeneity of polystyrene thin films in the glassy state by means of inelastic neutron scattering. We found that the small dynamic anisotropy was observed for the 200 Å film, not for the 1000 Å film, from the temperature dependence of the elastic scattering intensity. In case of the 200 Å film the mobility in the perpendicular direction to the film surface is slightly larger than that in the parallel direction, and the decrease of the mobility with the film thickness was observed for both the parallel and perpendicular directions. The dynamic anisotropy as well as the decreases in the mobility were well explained in terms of the interface hard layer between the polymer and the substrate. The dynamic heterogeneity was also studied in terms of the non-Gaussian parameter

A_0. We found that A_0 increased with decreasing the film thickness, showing the increase in the dynamic heterogeneity. Assuming that the heterogeneity arises from the multi-layer structure in addition to the intrinsic heterogeneity in the bulk glass state, we analyzed the thickness dependence of the non-Gaussian parameter using a simple bi-layer model consisting of the interface hard layer and the bulk-like layer to find that the hard layer has the thickness of $\sim$130 Å and the mean square displacement of $\sim$0.018 Å^2 at 230 K. These results obtained here support a picture that the polymer thin films have multi-layer structure, at least in dynamics.

References

[1] N. Satomi, A. Takahara, and Kajiyama, Macromolecules, **32**, 4474 (1999).

[2] T. Kajiyama, K. Tanaka, and A. Takahara, Polymer, **39**, 4665 (1998).

[3] G. B. DeMaggio, W. E. Frieze, D. W. Gidley, M. Zhu, H. A. Hristov, and A. F. Yee, Phys. Rev. Lett. **78**, 1524 (1997).

[4] W. J. Orts, J. H. vanZanten, W. W.-l. Wu, and S. K. Satija, Phys. Rev. Lett. **71**, 867 (1993).

[5] J. H. van Zanten, W. E. Wallace, and W. Wu, Phys. Rev. E **53**, R2053 (1996).

[6] T. Miyazaki, K. Nishida, and T. Kanaya, Phys. Rev. E **69**, 061803 (2004).

[7] C. J. Ellison, and J. M. Torkelson, Nature Mater. **2**, 695 (2003).

[8] R. D. Priestley, C. J. Ellison, L. J. Broadbelt, and J. M. Torkelson, Science, **309**, 456 (2005).

[9] T. Kanaya, and K. Kaji, Adv. Polym. Sci. **154**, 87 (2001).

[10] T. Kanaya, I. Tsukushi, K. Kaji, B. J. Gabrys, S. M. Bennington, and H. Furuya, Phys. Rev. B **64**, 144202 (2001).

[11] M. K. Sanyal, J. K. Nasu, A. Datta, and S. Banerjee, Europhys. Lett. **36**, 265 (1996).

[12] P. Dorucker, and W. L. Mattice, Macromolecules, **32**, 194 (1999).

[13] T. Kanaya, R. Zorn, I. Tsukushi, S. Murakami, K. Kaji, and D. Richter, J. Chem. Phys. **109**, 10456 (1998).

[14] R. Zorn, B. Frick, and L. J. Fetters, J. Chem. Phys. **116**, 845 (2002).

[15] R. Zorn, and B. Frick, J. Chem. Phys. **108**, 3327 (1998).

[16] K. Fukao, and Y. Miyamoto, Phys. Rev. E **61**, 1743 (2001).

[17] C. L. Soles, J. F. Douglas, W. Wu, H. Peng, and D. W. Gidley, Macromolecules, **37**,2890 (2004).

[18] M. Mukherjee, M. Bhattacharya, M. K. Sanyal, T. Geue, J. Grenzer, and U. Pietsch, Phys. Rev. E **66**, 061801 (2002).

[19] J. Kraus, P. Müeller-Buschbaum, T. Kuhlmann, D. W. Schubert, and M. Stamm, Europhys. Lett. **49**, 210 (2000).

[20] J. M. Zhang, D. H. Zhang, and D. Y. Shen, Macromolecules, **35**, 5140 (2002).

[21] K. S. Gautam, A. D. Schwab, A. Dhinojwala, D. Zhang, S. M. Dougal, and M. S. Yeganeh, Phys. Rev. Lett. **85**, 3854 (2000).

[22] A. Rahman, K. S. Singwi, and A. Sjölander, Phys. Rev. **126**, 986 (1962).

[23] R. Zorn, Phys. Rev. B **61**, 6249 (1997).

[24] T. Kanaya, I. Tsukushi, and K. Kaji, Prog. Theor. Phys. Suppl. **126**, 133 (1997).

[25] T. Kanaya, I. Tsukushi, K. Kaji, B. J. Gabrys, and S. M. Bennington, J. Non-Cryst. Solids. **235-237**, 212 (1998).

[26] T. Kanaya, U. Buchenau, S. Koizumi, I. Tsukushi, and K. Kaji, Phys. Rev. B **61**, R6451 (2000).

Chapter 7

Glass Transition of Polystyrene Thin Films by High Energy Resolution Spectrometer

7.1 Introduction

In the previous chapters, we have studied the meV dynamics of polymer thin films by inelastic neutron scattering, and we observed only one relaxational process (the picoseconds fast process) that is related to the local relaxation even above bulk T_g. We could not observe the relaxational process that is directly related to the glass transition even above the bulk T_g. Even in the case of bulk PS, the glass transition was not observed with the energy resolution at around δE ~0.20 meV [1]. The failure of detection of glass transition is due to the lack of energy resolution. From the former glass transition studies on bulk amorphous polymers by inelastic neutron scattering, it is clear that energy resolution of about μeV is necessary to detect the glass transition and such a high energy resolution [2-4] can be obtained in neutron backscattering spectrometers (BS) and neutron spin echo spectrometers (NSE). In the case of polymer thin films, Soles et al. have successfully detected the glass transition temperature (T_g) using backscattering spectrometer with several amorphous polymers [5,6]. In this chapter, we have studied the glass transition dynamics using relatively high energy resolution TOF spectrometer OSIRIS (δE ~0.025 meV) [7] in order to study the mechanism of glass transition of polymer thin films from dynamics. This energy resolution seems to be insufficient for the detection of glass transition, however Kanaya et al. reported

the possibility of detection of high frequency tail of the α process with similar energy resolution (δE $\sim$0.016 meV) for several amorphous polymers [8]. Therefore, we believe the detection of glass transition with this energy resolution.

7.2 Experimental

The sample used for the scattering experiments was amorphous polystyrene (PS) with molecular weight M_w= 2.90$\times 10^5$ and molecular weight distribution M_w/M_n=1.06, where M_w and M_n are the weight-average and the number-average of the molecular weight, respectively. The detail of sample preparation was written in Chapter 4 and we prepared films 1000 Å , 400 Å and 200 Å thick in addition to bulk in this chapter and 300 sheets of the films on Al foils were placed into a cylindrical Al cell 20 mm in diameter and 45 mm high.

Elastic and inelastic neutron scattering measurements were performed on an inverted geometry time-of-flight spectrometer OSIRIS installed at the pulsed neutron source in ISIS, Rutherford Appleton Laboratory, Didcot. In the present measurements, the final energy E_f was set to 1.85 meV and the energy resolution δE was 0.025 meV, which was evaluated from the half-width at the half-maximum of elastic scattering on the energy gain side. We have conducted elastic energy window scans in addition to the full spectra measurements, and the measurements were carried out at temperatures from 33 K to 423 K, covering the bulk glass transition temperature T_g of 373 K.

7.3 Results and Discussion

Figure 7-1 indicates the one example for dynamic scattering law $S(Q, \omega)$ obtained with LAM-40 at 403 K (Chapter 4) and OSIRIS at 408 K for 1000 Å thin films at the almost same Q values. The $S(Q, \omega)$ spectrum from OSIRIS was within the resolution function of LAM-40, indicating that OSIRIS could detect slower dynamics than that from LAM-40 because energy resolution was inversely related to the detection time. First we studied the temperature dependence of elastic scattering intensity and temperature dependence of $I_{el}(Q)$ at Q=1.76 Å^{-1} for bulk and 1000 Å was shown in

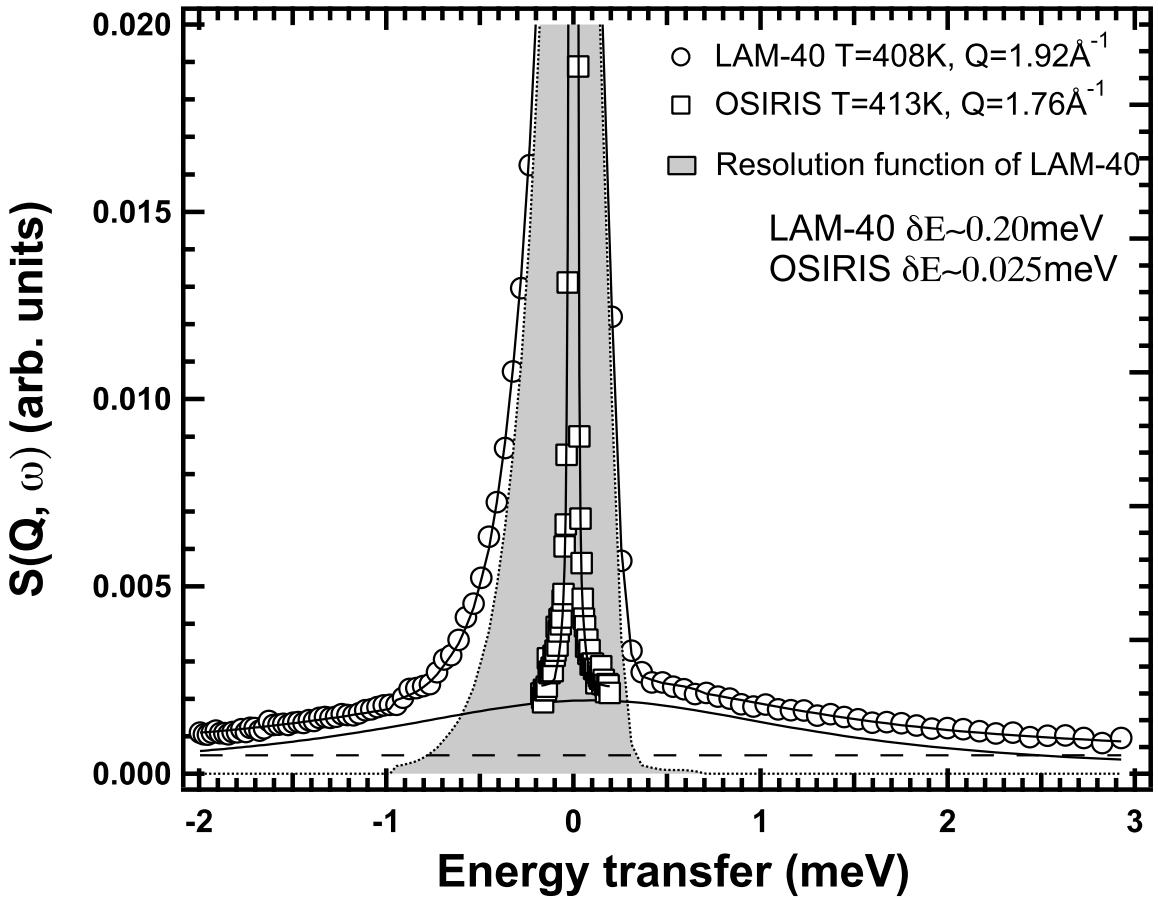

Figure 7.1: Dynamics scattering law $S(Q,\,\omega)$ of 1000 Å PS thin films measured by two TOF spectrometers LAM-40 at 403 K (∘) and OSIRIS (□) at 408 K with energy resolutions δE=0.20 meV and δE=0.025 meV.

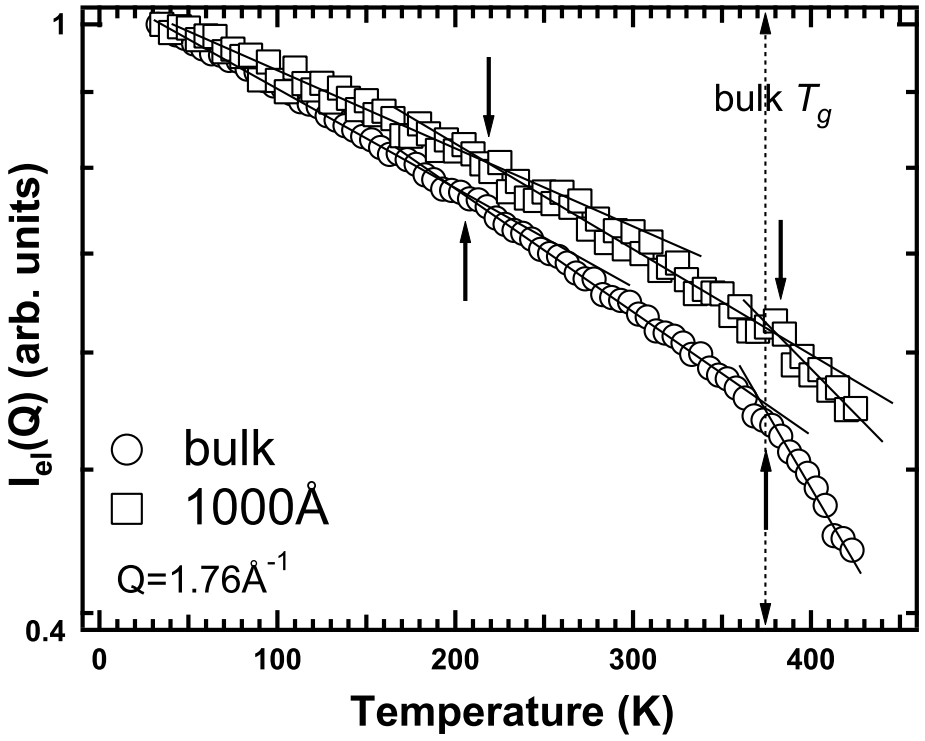

Figure 7.2: Temperature dependence of elastic scattering intensity $I_{el}(Q)$ obtained from bulk (∘) and 1000 Å thin films (□) at Q=1.76 Å^{-1} and arrows indicate the onset of relaxational process.

Figure 7-2. The slope of temperature dependence of $I_{el}(Q)$ for bulk was larger than that of the 1000 Å thin film, indicating the decrease of mobility in the 1000 Å film. In the low temperature region below about 200 K, $I_{el}(Q)$ linealy decreased with increasing temperature while it began to decrease more steeply with increasing temperature above about 200 K, indicating the onset of quasielastic scattering. As indicated by arrows in Figure 7-2, there exist two changes of the slope in the temperature dependence of $I_{el}(Q)$; one is located at around 200 K and the other is at around 370 K for both the samples. This suggests that there exists at least two relaxational process in the temperature range examined. As reported in Chapter 4, the change at ∼200 K was attributed to the onset of the fast process and the onset temperature seemed to shift to higher temperature with decreasing the film thickness, suggesting the hardening of polymer chain with decreasing the film thickness. The onset temperature at ∼373 K coincided with T_g determined by DSC for bulk PS. Definite physical origin of the relaxational process that onsets at ∼370 K is still unknown and under discussion. Kanaya et al. suggested that this relaxational process was related to the conformational change of polymer chains and also indicated a possibility of the high frequency tail of α process [8]. In any case this relaxation process appears at the glass transition temperature, so that in this chapter, we defined this onset temperature as T_g for thin films. As can been seen in Figure 7-3, the onset temperature for the 1000 Å film is higher than that for the bulk. In order to identify this behavior clearly, we have evaluated the temperature dependence of mean square displacement $< u^2 >$ for bulk, 1000 Å , 400 Å and 200 Å thin films using the same procedure as that described in Chapter 4. The temperature dependence of $< u^2 >$ is indicated in Figure 7-3 and the decrease of $< u^2 >$ with film thickness was also observed in the high energy resolution measurements (δE ∼0.025 meV). As indicated by arrows in Figure 7-3, the onset temperature of the relaxtional process appearing at ∼370 K in the bulk shifted to higher temperature with decreasing film thickness, suggesting increase of T_g with decreasing the film thickness. Figure 7-4 shows the thickness dependences of T_g, which were obtained from the inelastic neutron scattering with OSIRIS and ellipsometry. The latter was taken from Chapter 3.

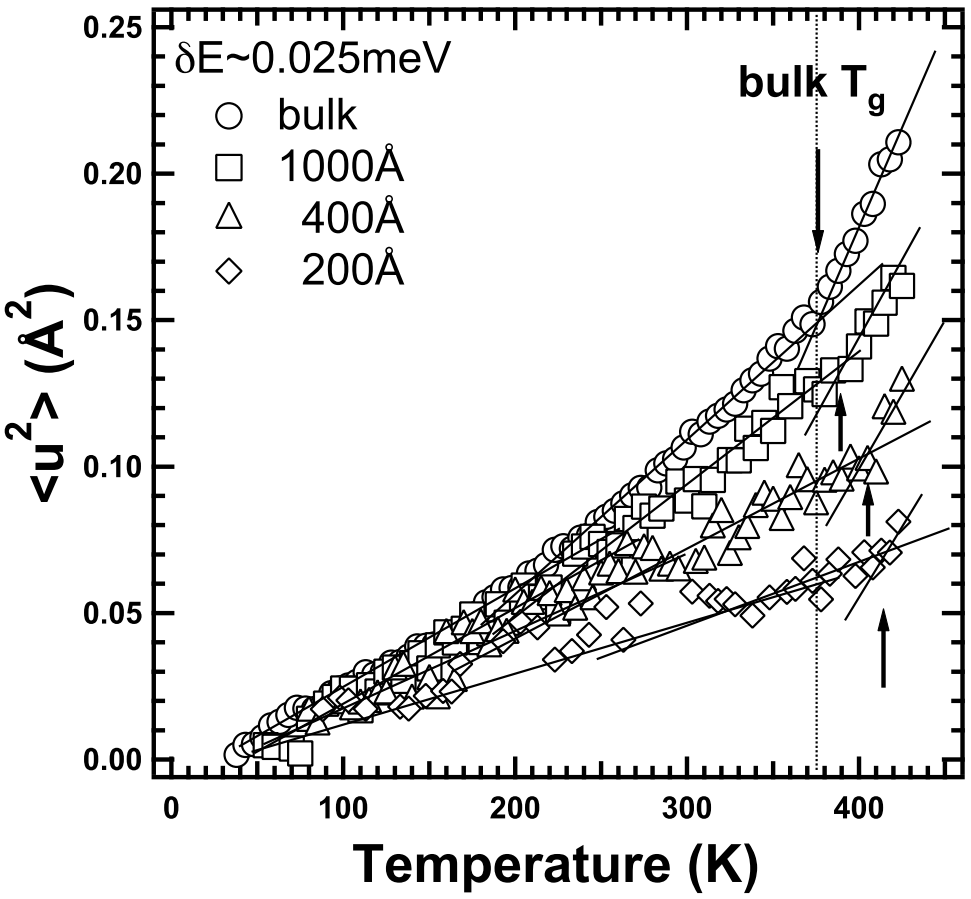

Figure 7.3: Temperature dependence of mean square displacement $< u^2 >$ for bulk ($\circ$), 1000 Å ($\square$), 400 Å ($\triangle$) and 200 Å ($\diamondsuit$) thin films and arrows indicate T_g evaluated from the onset temperature of relaxational process.

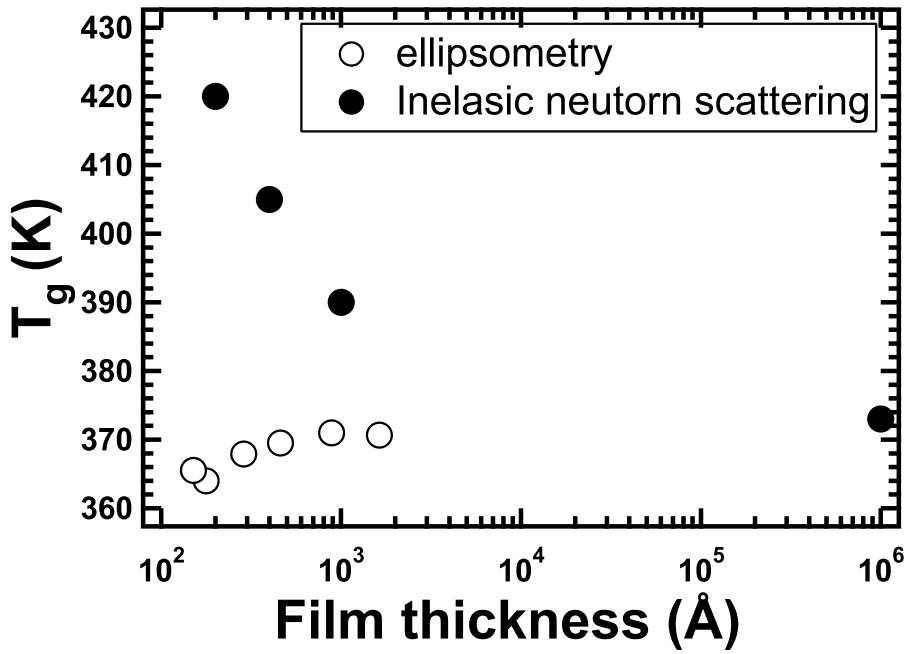

Figure 7.4: Thickness dependence of T_g evaluated from two methods ellipsometry (○) and inelastic neutron scattering (●).

Although the sample conditions were almost the same for both the measurements, totally different thickness dependence of T_g was observed. In the case of 200 Å thin films, the value of T_g is 40 K higher than that of bulk. Similar contradiction for the thickness dependence of T_g was observed by Soles et al. They studied the thickness dependence of T_g for polycarbonate (PC) thin films by X-ray reflectivity (XR), positron annihilation lifetime spectroscopy (PALS), and inelastic neutron scattering by a back scattering machine (δE $\sim$0.001 meV) [5]. The data from XR and PALS exhibited the decrease of T_g with film thickness, however only the data from inelastic neutron scattering exhibited the increase of T_g with decreasing the film thickness. Soles et al. studied the dynamical behavior of polymer thin films by neutron back scattering using several amorphous polymers, too [6] and found that $< u^2 >$ decreased and T_g increased with decreasing thickness for all the polymers investigated regardless of strength of interactions with substrate [6]. Considering these reported results, it was supposed that the increase of T_g and decrease of $< u^2 >$ with film thickness revealed by the inelastic neutron scattering might be related to some nature of polymer thin films though we don't have definite physical picture in order to explain this contradiction results. Soles et al. reported the frequency shift of alpha relaxation might be concerned with the contradict results, however the satisfactory explanation was not obtained from this physical picture [5].

In the following, we would like to discuss several possibilities for the explanation of our results. First possibility is the broadening of relxational time of the α process. In fact, the broadening of relaxation time of the α process with decreasing film thickness was observed by dielectric relaxation (DR) [9] and dynamic mechanical analysis (DMA) [10], and it confirms the heterogeneous dynamics of polymer thin films. The investigated time region strongly depends on measurement methods as shown in Figure 1-6. If the broadening of relaxation time of α process occurred with decreasing thickness, the observed distribution of relaxation time of α process in thin films would change apparently compared to that of bulk, depending on evaluation methods. As the result of the apparent change of distribution of relaxation time of α process, the

average relaxation time of α process over the frequency of thin films also change with the film thickness. Apparent increase or decrease of T_g of polymer thin films would occur compared to bulk and different thickness dependence of T_g would be observed. In fact, Scönhals et al. studied the dynamics of poly(methyl phenyl siloxane) (PMPS) confined to nano porous glass by combing dielectric spectroscopy (DS), temperature modulated DSC (TMDSC) and inelastic neutron scattering. In high frequency region, bulk exhibited faster dynamics than that of confined PMPS, however bulk exhibited slower dynamics that that of confined one in the low frequency region [11]. We supposed that the broadening of relaxational time might be related to the contradictory results from two different methods as to thickness dependence of T_g.

Inelastic neutron scattering (INS) probes dynamics in relatively microscopic scale ($\sim$Å), hence dominant Q value or spatial scale by INS is very different from those of other methods. In addition, strong Q dependence of relaxation time of α process ($\tau \sim Q^{-4}$) was observed for glass-forming polymer even in the time region investigated by INS [12]. This implies that the average relaxation time would be also strongly affected by spatial scale. The average Q value is at around 1 Å^{-1} in this INS measurements and the spatial scale is equal to the thickness of thin film in ellipsometry measurements, hence probed spatial scale differed much between the INS and ellipsometry measurements. Therefore, it was supposed that different spatial scale affected the average relaxation time of α process and the different thickness dependence of T_g by two methods. This is a second possibility to explain the contradiction results.

Compared to neutron back scattering spectrometer (δE $\sim$0.001 meV), the energy resolution of OSIRIS (δE $\sim$0.025 meV) is not high and it indicates the low sensitivity to dynamics of α process. Therefore OSIRIS needs higher temperature for the detection of α process than real one and about 40 K increase of T_g for 200 Å thin film might be related to the lack of energy resolution. Low sensitivity to α process with this INS measurement might be related to the contradiction results by two different methods.

At present stage, we don't know the appropriate explanation for the contradiction of T_g and more experimental investigations are needed in order to extract the final

conclusion.

7.4 Conclusion

In this chapter, we have studied the glass transition of polymer thin films with inelastic neutron scattering, using relatively high energy resolution spectrometer, OSIRIS. We observed another relaxational process in addition to the fast process and defined the onset temperature of the relaxational process as T_g from inelastic neutron scattering because the onset temperature coincided to the glass transition temperature of bulk. On the contrary to our expectation, T_g increased with decreasing film thickness from the inelastic neutron scattering, and we observed totally different thickness dependence of T_g between the ellipsometry and inelastic neutron scattering measurements under the same sample condition. At the present stage, we don't have definite physical picture in order to understand this contradiction, however we discussed three possible reasons for the contradiction: the broadening of the distribution of the relaxation time, the different spatial scales probed by the two methods, and the low energy resolution of the OSIRIS measurements. More experimental investigations are needed in order to extract final conclusion.

References

[1] T. Kanaya, T. Kawaguchi, and K. Kaji, J. Chem. Phys. **104**, 3841 (1996).

[2] B. Frick, U. Buchenau, and D. Richter, Colloid. Polym. Sci. **273**, 413 (1995).

[3] D. Richter, B. Frick, and B. Farago, Phys. Rev. Lett. **61**, 2465 (1988).

[4] D. Richter, R. Zorn, B. Farago, B. Frick, and L. J. Fetters, Phys. Rev. Lett. **68**, 71 (1992).

[5] C. L. Soles, J. F. Douglas, W. Wu, H. Peng, and D. W. Gidley, Macromolecules, **37**, 2890 (2004).

[6] C. L. Soles, J. F. Douglas, W. Wu, H. Peng, and D. W. Gidley, Macromolecules, **36**, 373 (2003).

[7] M. T. F. Telling, and K. H. Anderson, Phys. Chem. Chem. Phys. **7**, 1255 (2005).

[8] T. Kanaya, T. Kawaguchi, and K. Kaji, Macromolecules, **32**, 1672 (1999).

[9] K. Fukao, and Y. Miyamoto, Phys. Rev. E **61**, 1743 (2001).

[10] K. Akabori, K. Tanaka, T. Nagamura, A. Takahara, and T. Kajiyama, Macromolecule, **38**, 194 (2005).

[11] A. Schönhals, H. Goering, C. Schick, B. Frick, M. Mayorova, and R. Zorn, Eur. Phys. J. ST, **141**, 255 (2007).

[12] J. Colmenero, A. Alegria, J. M. Alberdi, F. Alvarez, and B. Frick, Phys. Rev. B **44**, 7321 (1991).

Chapter 8

Distribution of Glass Transition Temperature (T_g) in Polystyrene Thin Films

8.1 Introduction

The singularity of polymer thin films including T_g behaviour is understood in terms of the heterogeneous structure of polymer thin film [1-5] and we have also reported that polymer thin films are more heterogeneous than bulk from the point view of dynamics, as shown in Chapter 6. As pointed out by de Gennes [6] "future experiments should aim not at the determination of a single T_g but a distribution of T_g". The notion of multi-layer structure or distribution of T_g in a thin film was confirmed by Torkelson et al. experimentally using multilayer thin films including large fluorescent dye molecules [7,8]. However, Torkelson et al. only focused on the temperature dependence of integrated intensity of fluorescence molecule, other factors like the annealing effect [9] and/or inter-diffusion effect [10-12] were not discussed clearly in the work. In order to reveal the mechanism of glass transition of polymer thin films in more detail, we have to study the distribution of glass transition temperatures in the polymer thin films. In this chapter, we study the distribution of T_g in polymer thin films using multi-layered thin film by stacking hydrogenated PS (h-PS) and deuterated PS (d-PS) with neutron reflectivity (NR). Neutron can discern h-PS layer and d-PS layer clearly due to the difference of neutron scattering length density, hence we can evaluate T_g at a given position. We can evaluate accurate thickness and roughness by NR, and we believe

that NR can reveal another aspect of the glass transition of thin films compared to fluorescence/multilayer method.

8.2 Experimental

We used hydrogenated polystyrene (h-PS) with molecular weight (M_w) of 7.69×10^5 and molecular weight distributions (M_w/M_n) 1.18 and deuterated polystyrene (d-PS) with molecular weight (M_w) of 7.31×10^5 and molecular weight distributions (M_w/M_n) of 1.08, and we prepared d-PS/h-PS/d-PS tri-layered thin films. We chose relatively high molecular weight for both h-PS and d-PS in order to minimize the inter-layer diffusion effect. The bulk T_g of both h-PS and d-PS were 376K, which was determined by DSC. First we prepared a d-PS layer onto a 3 inch Si substrate by spin-coating toluene solutions at 2000 rpm and dried in a vacuum oven at 343 K for 24 h after drying in vacuum at room temperature for 2 days in order to remove residual solvent. For the second film preparation, we conducted surface treatment of Si substrate in order to remove thin films from Si substrate easily. We immersed a 4 inch Si substrate into 80/20 volume ratio solutions of concentrated H_2SO_4 (97%) and H_2O_2(34.5%) at 393 K for 1h and rinsed with water and ethanol several times in order to remove H_2SO_4/H_2O_2 solution [13]. Finally we can obtain a 4 inch Si substrate with hydroxyl surface. After the surface treatment with H_2SO_4/H_2O_2 solution, we prepared h-PS layer onto the 4 inch Si substrate with hydroxyl surface by spin-coating toluene solutions at 2000 rpm. Such prepared thin film (h-PS layer) was transferred from 4 inch Si substrate onto a water surface and collected onto the first d-PS layer, which was already prepared onto 3 inch Si substrate. Collected h-PS/d-PS bi-layer was dried in the vacuum oven at 343 K for 24 h after drying in vacuum at room temperature for 2 days in order to remove residual solvent. Using the similar procedure, we could obtain d-PS/h-PS/d-PS tri-layer thin films. After making d-PS/h-PS/d-PS tri-layer, we annealed this thin film at 365 K that is about 10 K below bulk T_g for 12 h in order to minimize the effect of inter-layer diffusion between h-PS layer and d-PS layer.

The neutron reflectivity measurements were done with MINE-II reflectometer [14]

installed JRR-3M reactor, Tokai and the measurements were performed at several temperatures from 298 K to 403 K in a vacuum cell. In order to avoid the inter-diffusion between different layers especially above T_g, data acquisition times at a given temperature were limited to 1.5 h.

8.3 Results and Discussion

Figure 8-1 indicates the reflectivity at several temperatures obtained from d-PS/h-PS/d-PS tri-layer. If the severe inter-diffusion between different layers occurred, the fringes disappeared due to the large roughness between layers [10-12]. In this experiment, the fringes were clearly visible even above bulk T_g, indicating that the inter-diffusion was depressed in the experimental time scale. The reflectivity profiles were analyzed with the formula derived by Parratt [15]. Figure 8-2 indicates the results of fit with a three-layer model at 298 K and 403 K and inset indicates the depth profile of neutron scattering length density. The agreements of the fits are very good for both temperatures, indicating that the three-layer model is appropriate to describe the obtained reflectivity profile from d-PS/h-PS/d-PS tri-layer both above and below bulk T_g. Using a simple three-layer model, we have evaluated the film thickness and roughness at each temperature. First we examined the temperature dependence of the total film thickness, which was obtained by simply adding the thickness of each layer in Figure 8-3. With increasing temperature from 298 K, the total film thickness increased, which was supposed to be caused by the thermal expansivity in glassy state. However, the total film thickness began to shrink above 388 K on the other hand, indicating the occurrence of so-called negative expansivity. Orts et al. first reported the negative expansivity of polymer thin films thinner than 250 Å by XR and Kanaya et al. reported that the negative expansivity in glassy state was mainly caused by the unrelaxed structure due to the lack of annealing [9,16]. In this experiment, we have annealed the stacked thin film below bulk T_g in order to avoid the inter-layer diffusion as much as possible, therefore the structural relaxation was not enough. Kanaya et al. also reported that the T_g value was not affected regardless of annealing condition even

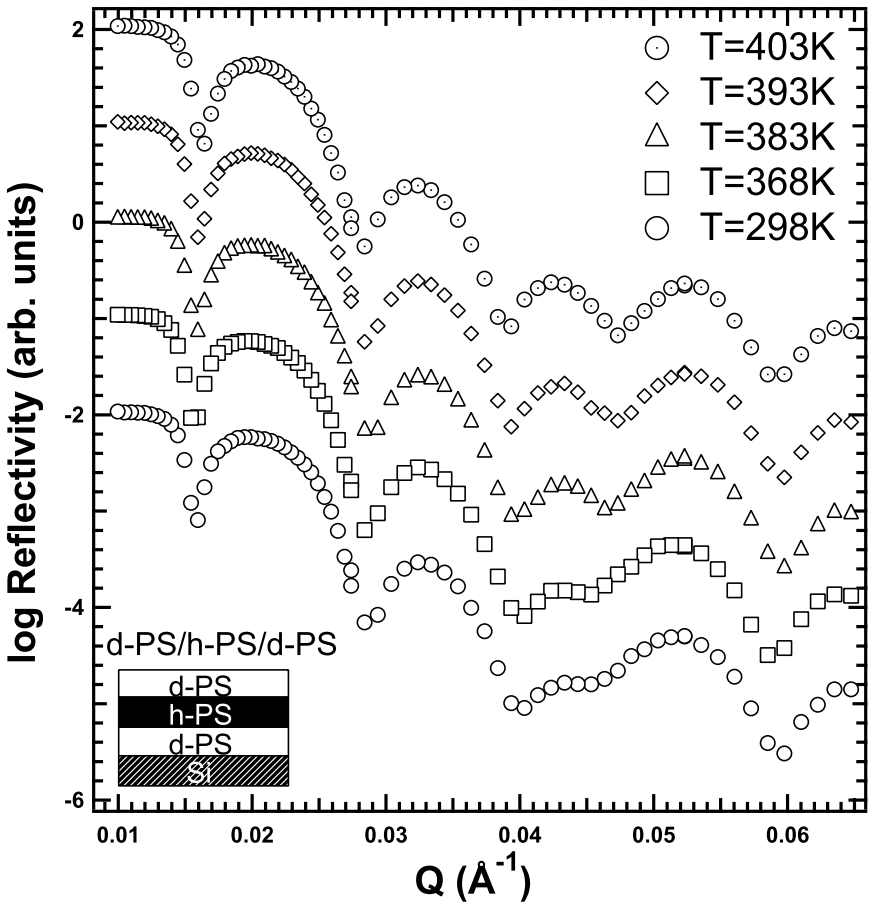

Figure 8.1: Neutron reflectivity profiles from dPS/hPS/dPS stacked tri-layer thin films at T=298 K (○), T=368 K (□), T=383 K (△), T=393 K (◇) and T=403 K (⊙) and each reflectivity profile was shifted in the vertical direction for clarification.

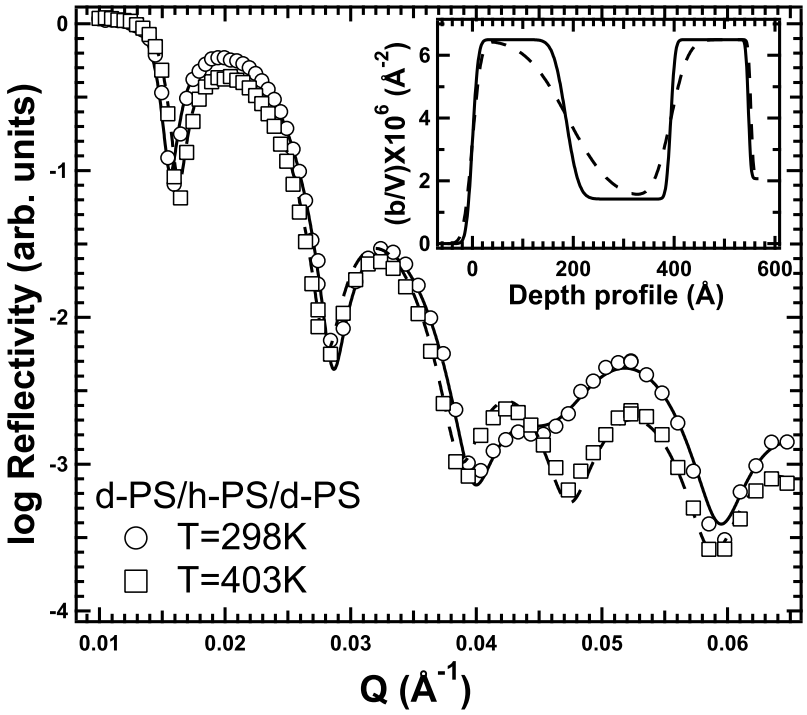

Figure 8.2: Neutron reflectivity profiles from dPS/hPS/dPS stacked tri-layer thin films at T=298 K (∘) and T=403 K (□). Solid and dashed curves are the results of fit using a three-layer model at 298 K (—) and 403 K (– –), respectively. Inset indicates the depth profile of neutron scattering length density at 298 K (—) and 403 K (– –).

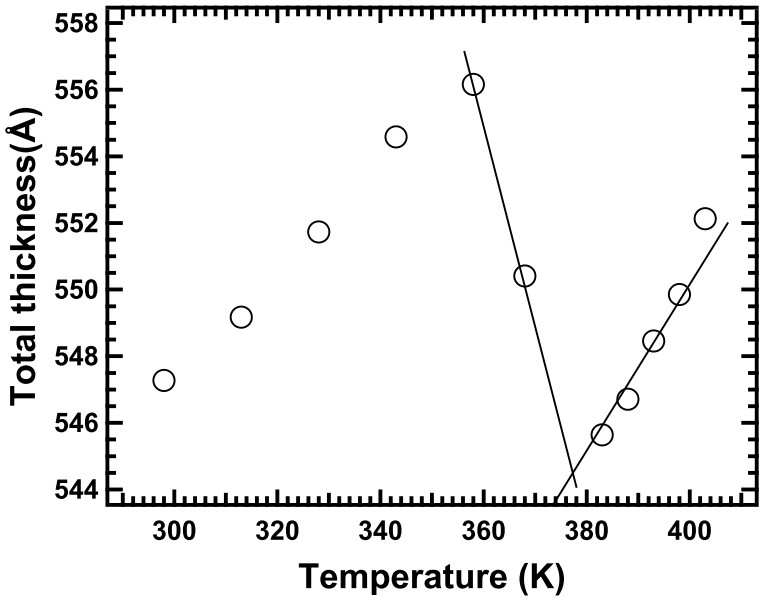

Figure 8.3: Temperature dependence of total film thickness obtained from the addition of the thickness of each layer and the intersection of two solid lines indicates the T_g of the total thickness of stacked film.

in the case of below T_g [9]. We tried to evaluate T_g of the stacked film from Figure 8-3, the intersection of solid lines was located at around 378K. The evaluated T_g value was almost the same as T_g evaluated from DSC ($\sim$376 K) and reported T_g value of thin PS films with similar thickness was not so different from the bulk value [2,3]. Therefore, we could estimate T_g from the temperature dependence of thickness in spite of the negative expansivity. Next, we examined the temperature dependence of thickness of each layer (h-PS or d-PS layer) independently as shown in Figure 8-4. The top, middle and the bottom figures correspond to the surface d-PS layer, the middle h-PS layer and the bottom d-PS layer at the Si substrate, respectively. The temperature dependence of thickness of the middle h-PS layer and the bottom d-PS layer was similar to that of total film thickness, showing negative expansivity. The surface d-PS layer also exhibited small negative expansivity, however the slope is not so large compared to other two layers and the onset temperature of negative slope of the surface layer seemed to be lower than those of other two layers. We have already shown that the decrease of T_g with thickness was caused by the high mobility of the surface layer in Chapter 3 and the layer near the substrate has lower mobility than that of bulk in Chapter 6. Although we don't have the physical picture to understand this behavior at present stage, we supposed that these observations might be related to the mobility of each layer and the different mobility of each layer affected the structural relaxation. In order to confirm this supposition, we have to study the annealing effect on multi-layer thin films clearly. From the intersection of the solid lines shown in Figure 8-4, we have evaluated T_g of each layer and the evaluated T_g of each layer from the top to bottom is 363 K, 390 K, and 383 K, respectively. Certainly, T_g of the middle layer and the bottom layer are higher than that of surface layer and this indicated the heterogeneous structure of polymer thin films. Tanaka et al. also reported that T_g at the solid/polymer interface was higher than that of bulk T_g by fluorescence lifetime measurement using evanescent wave excitation [17]. First we assumed that T_g monotonously increased with approaching to the substrate, however T_g of the middle h-PS layer is the highest among three layers. Though the definite answer is unknown at present stage from

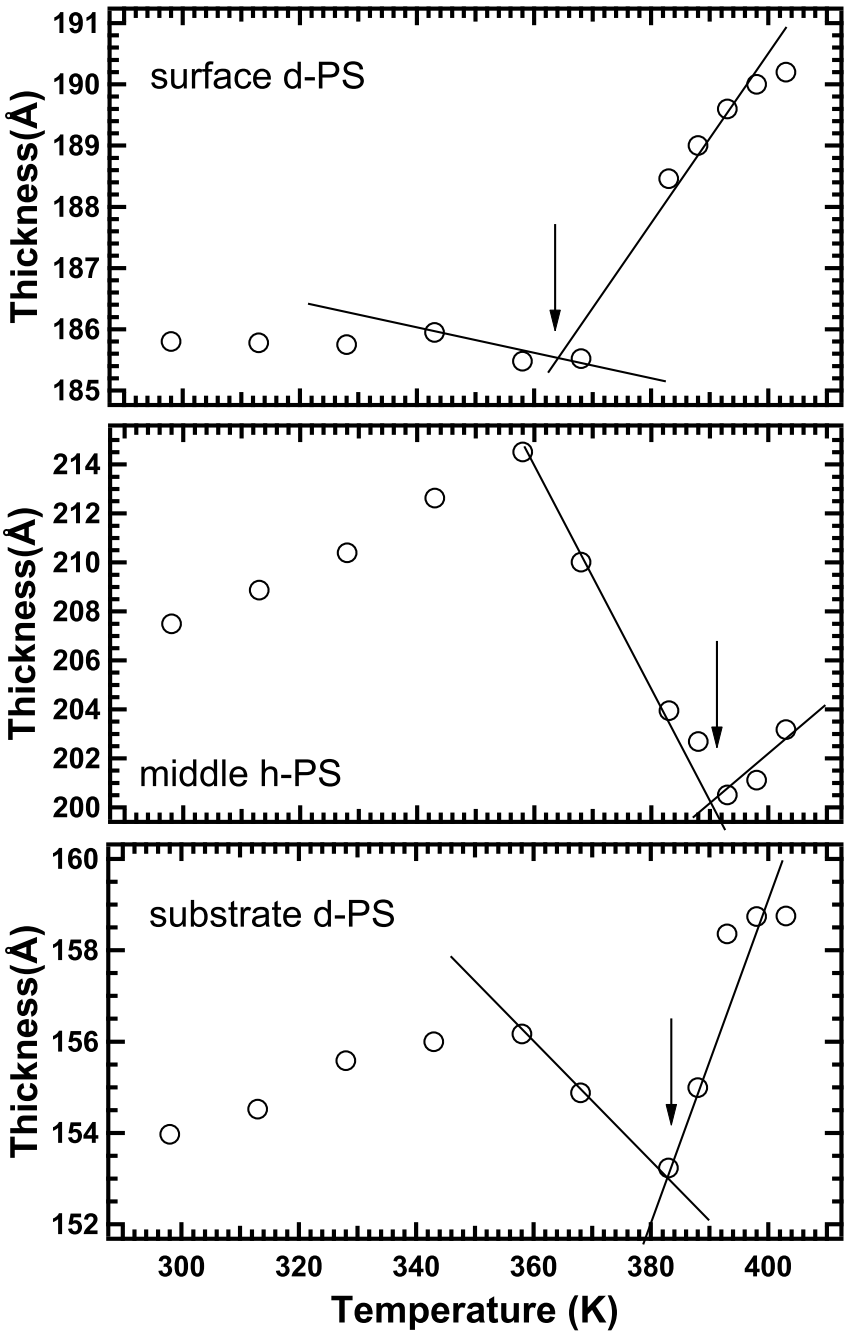

Figure 8.4: Temperature dependence of thickness for each layer and and down arrows indicate the evaluated T_g from each layer.

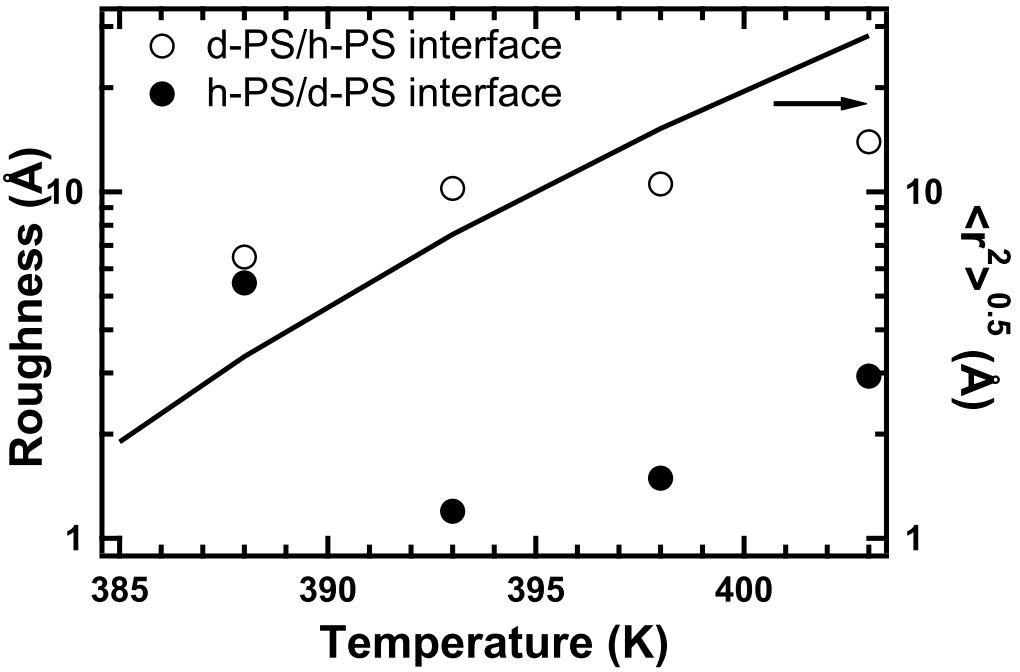

Figure 8.5: Temperature dependence of roughness at d-PS/h-PS interface (∘) and h-PS/d-PS interface (•) and solid line shows the temperature dependence of root of mean square displacement estimated from reptation.

this data only, the annealing effect or other factors might be concerned. Figure 8-5, we showed the temperature dependence of roughnesses in order to analyze the thermal behvaiour in more detail. The roughness at the interface between the surface d-PS layer and the middle h-PS layer (d-PS/h-PS interface) is much larger than that between the middle h-PS layer and the bottom d-PS layer (h-PS/d-PS interface), reflecting the higher T_g of the bottom d-PS layer than that of the surface d-PS layer. If each layer has the same glass transition temperature, such an asymmetry of roughness would not be observed. The difference of T_g of each layer is related to the difference of the roughness.

Finally, we estimated the root of mean square displacement of center of mass ($\sqrt{< r^2 >}$) for the evaluation of inter-layer diffusion effect. We assumed that the inter-layer diffusion was mainly caused by reptation, hence we used the below relation

$$\sqrt{< r^2 >} = \sqrt{6Dt/3} = \sqrt{2Dt}, \tag{8.1}$$

where t is annealing time and D is bulk-diffusion diffusion constant D [10]. Compared to the calculated $\sqrt{< r^2 >}$, the roughness at the interface between the surface d-PS and the middle h-PS exhibited similar value. On the other hand, the roughness at the interface between the middle h-PS and the bottom d-PS was much smaller than $\sqrt{< r^2 >}$ from reptation. It was supposed that the reduced mobility of polymer chain of the bottom d-PS layer compared to that of the surface d-PS layer might be related to the present result.

8.4 Conclusion

In this chapter, we have evaluated the distribution of T_g in a polymer thin film using tri-layer stacked thin film. Due to the lack of annealing, the negative expansivity was observed, however the evaluated T_g value from the total film thickness was not so different from the value evaluated from DSC. Therefore we evaluated T_g of each layer from the temperature dependence of the thickness. T_g of the surface layer was lower than that of bulk, and T_g from the middle layer and the bottom layer were higher than that of bulk. Although we have to consider the annealing effect of multi-layer thin films

clearly, we could roughly withdraw the distribution of T_g in the thin film. The interface roughness between the bottom d-PS layer and the middle h-PS layer was much lower than that between the middle h-PS layer and the substrate d-PS layer. This data would be related to the difference of T_g of each layer, supporting the heterogeneous structure of the polymer thin film.

References

[1] J. L. Keddie, R. A. L. Jones, and R. A. Cory, Europhys. Lett. **27**, 59 (1994).

[2] T. Miyazaki, K. Nishida, and T. Kanaya, Phys. Rev. E **69**, 061803 (2004).

[3] S. Kawana, and R. A. L. Jones, Phys. Rev. E **63**, 21501 (2001).

[4] K. Dalnoki-Veress, J. A. Forrest, C. Murray, C. Gigault, and J. R. Dutcher, Phys. Rev. E **63**, 31801 (2001).

[5] J. L. Keddie, R. A. L. Jones, and R. A. Cory, Faraday. Discuss. **98**, 219 (1994).

[6] P. G. de Gennes, Eur. Phys. J. E **2**, 201(2000).

[7] C. J. Ellison and J. M. Torkelson, Nature Mater. **2**, 695 (2003).

[8] R. D. Priestley, C. J. Ellison, L. J. Broadbelt, and J. M. Torkelson, Science, **309**, 456 (2005).

[9] T. Kanaya, T. Miyazaki, H. Watanabe, K. Nishida, H. Yamano, S. Tasaki, and D. B. Bucknall, Polymer, **44**, 3769 (2003).

[10] A. Karim, A. Mansour, G. P. Felcher, and T. P. Russel. Phys. Rev. B **42**, 6846 (1990).

[11] D. Kawaguchi, K. Masuoka, A. Takano, K. Tanaka, T. Nagamura, N. Torikai, R. M. Dalgliesh, S. Langridge and Y. Matsushita, Macromolecules **39**, 5180 (2006).

[12] T. Kuhlmann, J. Kraus, P. Müller-Buschbaum, D. W. Schubert, and M. Stamm, J. Non-Cryst. Solids. **235-237**, 457 (1998).

[13] N. Hosaka, N. Torikai, H. Otsuka, and A. Takahara, Langmuir, **23**, 902 (2007).

[14] T. Ebisawa, S. Tasaki, Y. Otake, H. Funahashi, K. Soyama, N. Torikai, and Y. Matsushita, Physica B **213/214**, 901 (1995).

[15] L. G. Parratt, Phys. Rev. **95**, 359 (1954).

[16] W. J. Orts, J. H. vanZanten, W. W. -l. Wu, and S. K. Satija, Phys. Rev. Lett. **71**, 867 (1993).

[17] K. Tanaka, Y. Tsuchimura, K. Akabori, F. Ito, and T. Nagamura, Appl. Phys. Lett. **89**, 061916 (2006).

Summary

This thesis includes studies on dynamics of polymer thin films by inelastic neutron scattering. The contents of the respective chapters are summarized below.

In Chapter 1, the author gave a brief summary of glass transition phenomenon and reviewed the previous works on glass transition of polymer thin films to show a basis of the studies in this thesis.

In Chapter 2, the fundamental theories of neutron scattering were described, mainly focusing on inelastic and quasielastic scattering, and the principles and the performances of the spectrometers used in this thesis were explained.

In Chapter 3, effects of Al on T_g of polystyrene thin films have been studied using ellipsometry. It was found that the decrease of T_g with thickness was for Al deposited substrate, and thickness dependence of T_g was very similar with that obtained from X-ray reflectivity with Si substrate. It was supposed that weak interactions between polystyrene and Al might be concerned for this result.

In Chapter 4, the glassy dynamics of polymer thin films have been investigated with inelastic and quasielastic neutron scattering methods. We found that decrease of $< u^2 >$ with film thickness. In order to understand the decrease, we also analyzed the inelastic and quasielastic scattering data. As for the inelastic scattering, we studied the low energy excitations so-called Boson peak of thin films. No significant peak shift of boson peak has not been observed regardless of thickness, however the inelastic scattering intensity decreased with film thickness. As for the quasielastic scattering data, we focused on the local relaxation so-called fast process. The relaxation time of fast process has not been affected by thickness and only the scattering intensity decreased with thickness. Similar thickness dependence was observed for the Boson peak

and the fast process, suggesting a common physical origin of both dynamics. In order to interpret these experimental results, we assumed two possibilities: one is a spatial confinement effect and the other is an interfacial effect. Considering the obtained experimental results, the interfacial layer is supposed to be a candidate for the decrease of mobility with thickness.

We observed the decrease of mobility with thickness and assumed two possibilities in the former chapter. In Chapter 5, in order to draw a final conclusion, we studied the molecular weight dependence of $< u^2 >$ with the same film thickness, indicating the change of degree of spatial confinement. Any significant M_w dependence of $< u^2 >$ has not been observed within the error, implying that the interfacial layer is the dominant factor for the decrease of mobility. Such an interfacial layer is supposed to be formed by the orientation of polymer chain near the substrate.

In Chapter 6, the anisotropic and heterogeneous dynamics of polystyrene thin films have been studied, using a high Q accessible spectrometer. As for the anisotropy, we could not observe dynamical anisotropy for the 1000 Å thin film, but for the 200 Å thin films. The mobility in the perpendicular direction to the surface is higher than that in the parallel direction, and these results were also explained by the hard interfacial layer. We also evaluated the dynamical heterogeneity using the notion of non-Gaussian parameter A_0. We found that A_0 value increased with film with decreasing thickness, indicating the increase of heterogeneity with decreasing thickness. Assuming a simple bi-layer model that is constructed of bulk and interfacial layers, the experimental results were well described and we found that the interfacial hard layer was 130 Å thick.

In Chapter 7, we studied the glass transition of polystyrene thin films using a relatively high energy resolution spectrometer with an energy resolution of 0.025 meV, and T_g evaluated from the temperature dependence of mean square displacement $< u^2 >$ increased on the contrary to our expectation. The totally different thickness dependence of T_g was obtained from two different methods: ellipsometry and inelastic neutron scattering. We assumed that the broadening of the relaxation time in the α process, which is directly related to glass transition, might be concerned. The second possibility

is the different spatial scales probed by two methods and the third possibility is related to the low energy resolution of the OSIRIS measurements.

In Chapter 8, we studied the distribution of T_g in polystyrene thin films using a tri-layer stacked film of d-PS/h-PS/d-PS by neutron reflectivity. From the temperature dependence of the thickness of each layer, we evaluated T_g of each layer and found that surface T_g is about 15 K lower than that of bulk T_g and the T_g of the bottom layer is about 5 K higher than that of bulk and we could also confirm the heterogeneous distribution of T_g of polystyrene thin films from the temperature dependence of roughness of each layer.

List of publications

Journal

1) "Thermal expansion and contraction of polymer thin film", T. Kanaya, T. Miyazaki, R. Inoue, and K. Nishida, Physica Status Solidi (b) **242**, 595 (2005). (Chapter 4)

2) "Inelastic neutron scattering study of low energy excitations in polymer thin films", R. Inoue, T. Kanaya, K. Nishida, I. Tsukushi, and K. Shibata, Phys. Rev. Lett. **95**, 056102 (2005). (Chapter 4)

3) "Low-energy excitations and the fast process of polystyrene thin supported films studied by inelastic and quasielastic neutron scattering", R. Inoue, T. Kanaya, K. Nishida, I. Tsukushi, and K. Shibata, Phys. Rev. E **74**, 021801 (2006). (Chapter 4)

4) "Dynamic anisotropy and heterogeneity of polystyrene thin films as studied by inelastic neutron scattering", R. Inoue, T. Kanaya, K. Nishida, I. Tsukushi, J. Taylor, S. Levett, and B. J. Gabrys, Eur. Phys. J. E **24**, 55 (2007). (Chapter 6)

5) "Molecular weight dependence of mean square displacement in ultra-thin polymer films as studied by inelastic neutron scattering", R. Inoue, T. Kanaya, K. Nishida, I. Tsukushi, and K. Shibata, submitted to Phys. Rev. E. (Chapter 5)

Proceedings

1) "Glassy dynamics of polymer thin films", T. Kanaya, T. Miyazaki, R. Inoue, H. Yamano, K. Nishida, I. Tsukushi, and K. Shibata, AIP Conference Proceedings

708, 197, (2004). (Chapter 4)

2) "Glass transition and thermal expansivity of polystyrene thin films", R. Inoue, T. Kanaya, T. Miyazaki, K. Nishida, I. Tsukushi, and K. Shibata, Materials science and Engineering A **442**, 367, (2006). (Chapter 4)

3) "Dynamic structure studies on polymer thin films", R. Inoue, T. Miyazaki, I. Tsukushi, T. Kanaya, K. Nishida, and K. Shibata, AIP Conference Proceedings **832**, 46, (2006). (Chapter 4,6,7)

4) "Dynamic heterogeneity of polymer thin films in terms of non-Gaussian parameter", T. Kanaya, R. Inoue, K. Nishida, I. Tsukushi, J. Taylor, S. Levett, and B. J. Gabrys, Conference Proceedings QENS 2006, Materials Research Society, 161 (2007). (Chapter 6)

Other works

1) "Ultra-slow dynamics in glass-forming polybutadiene", R. Inoue, N. Takahashi, K. Nishida, and T. Kanaya, AIP Conference Proceedings **708**, 691 (2004).

2) "Thermal neutron spin-echo studies on dynamics of a glass-forming polymer in a high Q range", T. Kanaya, K. Kakurai, I. Tsukushi, R. Inoue, H. Watanabe, M. Nishi, K. Nakajima, K. Takemura, and H. Furuya, J. Phys. Soc. Jpn. **74**, 3236 (2005).

3) "A test of MIEZE-reflectometer for study of surface and interface", M. Hino, M. Kitaguchi, H. Hayashida, Y. kawabata, S. Tasaki, T. Ebisawa, D. Yamazaki, R. Maruyama, K. Tanaka, N. Torikai, R. Inoue, and T. Kanaya, Physica B **385-86**, 1125 (2006).

4) "Core Phase Transition of Radiation-Modified Polysilane Miscelles as Revealed from Their Thermochromism", H. Tanaka, N. Sato, T. Matsuyama, R. Inoue, and T. Kanaya, Polymer Journal, **39**, 874 (2007).

5) "X-ray reflectivity studies on glass transition of free standing polystyrene thin films", T. Miyazaki, R. Inoue, K. Nishida, and T. Kanaya, Eur. Phys. J. ST, **141**, 203 (2007).

Acknowledgments

The present thesis is based on the study carried out under the instruction of Professor Toshiji Kanaya, Laboratory of Polymer Materials Science, Division of Multidisciplinary Chemistry Polymer Materials Science, Institute for Chemical Research, Kyoto University, from 2002 to 2008.

The author would like to express his most sincere thanks to Professor Toshiji Kanaya for his continuous guidance, shrewd comments, discussion and collaborations through the course of the study.

Professor Takenao Yoshizaki and Professor Hiroshi Watanabe are especially acknowledged for their critical review of this thesis.

The author wishes to express his gratitude to Associate Professor Koji Nishida for his continuous encouragements, discussions and collaborations throughout this investigation.

The author is deeply indebted to Associate Professor Itaru Tsukushi, Chiba Institute of Technology, for his sincere experimental assistance for the neutron scattering measurements through this study.

The author is indebted to Dr. Go Matsuba for his helpful guidance and advice.

The author is sincerely grateful to Dr. Kaoru Shibata and Dr. Yukinobu Kawakita for their kind support in inelastic and quasielastic scattering measurements with LAM-40 at High Energy Accelerator Research Organization (KEK), Tsukuba. The author is grateful to Dr. Barbara J. Gabrys for her great arrangements for the measurements at ISIS facility, Rutherford Appleton Laboratory, UK. The author is grateful to Dr. Jon Taylor and Dr. Simon Levett for their kind support in inelastic and quasielastic scattering measurements with MARI at ISIS facility, Rutherford Appleton Labora-

tory, UK and also grateful to Dr. Mark Telling for their kind support in inelastic and quasielastic scattering measurements with OSIRIS at ISIS facility, Rutherford Appleton Laboratory, UK. The author is grateful to Associate Professor Masahiro Hino and Associate Professor Seiji Tasaki for the kind support in neutron reflectivity measurements with MINE-II at JRR-3M, Tokai. The author is also grateful to Professor Mitsuhiro Shibayama, Associate Professor Osamu Yamamuro, and Associate Professor Naoya Torikai for other neutron scattering measurements. The author is sincerely grateful to Associate Professor Yoshinobu Tsujii and Dr. Shinpei Yamamoto for their kind support in ellipsometry measurements.

The author especially wishes to express thanks to Dr. Tsukasa Miyazaki, Dr. Takahiko Kawai, Dr. Nobuaki Takahashi, Dr. Takashi Konishi, Dr. Hiroki Ogawa, Mr. Hiroaki Yamano, Mr. Tsuyoshi Tsubouchi, Mr. Toru Iseki, Mr. Yuki Echizenya, Ms. Yuri Wakasugi, Ms. Nami Nakai, and Ms. Hanako Ishida for their continuous support throughout this study at Kanaya laboratory and also wishes to express all the other past and current students of Kanaya laboratory.

Finally, the author expresses his gratitude to his family.

March 2008

Rintaro Inoue